PROBABILISTIC MODELS FOR WIND LOADS AND RELIABILITY ANALYSIS

A Dissertation

Presented to the Faculty of the Graduate School

of Cornell University

in Partial Fulfillment of the Requirements for the Degree of

Doctor of Philosophy

by

Haoran Zhao

December 2017

PROBABILISTIC MODELS FOR WIND LOADS AND RELIABILITY ANALYSIS

Haoran Zhao, Ph.D.

Cornell University 2017

Probabilistic models and surrogate solution are developed to characterize wind loads acting on the structures and assess the corresponding structural responses of linear systems, respectively. These developments can be regarded as essential building blocks in the prediction of structural reliability subject to extreme wind. In this dissertation, we first review the commonly-used probabilistic models in literature and benchmark these models on a test example to illustrate their properties and examine their advantages and disadvantages. It is shown that the approximations based on these existing models on the extreme estimates exhibit large discrepancies. A new probabilistic model is then proposed to overcome this limitation. The model utilized Markov process whose finite dimensional distribution is characterized in terms of copulas. Finally, an efficient and accurate surrogate model is presented as an alternative to the traditional Monte Carlo method to evaluate the structural responses. The responses are approximated by translation processes whose second-moment properties and marginal distribution are obtained from linear random vibration theory and moment equations. The statements in this dissertation are supported by theoretical arguments and numerical examples.

BIOGRAPHICAL SKETCH

Born in Xi'An, China, the author moved to Shanghai, China at his early age. He received the Bachelor of Engineering in Department of Civil Engineering at Tongji University. During his undergraduate study, he is also the caption of the student steel bridge competition in both ASCE Mid-Pacific and national student conferences held in Berkeley and Clemson, respectively. Then, he studied under the guidance of Professor Mircea Grigoriu in School of Civil and Environmental Engineering at Cornell University. His research includes development of probabilistic models for both wind loads and resulting structural responses and reliability analysis of linear and nonlinear systems under wind loads.

This dissertation is dedicated to my parents, Wei Zhao and Tong Zhu.

ACKNOWLEDGEMENTS

I am grateful for the support and assistance of many people who made the completion of this dissertation possible. First, I wish to thank my advisor Professor Mircea Grigoriu. He continually and convincingly conveyed a spirit of adventure and provided invaluable expertise and theoretical insights in regard to my research.

Second, I would like to thank my committee members, Professor Huseyin Topaloglu, Professor Max Zhang, and Professor Peter Diamessis for their assistance and suggestions throughout my Ph.D. career.

Further thanks go to Dr. Emil Simiu, Professor Luigi Carassale, Professor Yukio Tamura for the technical discussions regarding experimental datasets and numerical simulations and Dr. Alin Radu, Dr. Changhoon Lee, Wayne Uy for their help and encouragement.

Finally, I am grateful to my parents, who have been a constant source of inspiration and support throughout my studies and my life.

TABLE OF CONTENTS

LIST OF TABLES

LIST OF FIGURES

CHAPTER 1

INTRODUCTION

Performance-based engineering (PBE) is widely recognized as a rational approach to assess the risks of structures subject to natural hazards, both in the design of new structures and in the rehabilitation of existing ones [7, 15]. The objectives of PBE are to reduce casualty and minimize the structural damage and functional disruption to acceptable degrees in the catastrophic events. Reliability, i.e., the probability that a structure performs according to design specifications, is an essential ingredient of PBE that need to be determined. Reliability estimates account for the uncertainties in loading, structural characteristics, materials, load effects, and damages. In this dissertation, I focus on the PBE framework for wind hazards, referred to as performance-based wind engineering (PBWE), and provide essential tools for its practical implementation.

Accurate prediction of structural behavior under extreme wind loads is a prerequisite to estimate the reliability for PBWE. The assessment of structural performance involves two steps: (1) the characterization of input wind loads and (2) the evaluation of system responses to these input loads, as shown in Fig. 1.1. Note that structural systems are assumed to be deterministic.

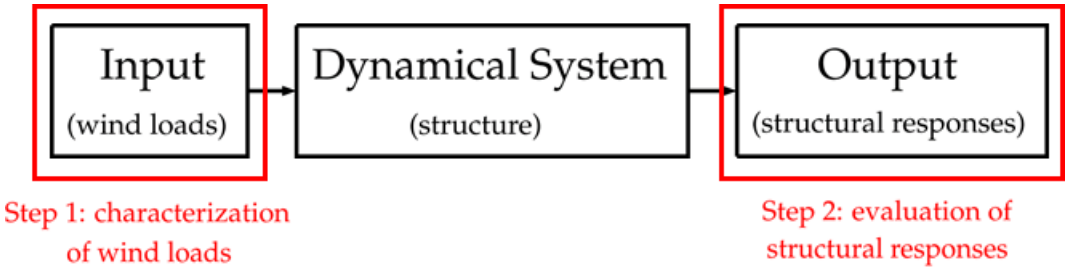

Figure 1.1: Analysis of structural behavior

Analytical methods, experimental tests, and computational fluid dynamics

(CFD) are employed to characterize wind loads in Step 1. Analytical methods, i.e., strip and quasi-static theories (see, e.g., [29]), provide a set of equations which relates the wind loads to the wind velocities from quasi-static analysis. With a suitable model on wind velocities, the spatial and temporal variations of wind loads can be readily predicted. Nevertheless, since these theories do not account for wind-structure interactions, the wind loads in the flow-separated regions cannot be correctly characterized [35]. On the other hand, experimental tests and CFD imitate in model scale the aerodynamic phenomena in the vicinity of structures in the full-scale environment. The time series of aerodynamic pressure acting on the structures are recorded through pressure taps. These time-series records provide essential information concerning wind loads since the effects of flow separation and vortex shedding have been taken into consideration. However, cost limits these approaches so that the obtained records are generally not sufficient to describe completely the probabilistic nature of wind loads. Consequently, probabilistic models need to be further calibrated to these pressure records in order to fully capture their uncertainties and extrapolate their statistical properties.

Many probabilistic models have been developed in the past a few decades. Gaussian models are the most commonly-used because of their mathematical simplicity. However, these models are not consistent with the essential statistical features of wind loads. For example, the skewness and kurtosis are -2.8959 and 21.6948 for the wind-pressure time series in Fig. 1.2(a) obtained from the experiment in Shimizu Corporation Laboratories (The skewness and kurtosis of Gaussian distribution are 0 and 3) [37]. The measurements are taken on the windward edge corner of a $0.1\text{m}\times0.1\text{m}\times0.5\text{m}$ rectangular building model. Fig. 1.2(b) shows the histogram of the wind-pressure time series in Fig. 1.2(a).

The red solid line indicates the Gaussian density with corresponding mean and variance with the time-series record.

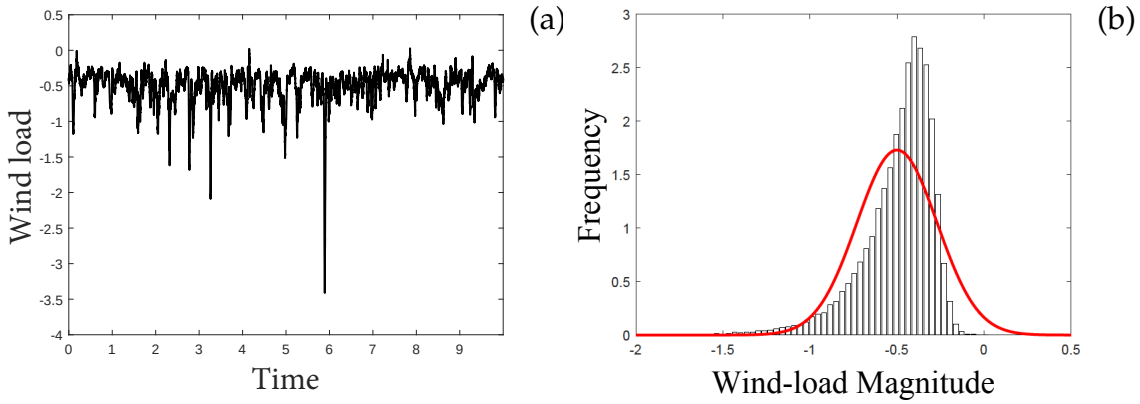

Figure 1.2: (a) time series of wind load and (b) its histogram

Attempts have been made to develop non-Gaussian models which are capable of matching the non-Gaussian features of the wind loads. The non-Gaussian models can be categorized into two classes: (1) extensions of Gaussian models, e.g., independent component analysis [30] and third-order spectral representation method (SRM) [51]; and (2) nonlinear transformation of Gaussian processes such as polynomial chaos [49] and translation model [17]. A detailed description regarding their properties and limitations is presented in Section 2 and 3. A common shortcoming of the aforementioned non-Gaussian models is that they cannot provide accurate approximations on the extremes of wind loads which are crucial for the reliability estimates in the PBWE framework.

The evaluation of the structural responses to the input wind loads is performed in Step 2. This is commonly carried out by Monte Carlo simulation. Large sets of sample wind loads are generated, structural responses are calculated for each wind-load sample, and statistical properties of responses such as reliability are estimated subsequently. The primary advantage of the Monte

Carlo method is that it provides guaranteed convergence for the estimation of any statistical property of the structural responses. Computational cost is the only limitation of this method, especially for complex systems.

This dissertation addresses both steps of performance evaluation. The models and methods presented in the subsequent sections provide means to accurately and efficiently predict the structural behavior. They can in turn be regarded as the essential building blocks of the PBWE framework. For Step 1, we aim to provide a comprehensive review on commonly-used non-Gaussian wind-load models and propose a novel non-Gaussian model to overcome the limitations of the existing models. The proposed model adopts the Markov assumption and its finite-dimensional distribution is characterized in terms of copulas. We show that this model performs consistently and remarkably on the extreme estimation of wind loads. Chapter 2 presents a new perspective on independent component analysis (ICA), one of the non-Gaussian models. Its applicability to non-Gaussian random vector and performance with respect to the vector dimension are examined. In Chapter 3, a review on the remaining aforementioned non-Gaussian models is provided following by the description of the proposed non-Gaussian model. Their statistical properties are listed and the accuracies are evaluated by a test case.

For Step 2, we present an alternative to the Monte Carlo simulation which is accurate and efficient. The structural responses are approximated by translation processes whose second-moment properties and marginal distribution are obtained from linear random vibration theory and moment equations, respectively. The approach is presented in Chapter 4.

Finally, Chapter 5 contains the conclusions drawn from this study. The state-

ments in these chapters are supported by theoretical arguments and numerical examples.

CHAPTER 2

A NEW PERSPECTIVE ON INDEPENDENT COMPONENT ANALYSIS

2.1 Summary

We examine the performance of the independent component analysis(ICA) which represents random vectors $\mathbf{X}$ by vectors $\tilde{\mathbf{X}}$ whose components are linear forms of independent random variables. The representation holds exactly or asymptotically in tails for Gaussian and non-Gaussian vectors with special characteristic functions or Gaussian, translation, and non-Gaussian vectors with independent tails. However, the distributions of $\tilde{\mathbf{X}}$ and its target vector $\mathbf{X}$ differ for a board range of non-Gaussian vectors. This statement is supported by numerical examples and theoretical arguments. It is also shown that the ICA representation $\tilde{\mathbf{X}}$ is approximately Gaussian for high dimensional vectors.

2.2 Introduction of ICA

Independent component analysis(ICA) is an useful tool in data processing and has been used successfully in several fields, e.g., market forecast [1] and wind engineering [5]. In ICA, a random vector is represented by a linear combination of deterministic vectors with the same dimension, referred to as modes, modulated by independent random variables. This representation has two benefits. First, it provides an efficient algorithm for generating samples of dependent random variables from samples of independent variables. Second, the modes have various meaningful interpretations in different applications. For example,

the ICA modes for the wind-induced pressure field on bluff bodies have the meaning of so-called coherent structures which reveal the flow behavior, detect the recurrent appearances of pressure patterns, and provide the information of vortex shedding in the neighborhood of the body [5].

Let $\mathbf{X} \in \mathbb{R}^m$ be an m-dimensional random vector with covariance matrix $\mathbf{\Sigma}$ and joint distribution $\mathbf{F}$. It is assumed without loss of generality that $\mathbf{X}$ has mean zero. The ICA represents $\mathbf{X}$ by $\tilde{\mathbf{X}}$ which has the form

$$\mathbf{X} \approx \tilde{\mathbf{X}} = \mathbf{AS} = \sum_{k=1}^{n} A_k S_k, \tag{2.1}$$

where $\mathbf{S} = [S_1, \ldots, S_k, \ldots, S_n]^T$ is an n-dimensional vector with independent components $\{S_k\}(n \leq m)$, and $\mathbf{A} = [A_1, \ldots, A_k, \ldots, A_n]$ is an $m \times n$ deterministic matrix, where the columns $A_k \in \mathbb{R}^m$, $k = 1, \ldots, n$, are modes [5].

We show that (1) it may not be possible to represent $\mathbf{X}$ by $\tilde{\mathbf{X}}$ exactly, i.e., $\mathbf{X} \stackrel{\mathrm{d}}{=} \tilde{\mathbf{X}}$ does not, generally, hold if $\{S_k\}$ are independent, and (2) the discrepancy between the target vector $\mathbf{X}$ and its ICA representation $\tilde{\mathbf{X}}$ can be significant. We only consider the case $n = m$. The construction of $\tilde{\mathbf{X}}$ for this case involves three steps. First, denote by L the Cholesky lower triangular matrix of known correlation matrix $\mathbf{\Sigma}$ of $\mathbf{X}$. Matrix L relates $\mathbf{\Sigma}$ through equation $\mathbf{\Sigma} = LL^T$, whose entries $\{L_{jk}\}$ can be calculated by [23, Sec. 5.2.1]

$$L_{jk} = \frac{\Sigma_{jk} - \sum_{r=1}^{k-1} L_{jr} L_{kr}}{\left[\Sigma_{kk} - \sum_{r=1}^{k-1} L_{kr}^2\right]^{1/2}}, \quad 1 \leq k \leq j \leq m, \text{ with } \sum_{r=1}^{0} L_{jr} L_{kr} = 0, \tag{2.2}$$

where $\{\Sigma_{jk}\}$ are the components of $\mathbf{\Sigma}$. Second, set $\mathbf{A} = L\Lambda$, where Λ is an arbitrary orthogonal matrix [9]. Note that $E[\tilde{\mathbf{X}}] = E[\mathbf{X}] = \mathbf{0}$ and

$$\begin{aligned} E[\tilde{\mathbf{X}}\tilde{\mathbf{X}}^T] = E\left[\mathbf{AS}\mathbf{S}^T\mathbf{A}^T\right] &= L\Lambda E\left[\mathbf{S}\mathbf{S}^T\right]\Lambda^T L^T \\ &= L\Lambda\Lambda^T L^T = LL^T = \mathbf{\Sigma} = E[\mathbf{X}\mathbf{X}^T], \ \forall\, \Lambda, \end{aligned} \tag{2.3}$$

provided $E[\mathbf{S}] = \mathbf{0}$ and $E\left[\mathbf{S}\mathbf{S}^T\right] = \mathbf{I}$, in which $\mathbf{0}$ is a zero vector and $\mathbf{I}$ is the identity matrix. Third, we use a metric to quantify the degree of dependence among the components of $\mathbf{S} = \Lambda^T L^{-1}\mathbf{X}$ to find an optimal Λ, e.g., the metric $d(\mathbf{S}) = |\sum_{k=1}^{m} H(S_k) - H(\mathbf{S})|$, where $H(S_k)$ and $H(\mathbf{S})$ are entropies defined by $H(S_k) = -\int f_{S_k} \log f_{S_k} ds_k$ and $H(\mathbf{S}) = -\int f_{\mathbf{S}} \log f_{\mathbf{S}} ds_1 \dots ds_m$, respectively, in which f_{S_k} and $f_{\mathbf{S}}$ are marginal and joint densities of $\mathbf{S}$ [8, 30]. Note that $d(\mathbf{S}) = 0$ iff $\mathbf{S}$ has independent components. Alternative metrics can be found in [43, 4, 57].

The remaining chapter has two parts. The first part presents cases in which the ICA representation $\tilde{\mathbf{X}}$ fully or partially characterizes $\mathbf{X}$. The second part provides several examples in which $\tilde{\mathbf{X}}$ and $\mathbf{X}$ differ and examines the accuracy of $\tilde{\mathbf{X}}$ for low and high dimensional vectors.

2.3 Exact ICA representation

We present two classes of random vectors that admit the representation in Eq. 2.1, Gaussian vectors and non-Gaussian vectors whose characteristic functions satisfy some conditions, and a class of non-Gaussian vectors for which Eq. 2.1 holds asymptotically in tails.

2.3.1 Gaussian vectors

If $\mathbf{X} \in \mathbb{R}^m$ is an m-dimensional Gaussian random vector with mean zero and correlation matrix Σ, then

$$\mathbf{X} \stackrel{\mathrm{d}}{=} \tilde{\mathbf{X}} = L\mathbf{S}, \tag{2.4}$$

where L is the Cholesky lower triangular matrix of $\mathbf{\Sigma}$ and $\{S_k\}$, the components of $\mathbf{S}$, are independent and identically standard Gaussian variables. The proof of the validity of Eq. 2.4 can be found in [48, Sec. 3.5.3].

2.3.2 Non-Gaussian vectors

The distributions of $\tilde{\mathbf{X}}$ and $\mathbf{X}$ are identical iff there exists an $\mathbf{A}$ such that the characteristic function of $\mathbf{X}$ satisfies the following condition

$$\varphi_X(\mathbf{W}^T\mathbf{v}) = E\left[\exp\{i\mathbf{v}^T\mathbf{W}\mathbf{X}\}\right] = \prod_{k=1}^{m} E\left[\exp\{iv_kS_k\}\right] = \prod_{k=1}^{m} E\left[\exp\{i\sum_{j=1}^{m} W_{kj}v_kX_j\}\right]$$
$$= \prod_{k=1}^{m} \varphi_X(W_{k1}v_k, \ldots, W_{kj}v_k, \ldots, W_{km}v_k), \tag{2.5}$$

where $\{S_k\}$, $\{X_j\}$, and $\{W_{kj}\}$ are components of $\mathbf{S}$, $\mathbf{X}$, and $\mathbf{W} = \mathbf{A}^{-1}$, respectively. This follows from the definition of $\tilde{\mathbf{X}}$ and the property of characteristic functions for independent random variables.

It is possible to satisfy the condition in Eq. 2.5. For example, Eq. 2.5 becomes

$$\varphi_X(W_{11}v_1 + W_{21}v_2, W_{12}v_1 + W_{22}v_2) = \varphi_X(W_{11}v_1, W_{12}v_1)\varphi_X(W_{21}v_2, W_{22}v_2) \tag{2.6}$$

for $m = 2$ and holds for a bivariate uniform vector $\mathbf{X} = [X_1, X_2]^T$ with probability density as shown in Fig. 2.1. The density and characteristic function of $\mathbf{X}$ in this figure are

$$f(x_1, x_2) = \begin{cases} \frac{1}{4}, & \text{for } x_1, x_2 \in A_{u1}. \\ 0, & \text{otherwise.} \end{cases} \tag{2.7}$$

$$\text{and } \varphi(v_1, v_2) = \frac{2\left[\cos(v_1) - \cos(2v_2)\right]}{4v_2^2 - v_1^2}, \tag{2.8}$$

respectively. Note that Eq. 2.6 holds when $W_{11} = 2W_{12}$ and $W_{21} = 2W_{22}$ so that there exists such a matrix $\mathbf{A}$ that $\tilde{\mathbf{X}} \overset{\text{d}}{=} \mathbf{X}$.

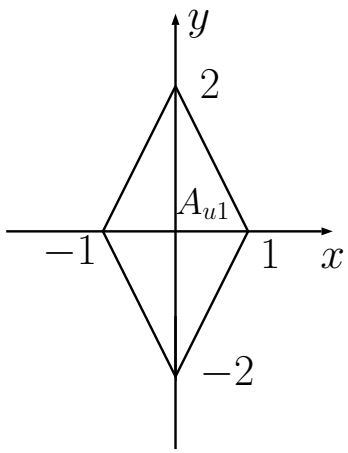

Figure 2.1: PDF of bivariate uniform distribution

2.3.3 Vectors with asymptotically independent components

Consider a special case of $\tilde{\mathbf{X}}$ by setting $\mathbf{A} = \mathbf{I}$. Then, Eq. 2.1 becomes

$$\tilde{\mathbf{X}} \stackrel{\mathrm{d}}{=} \mathbf{S}, \tag{2.9}$$

where **S** has independent components $\{S_j\}$ which satisfy the condition $S_j \stackrel{\mathrm{d}}{=} X_j$, and so does $\tilde{\mathbf{X}}$. Denote by $\tilde{X}_j,\ j = 1, \ldots, m$, the components of $\tilde{\mathbf{X}}$. We show that $\tilde{\mathbf{X}}$ and **X** have similar tails , i.e.,

$$\lim_{x_1,\ldots,x_m \to \infty} \left[P\big(\bigcap_{j=1}^{m} \{X_j \leq x_j\}\big) - \prod_{j=1}^{m} P\big(\tilde{X}_j \leq x_j\big) \right] = 0, \tag{2.10}$$

if **X** is Gaussian or translation with dependent components, and if **X** is a non-Gaussian, non-translation vector with independent tails.

Gaussian vectors

Suppose **X** is a standard Gaussian random vector. The proof of Eq. 2.10 follows from (1) the fact that X_j and $\tilde{X}_j$ have the same distributions, i.e., $X_j \stackrel{\mathrm{d}}{=} \tilde{X}_j,\ j = 1, \ldots, m$, (2) Corollary to the Normal Comparison Lemma which states that [40,

Corollary 2.1]

$$\left| P(\bigcap_{j=1}^{m}\{X_j \leq x_j\}) - \prod_{j=1}^{m} P(X_j \leq x_j) \right| \leq \frac{1}{4} \sum_{1 \leq r < t \leq m} |\rho_{rt}| \exp\left[-\frac{x_r^2 + x_t^2}{2(1+|\rho_{rt}|)} \right], \quad (2.11)$$

where ρ_{rt} is the covariance between X_r and X_t, and (3) the observation that the upper bound in Eq. 2.11 approaches zero as $x_1, \ldots, x_m \to \infty$.

Consider for illustration a bivariate Gaussian vector with mean zero and correlation matrix $\mathbf{\Sigma}$. The components of $\mathbf{\Sigma}$ are $\Sigma_{11} = \Sigma_{22} = 1$ and $\Sigma_{12} = \Sigma_{21} = 0.5$. Fig. 2.2 shows the probabilities $1 - P(X_1 \leq x, X_2 \leq x)$ and $1 - P(\tilde{X}_1 \leq x)P(\tilde{X}_2 \leq x)$. It can be seen that $P(X_1 \leq x, X_2 \leq x) \approx P(\tilde{X}_1 \leq x)P(\tilde{X}_2 \leq x)$ for sufficiently large x.

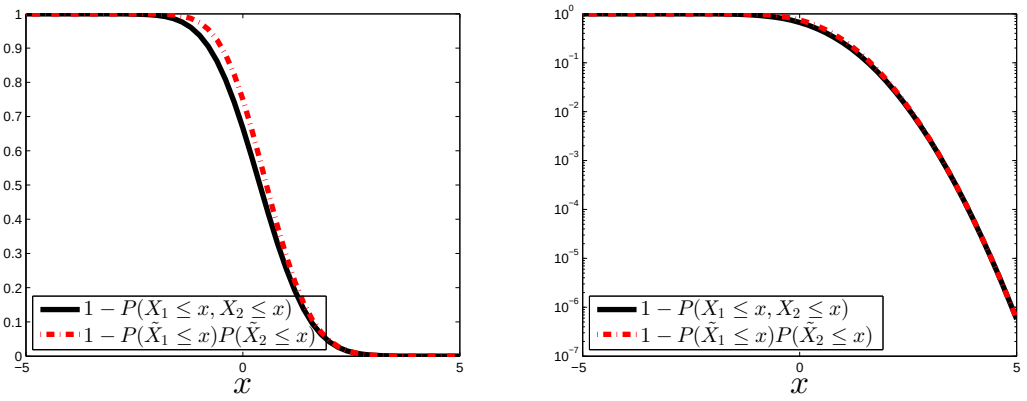

Figure 2.2: Plots of $1 - P(X_1 \leq x, X_2 \leq x)$ and $1 - P(\tilde{X}_1 \leq x)P(\tilde{X}_2 \leq x)$ for bivariate standard Gaussian vector with $\rho = 0.5$: linear (a) and logarithmic (b) scales

Translation vectors

Let $X_j = h_j(G_j)$, $j = 1, \ldots, m$, denote the components of a translation vector, where $\{G_j\}$ are correlated standard Gaussian variables and $h_j = F_j^{-1} \circ \Phi$ are generally nonlinear functions, in which F_j and Φ denote the distribution of X_j and standard Gaussian distribution, respectively [17, Sec. 3.1]. Note that Eq. 2.10

can be written as

$$\lim_{u_1,\ldots,u_m\to 1}\left[P\big(\bigcap_{j=1}^{m}\{X_j \le F_j^{-1}(u_j)\}\big) - \prod_{j=1}^{m} u_j\right] = 0, \tag{2.12}$$

since $P(\tilde{X}_j \le F_j^{-1}(u_j)) = u_j$, $j = 1, \ldots, m$.

The limit in Eq. 2.12 holds by the definition of translation vectors and the property of Gaussian vectors. We have

$$\begin{aligned}\lim_{u_1,\ldots,u_m\to 1} P\big(\bigcap_{j=1}^{m}\{X_j \le F_j^{-1}(u_j)\}\big) &= \lim_{u_1,\ldots,u_m\to 1} P\big(\bigcap_{j=1}^{m}\{F_j^{-1}(\Phi(G_j)) \le F_j^{-1}(u_j)\}\big)\\ &= \lim_{u_1,\ldots,u_m\to 1} P\big(\bigcap_{j=1}^{m}\{G_j \le \Phi^{-1}(u_j)\}\big)\\ &= \lim_{u_1,\ldots,u_m\to 1}\prod_{j=1}^{m} u_j. \end{aligned}\tag{2.13}$$

The above property can be illustrated by Fig. 2.3 which shows $1 - P(X_1 \le x, X_2 \le x)$ and $1 - P(\tilde{X}_1 \le x)P(\tilde{X}_2 \le x)$ for a bivariate translation vector with standard exponential marginal distributions $F_1(x) = F_2(x) = 1 - \exp(-x)$. The probabilities $P(X_1 \le x, X_2 \le x)$ and $P(\tilde{X}_1 \le x)P(\tilde{X}_2 \le x)$ match in the tail region.

Non-Gaussian, non-translation vectors with independent tails

Consider a bivariate random vector **X** with components X_1 and X_2 with distributions F_1 and F_2, respectively. Define by $\lambda_u = P(X_2 > F_2^{-1}(u) | X_1 > F_1^{-1}(u))$ the upper tail dependence coefficient. If

$$\lim_{u\to 1}\lambda_u = 0, \tag{2.14}$$

then we say that **X** is upper tail independent [33, Sec. 2.1.10]. We show that this definition implies that $P(X_1 \le F_1^{-1}(u), X_2 \le F_2^{-1}(u))$ approaches $P(X_1 \le$

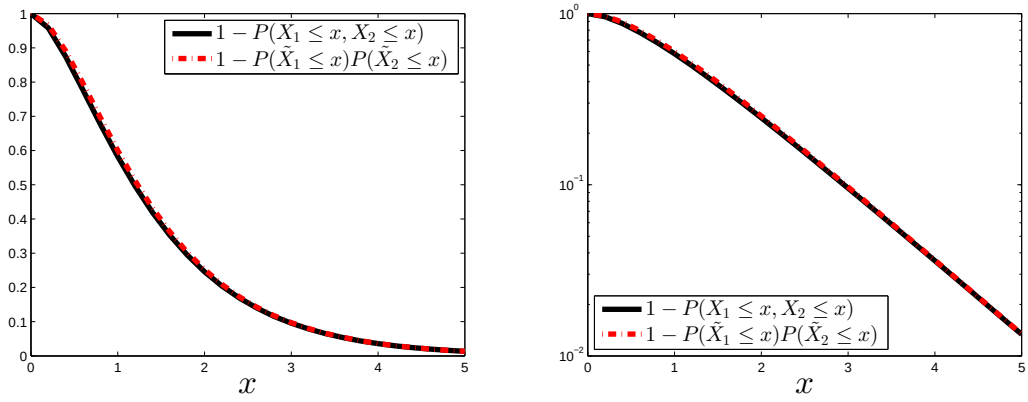

Figure 2.3: Plots of $1 - P(X_1 \le x, X_2 \le x)$ and $1 - P(\tilde{X}_1 \le x)P(\tilde{X}_2 \le x)$ for bivariate translation vector with $F_1(x) = F_2(x) = 1 - \exp(-x)$: linear (a) and logarithmic (b) scales

$F_1^{-1}(u))P(X_2 \le F_2^{-1}(u))$ for u arbitrarily close to 1, in other words, Eq. 2.14 is a sufficient condition for

$$\lim_{u \to 1} \left[P(X_1 \le F_1^{-1}(u), X_2 \le F_2^{-1}(u)) - u^2 \right] = 0. \tag{2.15}$$

If Eq. 2.14 holds, then

$$\begin{aligned}
0 &= \lim_{u \to 1} \frac{P(X_1 > F_1^{-1}(u), X_2 > F_2^{-1}(u))}{P(X_1 > F_1^{-1}(u))} \\
&= \lim_{u \to 1} \frac{1 - P(X_1 \le F_1^{-1}(u)) - P(X_2 \le F_2^{-1}(u)) + P(X_1 \le F_1^{-1}(u), X_2 \le F_2^{-1}(u))}{1 - P(X_1 \le F_1^{-1}(u))} \\
&= \lim_{u \to 1} \frac{1 - 2u + P(X_1 \le F_1^{-1}(u), X_2 \le F_2^{-1}(u))}{1 - u} \\
&= 2 - \lim_{u \to 1} \frac{P(X_1 \le F_1^{-1}(u), X_2 \le F_2^{-1}(u)) - 1}{u - 1} \times \\
&\lim_{u \to 1} \frac{\log u}{\log P(X_1 \le F_1^{-1}(u), X_2 \le F_2^{-1}(u))} \frac{\log P(X_1 \le F_1^{-1}(u), X_2 \le F_2^{-1}(u))}{\log u} \\
&= 2 - \lim_{u \to 1} \frac{\log P(X_1 \le F_1^{-1}(u), X_2 \le F_2^{-1}(u))}{\log u}
\end{aligned} \tag{2.16}$$

Let $f(u)$ denote $\log u / \log P(X_1 \le F_1^{-1}(u), X_2 \le F_2^{-1}(u))$. Note that Eq. 2.16 holds since

$$\lim_{u \to 1} f(u) = \lim_{u \to 1} \frac{P(X_1 \le F_1^{-1}(u), X_2 \le F_2^{-1}(u))}{u \frac{d}{du} P(X_1 \le F_1^{-1}(u), X_2 \le F_2^{-1}(u))} = \frac{1}{2} < \infty. \tag{2.17}$$

Then, by multiplying $\lim_{u\to 1}\log u$ on both sides of Eq. 2.16, we have

$$\begin{aligned} 0 &= \lim_{u\to 1}\frac{\log P(X_1 \le F_1^{-1}(u), X_2 \le F_2^{-1}(u))}{\log u}\lim_{u\to 1}\log u - 2\lim_{u\to 1}\log u \\ &= \lim_{u\to 1}\left[P(X_1 \le F_1^{-1}(u), X_2 \le F_2^{-1}(u)) - u^2\right]. \end{aligned} \tag{2.18}$$

On the other hand, Eq. 2.15 does not imply Eq. 2.14. One counterexample is a bivariate vector with distribution

$$\begin{aligned} F(x_1, x_2) &= \exp\left\{-\left[x_1^{-\frac{1}{\theta}} + x_2^{-\frac{1}{\theta}}\right]^{\theta}\right\} \\ x_1, x_2 &\ge 0, \quad \theta \in (0, 1]. \end{aligned} \tag{2.19}$$

This distribution satisfies Eq. 2.15 but $\lambda_u = 2 - 2^{\theta} \neq 0$ if $\theta \neq 1$.

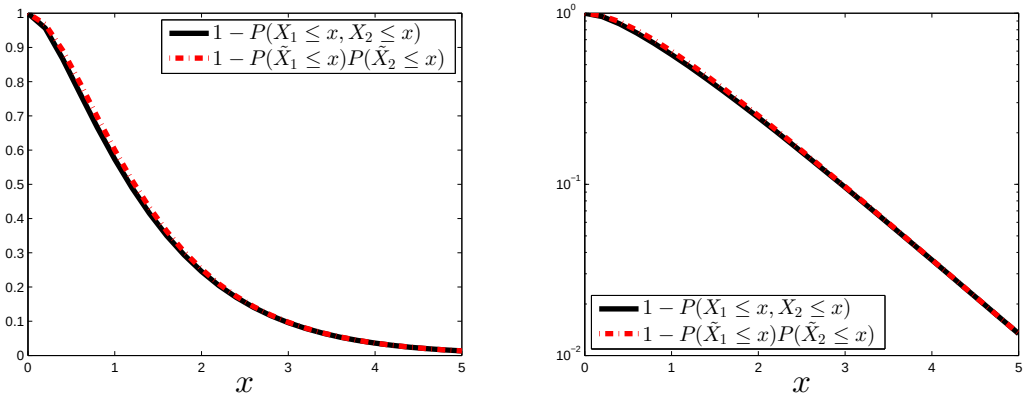

Figure 2.4: Plots of $1 - P(X_1 \le x, X_2 \le x)$ and $1 - P(\tilde{X}_1 \le x)P(\tilde{X}_2 \le x)$ for bivariate Gumbel distribution with $\alpha = 0.5$: linear (a) and logarithmic (b) scales

An example for upper tail independent random vector is a bivariate Gumbel vector with joint and marginal distributions of X_1 and X_2 defined by [38, Sec. 2.2]

$$\begin{aligned} F(x_1, x_2) &= (1 - \exp(-x_1))(1 - \exp(-x_2))(1 + \alpha\exp(-x_1 - x_2)) \\ x_1, x_2 &\ge 0, \quad \alpha \in [-1, 1], \end{aligned} \tag{2.20}$$

and

$$F_j(x_j) = 1 - \exp(-x_j), \quad j = 1, 2, \tag{2.21}$$

respectively. Note that this is not a translation vector since $f(x_1, x_2) \prod_{j=1}^{2} \phi(g_j)/f(x_j)$ does not admit the form of Gaussian joint density with arguments $g_j, j = 1, 2$, where $g_j = \Phi^{-1}(F_j(x_j))$, ϕ is standard Gaussian density, and $f(x_1, x_2)$ and $f(x_j), j = 1, 2$, denote the joint and marginal densities of X_1 and X_2, respectively. Fig. 2.4 shows the probabilities $1 - P(X_1 \leq x, X_2 \leq x)$ and $1 - P(\tilde{X}_1 \leq x)P(\tilde{X}_2 \leq x)$ with $\alpha = 0.5$. It can be seen that $P(X_1 \leq x, X_2 \leq x) \approx P(\tilde{X}_1 \leq x)P(\tilde{X}_2 \leq x)$ in the tail region which supports Eq. 2.15.

2.4 Approximate ICA representation

We give examples of low dimensional non-Gaussian vectors for which the ICA representation does not hold, and examine the accuracy of $\tilde{\mathbf{X}}$ for this case. We also show that the ICA representation $\tilde{\mathbf{X}}$ for arbitrary high dimensional non-Gaussian vectors is approximately Gaussian.

2.4.1 Low dimensional vectors

There are numerous non-Gaussian vectors that do not admit the ICA representation. We give one example to support this statement. The components X_1 and X_2 of $\mathbf{X}$ have joint density $f(x_1, x_2) = (2\pi)^{-1}(1 + x_1^2 + x_2^2)^{-\frac{3}{2}}$, which is known as the circular bivariate Cauchy distribution. The characteristic function of $\mathbf{X}$ is $\varphi_X(v_1, v_2) = \exp\{-(v_1^2 + v_2^2)^{\frac{1}{2}}\}$ [12]. The equality of Eq. 2.6 holds iff $W_{11}W_{22} + W_{12}W_{21} = 0$ which indicates the singularity of matrix $\mathbf{W} = \mathbf{A}^{-1}$.

Therefore, matrix **A** does not exist in this example.

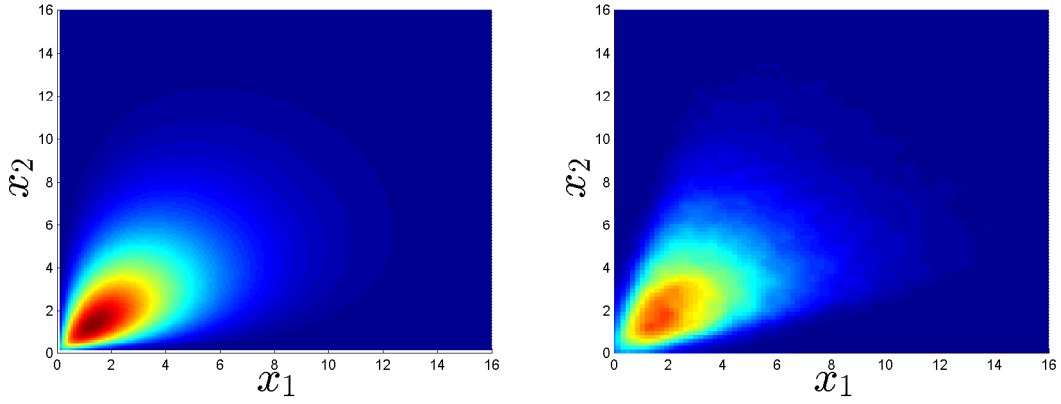

Figure 2.5: Joint densities of target vector **X** (a) and the ICA representation $\tilde{\mathbf{X}}$ (b)

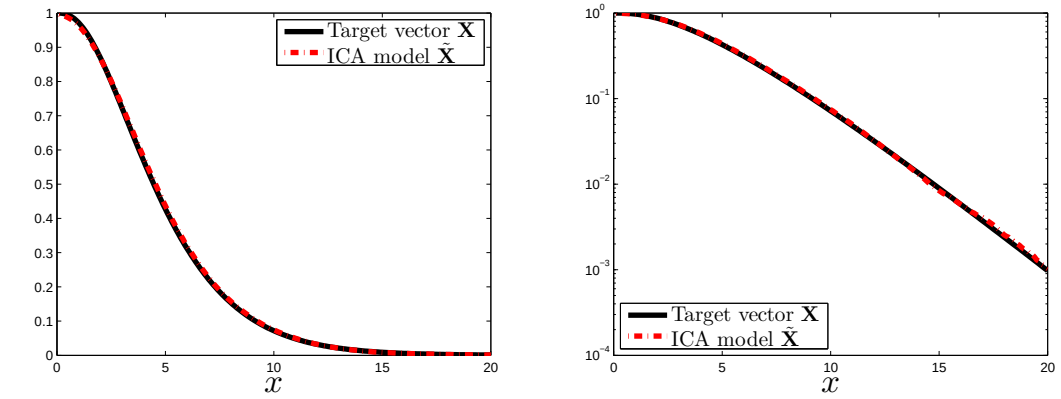

Figure 2.6: Plots of $1 - P(X_1 \leq x, X_2 \leq x)$ and $1 - P(\tilde{X}_1 \leq x, \tilde{X}_2 \leq x)$ of **X** and $\tilde{\mathbf{X}}$ for bivariate translation vectors with Gamma marginals: linear (a) and logarithmic (b) scales

Moreover, two examples are provided to reveal the performance of $\tilde{\mathbf{X}}$ for low dimensional vectors. The ICA representation $\tilde{\mathbf{X}}$ may be a satisfactory approximation of **X**. The example for illustration is a bivariate translation vector with components $X_j = F_j^{-1}(\Phi(G_j))$, $j = 1, 2$, where $\{G_1, G_2\}$ are correlated standard Gaussian variables with correlation coefficient $\rho = 0.5$, and $F_1 = F_2$ are Gamma distribution with shape coefficient $k = 2$ and scale coefficient $\theta = 2$. The joint density of $\tilde{\mathbf{X}}$ almost coincides with that of target vector **X**, as shown in Fig. 2.5. Fig. 2.6 shows the probabilities $1-P(X_1 \leq x, X_2 \leq x)$ and $1-P(\tilde{X}_1 \leq x, \tilde{X}_2 \leq x)$.

The differences of two lines are almost indistinguishable at the figure scale. Suppose now $\mathbf{X} = [X_1, X_2]^T$ is a bivariate zero-mean T-distributed random vector with density

$$f(x_1, x_2) = \frac{\Gamma[\nu/2+1]}{\Gamma(\nu/2)\nu\pi\sqrt{|\mathbf{\Sigma}|}\left[1+\mathbf{x}^T\mathbf{\Sigma}^{-1}\mathbf{x}/\nu\right]^{\nu/2+1}} = \frac{1}{2\pi\sqrt{|\mathbf{\Sigma}|}\left[1+\mathbf{x}^T\mathbf{\Sigma}^{-1}\mathbf{x}/\nu\right]^{\nu/2+1}}, \tag{2.22}$$

where $\mathbf{x} = [x_1, x_2]^T$, $\nu > 2$ is the degree of freedom, Γ denotes Gamma function, and $\mathbf{\Sigma}$ is the correlation matrix. Consider the special case where the components of correlation matrix $\Sigma_{ij} = \delta_{ij}$, in which δ_{ij} indicates the Kronecker delta function. Then, equation $\mathbf{S} = \Lambda^T L^{-1}\mathbf{X}$ takes the form

$$\begin{aligned} S_1 &= \frac{1}{a}\cos\psi X_1 + \frac{1}{a}\sin\psi X_2, \\ S_2 &= -\frac{1}{a}\sin\psi X_1 + \frac{1}{a}\cos\psi X_2, \end{aligned} \tag{2.23}$$

where $a = \sqrt{\nu/(\nu-2)}$ and Λ has columns $[\cos\psi, \sin\psi]^T$ and $[-\sin\psi, \cos\psi]^T$. The joint density of $\mathbf{S}$, denoted by $f_{\mathbf{S}}(s_1, s_2)$, has the expression

$$\begin{aligned} f_{\mathbf{S}}(s_1, s_2) &= f(a\cos\psi s_1 - a\sin\psi s_2, a\sin\psi s_1 + a\cos\psi s_2) \\ &= \frac{1}{2\pi}\left[1 + a^2(s_1^2+s_2^2)/\nu\right]^{-(\nu/2+1)}. \end{aligned} \tag{2.24}$$

We can see that $f_{\mathbf{S}}(s_1, s_2)$ is irrespective of the direction ψ which implies that there is no theoretical optimal Λ. However, optimal Λ results if the information of $\mathbf{X}$ consists of a finite number of samples. Figs. 2.7 and 2.8 show the joint densities of $\mathbf{X}$ and $\tilde{\mathbf{X}}$ and the probabilities $1 - P(X_1 \le x, X_2 \le x)$ and $1 - P(\tilde{X}_1 \le x, \tilde{X}_2 \le x)$ for $\nu = 5$ from 100000 samples. The differences in the tail region are large.

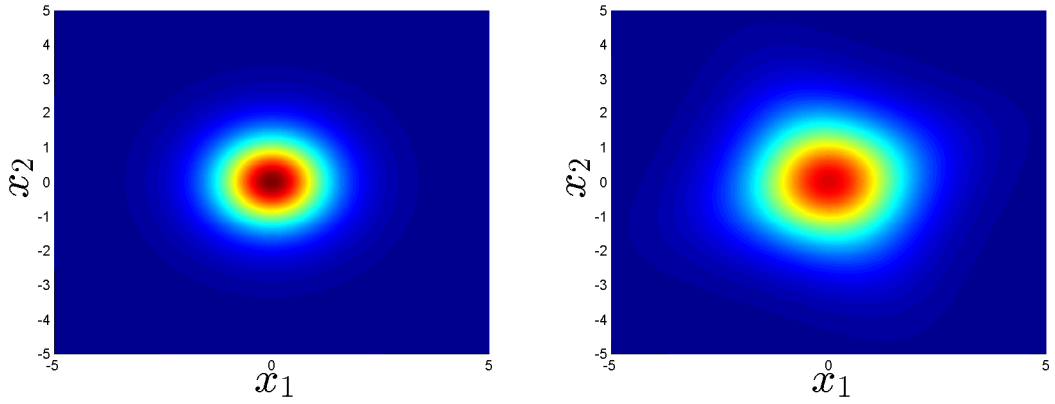

Figure 2.7: Joint densities of target vector $\mathbf{X}$ (a) and the ICA representation $\tilde{\mathbf{X}}$ (b)

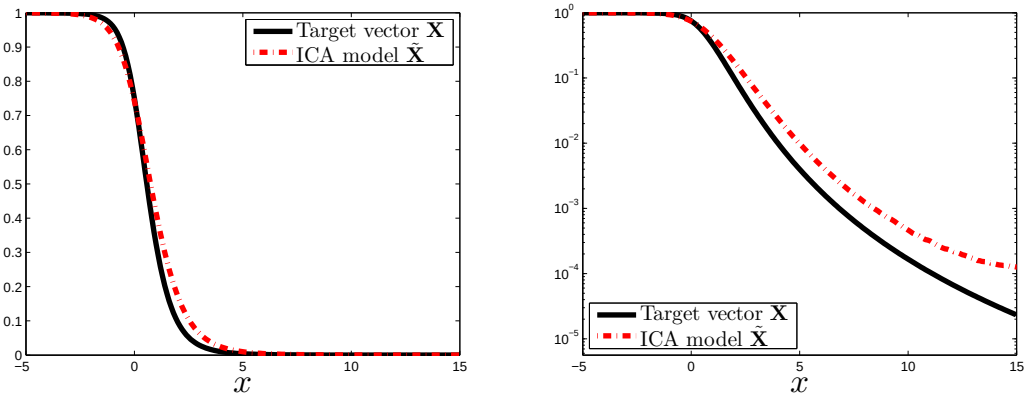

Figure 2.8: Plots of $1 - P(X_1 \leq x, X_2 \leq x)$ and $1 - P(\tilde{X}_1 \leq x, \tilde{X}_2 \leq x)$ of $\mathbf{X}$ and $\tilde{\mathbf{X}}$ for bivariate T-distributed vectors: linear (a) and logarithmic (b) scales

2.4.2 High dimensional vectors

The ICA representation $\tilde{\mathbf{X}}$ performs poorly for high dimensional vectors. We prove this statement by using the Lindeberg-Feller Central Limit Theorem that is stated here for convenience.

Suppose $\{S_k, k = 1, \ldots, n\}$ is a set of independent random variables with mean zero, variances $\sigma_k^2 = E[S_k^2]$, and distributions F_k^S. Set $w_n^2 = \sum_{k=1}^{n} \sigma_k^2$ and $W_n = S_1 + \cdots + S_n$. We say that $\{S_k\}$ satisfies the Lindeberg-Feller condition if

we have

$$\frac{1}{w_n^2}\sum_{k=1}^{n} E\left[S_k^2\, 1_{(|S_k/w_n|>\xi)}\right] = \frac{1}{w_n^2}\sum_{k=1}^{n}\int_{|s_k|>\xi\, w_n} s_k^2\, F_k^S(ds_k) \to 0, \text{ as } n\to\infty,\ \forall \xi > 0. \tag{2.25}$$

This condition means that most of the probability mass of S_k is in an interval about the mean and this interval is small relative to w_n. The Lindeberg-Feller Central Limit Theorem states that the Lindeberg-Feller condition implies W_n/w_n converges in distribution to $N(0,1)$ as $n\to\infty$, where $N(0,1)$ denotes the standard Gaussian random variable [47, Sec. 9.8].

Recall the ICA representation in Eq. 2.1, i.e., $\tilde{\mathbf{X}} = \mathbf{AS}$, where $\mathbf{S}$ is a n-dimensional random vector with independent components $\{S_k\}$ of mean zero and finite variances, $\tilde{\mathbf{X}}$ is a $\mathbb{R}^m$-valued random vector, and $\mathbf{A}$ is the $m\times n$ transformation matrix with components $\{A_{jk}\}$. Note that we do not restrict $\tilde{\mathbf{X}}$ and $\mathbf{S}$ to have the same dimension, i.e., $m=n$, in this proof. Set

$$W_n = \sum_{j=1}^{m}\beta_j\tilde{X}_j = \sum_{j=1}^{m}\sum_{k=1}^{n} A_{jk}\beta_j S_k = \sum_{k=1}^{n}\left[\sum_{j=1}^{m} A_{jk}\beta_j\right] S_k = \sum_{k=1}^{n} Y_k, \tag{2.26}$$

where $Y_k = \left[\sum_{j=1}^{m} A_{jk}\beta_j\right] S_k$ and $\{\beta_j\}$ are arbitrary constants. The random variables $\{Y_k\}$ have finite variances provided $E[S_k^2]<\infty$. Since $\{S_k\}$ are independent and the distributions are assumed to satisfy the Lindeberg-Feller condition, so are $\{Y_k\}$. Accordingly, $W_n/w_n \to N(0,1)$ in distribution as $n\to\infty$ with the notation $w_n = \sum_{k=1}^{n} E[Y_k^2]$, and since $\{\beta_j\}$ are arbitrary, $\tilde{\mathbf{X}}$ becomes a Gaussian vector as n increases indefinitely. Denote the characteristic functions of W_n and $\tilde{\mathbf{X}}$ by $\varphi_W(t)$ and $\varphi_{\tilde{X}}(\mathbf{v})$, respectively. The above statement can be proved based on (1) the equivalence of $\varphi_W(t)$ and $\varphi_{\tilde{X}}(\mathbf{v})$, i.e.,

$$\varphi_W(t) = E\left[\exp\left(iW_n t\right)\right] = E\left[\exp\left\{i(\sum_{j=1}^{m}\beta_j\tilde{X}_j)t\right\}\right] = E\left[\exp\left\{i(\sum_{j=1}^{m} v_j\tilde{X}_j)\right\}\right] = \varphi_{\tilde{X}}(\mathbf{v}), \tag{2.27}$$

with the notation $v_j = \beta_j t$, and (2) the fact that $\varphi_W(t)$ converges to Gaussian characteristic function as $n \to \infty$. Hence, $\tilde{\mathbf{X}}$ is approximately Gaussian for sufficiently large n.

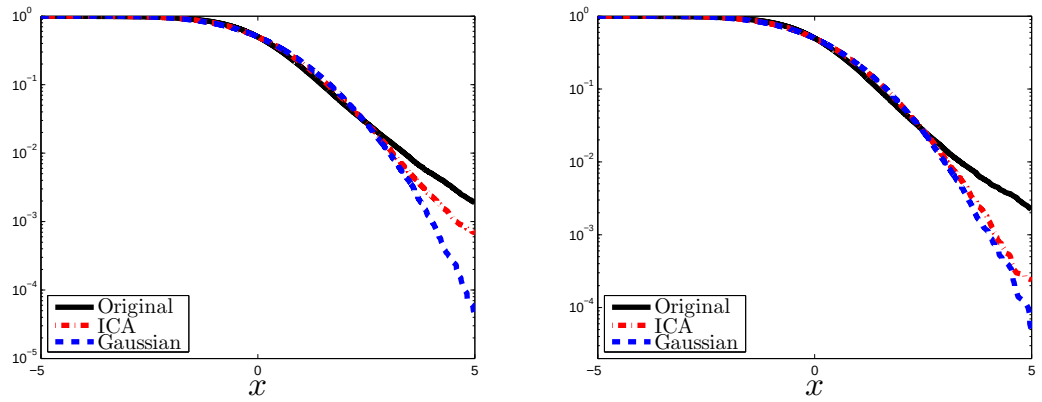

Figure 2.9: Marginal distributions of $\mathbf{X}$, $\tilde{\mathbf{X}}$, and multivariate Gaussian distribution with dimensions: $n = 20$ (a) and $n = 40$ (b)

The above theoretical arguments can be illustrated by a numerical example. Consider a T-distributed random vector with five degrees-of-freedom. Fig. 2.9 shows the marginal distributions of $\mathbf{X}$, $\tilde{\mathbf{X}}$, and multivariate Gaussian distribution with dimensions $n = 20$ and $n = 40$. It can be seen that the distribution of $\tilde{\mathbf{X}}$ tends to be Gaussian for large n.

Generally, the dimension of $\mathbf{X}$ is larger than that of $\mathbf{S}$, i.e., $n < m$. Yet, if the ratio of these dimensions is kept constant, we note that $n \to \infty$ as $m \to \infty$ so that the previous statement applies.

2.5 Chapter summary

We have provided a critical evaluation of the performance of the independent component analysis (ICA). In ICA, random vectors $\mathbf{X}$ are characterized by vec-

tors $\tilde{\mathbf{X}}$ which are defined by the summations of deterministic vectors with the same dimension, multiplied by independent random variables. We have shown that (1) $\tilde{\mathbf{X}}$ and $\mathbf{X}$ have the same distribution if $\mathbf{X}$ follows Gaussian and non-Gaussian probability laws of which the characteristic functions satisfy some conditions; and (2) $\tilde{\mathbf{X}}$ can represent $\mathbf{X}$ in tails if $\mathbf{X}$ is non-Gaussian with independent tails.

However, the representation $\tilde{\mathbf{X}}$ does not, generally, hold for non-Gaussian $\mathbf{X}$. The validity of this statement and the accuracy of $\tilde{\mathbf{X}}$ have been illustrated by several numerical examples for low dimensional non-Gaussian vectors. Moreover, Lindeberg-Feller Central Limit Theorem shows that $\tilde{\mathbf{X}}$ is approximately Gaussian for high dimensional non-Gaussian vectors. It was concluded that ICA is an useful tool which provides exact representation or satisfactory approximation for some cases, but it needs to be used with great caution for the others.

CHAPTER 3

REVIEW OF NON-GAUSSIAN MODELS AND COPULA-BASED MARKOV MODEL

3.1 Summary

A probabilistic model is developed for stochastic processes that have been widely applied in engineering mechanics. We review the other three commonly-used models introduced in introduction and benchmark these models on a test example to illustrate their properties and examine their advantages and disadvantages. It is shown that the approximations based on these existing models on the metric of distribution of extreme exhibit large discrepancies. We propose a new probabilistic model to overcome this limitation. The model utilizes m^{th}-order Markov process whose finite dimensional distribution is characterized in terms of copulas. The parameters of the copulas are selected such that the errors on the linear combinations of quantities of interest are minimized. Theoretical arguments and numerical examples are provided to demonstrate the properties of the model. The model is then applied to the wind pressure process obtained from the wind tunnel experiment to illustrate its practical use.

3.2 Introduction of models for stochastic processes

Stochastic processes $Q(t)$ abound in engineering mechanics. For example, they can represent wind loads on the buildings, wave forces on the offshore platforms, and seismic ground accelerations on the structural foundations. Statis-

tical analysis of the system responses subjected to these actions is commonly carried out in the context of Monte Carlo simulation where a large number of sample processes are generated, the system governing equations are solved for each sample process, and the outputs are evaluated statistically. However, the number of available records of these stochastic processes $Q(t)$ is generally insufficient to perform such analysis. Models $\tilde{Q}(t)$, which approximate the probability law of $Q(t)$ to an acceptable degree, need to be used to characterize these stochastic processes beyond their records.

Many probabilistic models have been developed in the past few decades. The most commonly-used models are the Karhunen-Loéve and spectral representations. Suppose that the stochastic process $Q(t)$ has mean zero and finite correlation function $r(\tau) = E[Q(t+\tau)Q(t)]$, Karhunen-Loéve representation $\tilde{Q}_m^{KL}(t)$ approximates $Q(t)$ by [24](p. 161)

$$Q(t) \approx \tilde{Q}_m^{KL}(t) = \sum_{k=1}^{m} \phi_k(t) Z_k, \;\; t \in D, \tag{3.1}$$

where m is the truncation level, D is a bounded time interval, $\{Z_k\}$ are uncorrelated random variables with means zero and variances $\{\lambda_k\}$, and $\{\lambda_k, \phi_k(t)\}$ are eigenvalues and eigenfunctions of $r(\tau)$. Under the further assumption that $Q(t)$ is stationary, the spectral representation $\tilde{Q}_m^{SR}(t)$ has the expression

$$Q(t) \approx \tilde{Q}_m^{SR}(t) = \sum_{k=1}^{m} [\cos(\omega_k t)\Delta u_k + \sin(\omega_k t)\Delta v_k], \;\; t \in D, \tag{3.2}$$

where $\{\omega_k, \Delta\omega_k\}$ are partitions of non-negative frequencies ω, $S(\omega)$ is the two-sided spectral density of $Q(t)$, and the orthogonal increments $\Delta u_k := X_k$ and $\Delta v_k := Y_k$ can be considered as independent Gaussian random variables with means zero and variances $2S(\omega_k)\Delta\omega_k$. An alternative form of spectral representation defines the orthogonal increments $\Delta u_k := 2\sqrt{S(\omega_k)\Delta\omega_k}\cos(\psi_k)$ and

$\Delta v_k := 2\sqrt{S(\omega_k)\Delta\omega_k}\sin(\psi_k)$, where $\{\psi_k\}$ are independent uniform random variables in the range $[0, 2\pi]$. The properties and differences of these two forms of spectral representations are presented in [20].

The aforementioned models have the second-order nature, that is, they are constructed to represent the stochastic process $Q(t)$ up to the second moments, unless $Q(t)$ is Gaussian-distributed. However, the Gaussian assumption is not realistic in practical applications. For example, wind velocities and wind pressures in the flow separated region have been shown to follow distributions which are clearly non-Gaussian [36]. Attempts have been made to develop non-Gaussian models so that information on $Q(t)$ can be captured beyond the second moments. A direct extension of Karhunen-Loéve representation is provided in [46], wherein the basis functions $\{\phi_k(t)\}$ in Eq. 3.1 remain the eigenfunctions of correlation function $r(\tau)$ and the samples of Z_k, $k = 1, \ldots, m$, are iteratively updated so that the marginal distribution of the model $\tilde{Q}_m^{KL}(t)$ converges to that of $Q(t)$. However, such convergence is not guaranteed and the marginal distribution of $\tilde{Q}_m^{KL}(t)$ generally does not match the marginal distribution of $Q(t)$ exactly. The spectral representation method is generalized in [51], referred to as the third-order spectral representation method (SRM). The orthogonal increments Δu_k and Δv_k are required to satisfy the additional third-order orthogonality conditions. As a consequence, the resulting representation matches the prescribed third-order cumulant function. Nonetheless, this representation is not able to capture the marginal distribution of $Q(t)$ and cannot distinguish between processes that are equal in the third moment sense, as illustrated in the numerical example.

Aside from these direct extensions, nonlinear transformations of standard

Gaussian process are another class of non-Gaussian models. Two types of models are considered here. The first model utilizes the polynomial chaos representation which represents the process $Q(t)$ in terms of the Hermite polynomials of standard Gaussian process with deterministic coefficients [49]. The representation is truncated such that the resulting approximation is accurate to an acceptable degree and can be constructed within the computational budget. It can be shown that polynomial chaos approximation converges to $Q(t)$ in the mean square sense and in finite dimensional distribution. However, limitations of such approximation are explored in [14, 13]. For example, higher-order moments of the approximation may diverge as the truncation level increases. The second type is the translation model which constitutes the mapping between the target process $Q(t)$ and standard Gaussian process by using the marginal distribution of $Q(t)$ [18]. The translation model is capable of matching the marginal distribution and the correlation function of $Q(t)$ if they are consistent with each other. Recent developments of algorithms have enabled the efficient use of this model for simulation.

In this work, a comprehensive review of the aforementioned non-Gaussian models is provided. The detailed properties of these models are listed and their accuracies are examined by numerical example. The metric of the distribution of extreme, i.e., $F_{\max}(q) = P(\max_{t\in D} Q(t) \leq q)$, is of particular interest since it is crucial for reliability analysis in the practical applications. It is shown that the translation model provides the best approximation on the distribution of extreme. Its performance is superior if the dependence between simultaneously large values of $Q(t)$ at different time points is weak. Yet, when such dependence is strong, the translation model performs poorly. To address this issue, we propose a new non-Gaussian model that is based on the higher-order Markov

process. The finite dimensional distributions of the Markov process are characterized in terms of copulas whose parameters are selected by optimization algorithms such that the resulting model fits best the specified quantities of interest. This model can be viewed as the extension of the works in [10, 6, 31]. Theoretical arguments and numerical examples are presented to show that the model matches the marginal distribution of the target process $Q(t)$ and is flexible enough to approximate satisfactorily the combinations of the quantities of interest, including the distribution of extreme. We also apply this model to the simulation of a wind pressure process obtained from the wind tunnel experiment to illustrate its practical use.

The outline of the remaining sections is as follows. In section 3.3, we provide the review of the non-Gaussian models. Section 3.4 describes the construction of the copula-based Markov model and the algorithm of model calibration. The numerical examples are in section 3.5.

3.3 Review of non-Gaussian models for stochastic processes

Let $Q(t), t \in [0, \tau^*]$, denote a $\mathbb{R}$-valued zero-mean stationary process, where $[0, \tau^*]$ is a bounded time interval. Three types of non-Gaussian models for $Q(t)$, namely third-order spectral representation method (SRM), polynomial chaos, and translation model, are of interest. The constructions and properties of these models are summarized in this section. Note that the higher-order extension of Karhunen-Loéve representation in [46] is not considered in this work as its properties are analogous to those of the translation model. The connection and comparison between these two models can be found in [39].

3.3.1 Third-order SRM

Third-order SRM is first introduced in [51] and has been successfully applied to various stochastic processes. Suppose that stochastic process $Q(t)$ can be partially specified by the correlation function $r(\tau) = E[Q(t+\tau)Q(t)]$ with two-sided spectral density $S(\omega) = \int_{\mathcal{R}} r(\tau)\exp(-i\omega\tau)d\tau/2\pi$, and the third-order cumulant function $c(\tau_1,\tau_2) = E[Q(t)Q(t+\tau_1)Q(t+\tau_2)]$ with bispectrum $B(\omega_1,\omega_2) = \iint_{\mathcal{R}^2} c(\tau_1,\tau_2)\exp[-i(\omega_1\tau_1 + \omega_2\tau_2)]d\tau_1 d\tau_2/4\pi^2$. It is further assumed that $S(\omega)$ only have values in $[-\omega^*,\omega^*]$ and $B(\omega_1,\omega_2)$ in the first quadrant is bounded by $[0,\omega^*]\times[0,\omega^*]$, $0 < \omega^* < \infty$, respectively. Denote by $\{\omega_k, k = 1,\ldots,m\}$ an even partition of the interval $[0,\omega^*]$, where $0 < \omega_1 < \cdots < \omega_m = \omega^*$, with $\Delta\omega_1 = (\omega_1+\omega_2)/2$, $\Delta\omega_k = (\omega_{k+1}-\omega_{k-1})/2$, $k = 2,\ldots,m-1$, and $\Delta\omega_m = (\omega_m - \omega_{m-1})/2$. The third-order SRM has the form

$$\tilde{Q}_m^{SR}(t) = \sum_{k=1}^{m}\Big\{2\sqrt{S_p(\omega_k)\Delta\omega_k}\cos(\omega_k t - \psi_k) + \sum_{\omega_i+\omega_j=\omega_k}^{\omega_i\geq\omega_j>0} 2\sqrt{S(\omega_k)\Delta\omega_k b_p^2(\omega_i,\omega_j)}\cos[\omega_k t - (\psi_i+\psi_j+\beta(\omega_i,\omega_j))]\Big\}, \quad (3.3)$$

where $\{\psi_k, k = 1,\ldots,m\}$ are independently uniformly distributed random variables in the range $[0,2\pi]$, $\beta(\omega_i,\omega_j) = \arctan[\Im(B(\omega_i,\omega_j))/\Re(B(\omega_i,\omega_j))]$ is the phase of the bispectrum, in which $\Im(B(\omega_i,\omega_j))$, $\Re(B(\omega_i,\omega_j))$ denote the imaginary and real parts of $B(\omega_i,\omega_j)$, and $b_p^2(\omega_i,\omega_j)$ and $S_p(\omega_k)$ are the so-called partial bicoherence and pure-power spectrum which have the expressions

$$b_p^2(\omega_i,\omega_j) = \frac{|B(\omega_i,\omega_j)|^2\Delta\omega_i\Delta\omega_j}{S_p(\omega_i)S_p(\omega_j)S(\omega_i+\omega_j)\Delta(\omega_i+\omega_j)}, \quad (3.4)$$

$$S_p(\omega_k) = S(\omega_k)[1 - \sum_{\omega_i+\omega_j=\omega_k}^{\omega_i\geq\omega_j>0} b_p^2(\omega_i,\omega_j)]. \quad (3.5)$$

Partial bicoherence and pure-power spectrum correspond to the contributions of wave interactions and waves with single frequencies. Detailed descriptions

on these two quantities can be found in [51](p. 4). It is also worth noting that a first glimpse of Eqs. 3.4 and 3.5 seems to suggest that $b_p^2(\omega_i, \omega_j)$ must be obtained in order to calculate $S_p(\omega_k)$ and vice versa. However, they can be constructed together in a term-by-term fashion, starting to calculate $S_p(\omega_1)$, $b_p^2(\omega_1, \omega_1)$, $S_p(\omega_2)$ and so on. We now investigate the properties of this model which are first proved in [51]. We present the alternative proofs here.

Property 1: $\tilde{Q}_m^{SR}(t)$ has mean zero.

This property follows readily from taking expectation on both sides of Eq. 3.3, i.e.,

$$E[\tilde{Q}_m^{SR}(t)] = \sum_{k=1}^{m} \Big\{ 2\sqrt{S_p(\omega_k)\Delta\omega_k} E[\cos(\omega_k t - \psi_k)] + \sum_{\omega_i+\omega_j=\omega_k}^{\omega_i \geq \omega_j > 0} 2\sqrt{S(\omega_k)\Delta\omega_k b_p^2(\omega_i, \omega_j)} E[\cos(\omega_k t - (\psi_i + \psi_j + \beta(\omega_i, \omega_j)))] \Big\}. \quad (3.6)$$

Since $E[\cos(\omega_k t - \psi_k)] = 0$ and $E[\cos(\omega_k t - (\psi_i + \psi_j + \beta(\omega_i, \omega_j)))] = 0, \forall \psi_k, \psi_i, \psi_j$, $i, j, k = 1, \ldots, m$, we have $E[\tilde{Q}_m^{SR}(t)] = 0$.

Property 2: $\tilde{Q}_m^{SR}(t)$ converges to $Q(t)$ in the second and the third moment sense as $m \to \infty$.

The proof of the second-moment convergence is from the fact that

$$\begin{aligned} & E[\tilde{Q}_m^{SR}(t+\tau)\tilde{Q}_m^{SR}(t)] \\ = & \sum_{k=1}^{m}\sum_{l=1}^{m} 4\sqrt{S_p(\omega_k)S_l(\omega_l)\Delta\omega_k\Delta\omega_l} E[\cos(\omega_k(t+\tau) - \psi_k)\cos(\omega_l t - \psi_l)] \\ & + \sum_{k=1}^{m}\sum_{l=1}^{m} \sum_{\omega_i+\omega_j=\omega_k}^{\omega_i \geq \omega_j > 0} \sum_{\omega_i'+\omega_j'=\omega_l}^{\omega_i' \geq \omega_j' > 0} 4\sqrt{S(\omega_k)\Delta\omega_k b_p^2(\omega_i, \omega_j) S(\omega_l)\Delta\omega_l b_p^2(\omega_i', \omega_j')} \\ & E[\cos(\omega_k(t+\tau) - (\psi_i + \psi_j + \beta(\omega_i, \omega_j)))\cos(\omega_l t - (\psi_i' + \psi_j' + \beta(\omega_i', \omega_j')))]. \quad (3.7) \end{aligned}$$

Note that the first term is non-zero only if $k = l$, i.e.,

$$\begin{aligned}
&\sum_{k=1}^{m}\sum_{l=1}^{m} 4\sqrt{S_p(\omega_k)S_l(\omega_l)\Delta\omega_k\Delta\omega_l}E[\cos(\omega_k(t+\tau)-\psi_k)\cos(\omega_l t-\psi_l)] \\
=&\sum_{k=1}^{m} 4S_p(\omega_k)\Delta\omega_k E[\cos(\omega_k(t+\tau)-\psi_k)\cos(\omega_k t-\psi_k)] \\
=&\sum_{k=1}^{m} 2S_p(\omega_k)\Delta\omega_k\cos(\omega_k\tau). \qquad (3.8)
\end{aligned}$$

In the second term, the non-zero expectations arise when $k = l$, $i = i'$, and $j = j'$. The second term then becomes

$$\begin{aligned}
&\sum_{k=1}^{m}\sum_{\omega_i+\omega_j=\omega_k}^{\omega_i\geq\omega_j>0} 2S(\omega_k)\Delta\omega_k b_p^2(\omega_i,\omega_j)\cos(\omega_k\tau) \\
=&\sum_{k=1}^{m} 2S(\omega_k)\Delta\omega_k\cos(\omega_k\tau)\sum_{\omega_i+\omega_j=\omega_k}^{\omega_i\geq\omega_j>0} b_p^2(\omega_i,\omega_j). \qquad (3.9)
\end{aligned}$$

From the definition of $S_p(\omega_k)$, we have

$$\begin{aligned}
&E[\tilde{Q}_m^{SR}(t+\tau)\tilde{Q}_m^{SR}(t)] = \sum_{k=1}^{m} 2S_p(\omega_k)\Delta\omega_k\cos(\omega_k\tau) \\
&+\sum_{k=1}^{m} 2S(\omega_k)\Delta\omega_k\cos(\omega_k\tau)\sum_{\omega_i+\omega_j=\omega_k}^{\omega_i\geq\omega_j>0} b_p^2(\omega_i,\omega_j) = \sum_{k=1}^{m} 2S(\omega_k)\Delta\omega_k\cos(\omega_k\tau). \qquad (3.10)
\end{aligned}$$

The expression in Eq. 3.10 is the Riemann sum of $r(\tau) = \int_0^\infty 2S(\omega)\cos(\omega\tau)d\omega$ which converges to $r(\tau)$ as $m \to \infty$. The property that $\tilde{Q}_m^{SR}(t)$ converges to $Q(t)$ in the third moment sense can be shown similarly and the proof is given in Appendix A.

Property 3: $\tilde{Q}_m^{SR}(t)$ is weakly stationary.

This property follows directly from Property 1 and the observation that the correlation function of $\tilde{Q}_m^{SR}(t)$ in Eq. 3.10 only depends on time lag τ.

In summary, third-order SRM extends the traditional second-order SRM by introducing partial bicoherence and pure-power spectrum, which decouple the contributions of wave interactions and waves with single frequencies.

This model has mean zero and is weakly stationary. It converges to the target stochastic process in the second and the third moment sense. However, this model cannot distinguish between processes with the same third moment and is not able to match exactly the marginal distribution of $Q(t)$. This may result in large discrepancies in the tail of the distribution which may have a profound effect on the estimate of distribution of extreme based on this model, as illustrated in the numerical example.

3.3.2 Polynomial chaos

Under the assumption that $Q(t)$ is a stationary stochastic process with mean zero and finite correlation function $r(\tau) = E[Q(t+\tau)Q(t)]$, the infinite series [49]

$$Q(t) = \sum_{k=0}^{\infty} \beta_k h_k(G(t)) \tag{3.11}$$

constitutes the polynomial chaos representation for $Q(t)$, where $\{\beta_k\}$ are the deterministic coefficients that need to be determined, $G(t)$ is a zero-mean, unit variance Gaussian process with correlation function $\rho(\tau) = E[G(t+\tau)G(t)]$, and

$$h_k(x) = (-1)^k e^{-\frac{x^2}{2}} \frac{d^k}{dx^k} e^{-\frac{x^2}{2}} \tag{3.12}$$

are the one-dimensional Hermite polynomials. The collection $\{h_k(G(t))\}$ have means zero except that
$E[h_0(G(t))] = 1$ and satisfy the orthogonalities with respect to the probability measure, i.e.,

$$E[h_k(G(t))h_l(G(t))] = k!\,\delta_{kl}, \tag{3.13}$$

where δ_{kl} denotes the Kronecker delta. From the properties of Gaussian random variables [18](p. 383), Eq. 3.13 can be further extended as

$$E[h_k(G(t+\tau))h_l(G(t))] = k!\rho^k(\tau)\ \delta_{kl}. \tag{3.14}$$

We note that the representation in Eq. 3.11 is completely defined by $\{\beta_k\}$ and $\rho(\tau)$ which can be evaluated by using the orthogonalities in Eqs. 3.13 and 3.14. More specifically, the coefficients $\{\beta_k\}$ are calculated according to the equation

$$\beta_k = \frac{1}{k!}E[Q(t)h_k(G(t))], \tag{3.15}$$

since $E[Q(t)h_k(G(t))] = \sum_{l=0}^{\infty}\beta_l E[h_k(G(t))h_l(G(t))] = \beta_k k!$, and the correlation function $\rho(\tau)$ of $G(t)$ is the solution to the polynomial equation

$$r(\tau) = E[Q(t+\tau)Q(t)] = \sum_{k=0}^{\infty}\sum_{l=0}^{\infty}\beta_k\beta_l E[h_k(G(t+\tau))h_l(G(t))] = \sum_{k=0}^{\infty}\beta_k^2 k!\rho^k(\tau). \tag{3.16}$$

Eqs. 3.15 and 3.16 also indicate that $\beta_0 = E[Q(t)] = 0$, and the variance of $Q(t)$, $r(0) = E[Q^2(t)] = \sum_{k=0}^{\infty}{\beta_k}^2 k!$.

By retaining the first m terms of the series, Eq. 3.11 yields

$$Q(t) \approx \tilde{Q}_m^{PC}(t) = \sum_{k=0}^{m}\beta_k h_k(G(t)), \tag{3.17}$$

which is defined as the polynomial chaos approximation for $Q(t)$. We present and prove the properties of $\tilde{Q}_m^{PC}(t)$. Some of the proofs can also be found in [13].

Property 1: From direct derivation, the second-moment properties of $\tilde{Q}_m^{PC}(t)$

are given by

$$E[\tilde{Q}_m^{PC}(t)] = \sum_{k=0}^{m} \beta_k E[h_k(G(t))] = \beta_0 = 0, \tag{3.18}$$

$$E[\tilde{Q}_m^{PC^2}(t)] = \sum_{k=0}^{m}\sum_{l=0}^{m} \beta_k\beta_l E[h_k(G(t))h_l(G(t))] = \sum_{k=0}^{m} \beta_k^2 k!, \tag{3.19}$$

$$E[\tilde{Q}_m^{PC}(t+\tau)\tilde{Q}_m^{PC}(t)] = \sum_{k=0}^{m}\sum_{l=0}^{m} \beta_k\beta_l E[h_k(G(t+\tau))h_l(G(t))] = \sum_{k=0}^{m} \beta_k^2 k!\rho^k(\tau), \tag{3.20}$$

which converge to the corresponding second-moment properties of $Q(t)$ as $m \to \infty$.

Property 2: $\tilde{Q}_m^{PC}(t)$ converges to $Q(t)$ in L^2, $\forall t$.

This property follows from

$$\begin{aligned}\lim_{m\to\infty} E[(\tilde{Q}_m^{PC}(t) - Q(t))^2] &= E[Q^2(t)] + \lim_{m\to\infty}(E[\tilde{Q}_m^{PC^2}(t)] - 2E[\tilde{Q}_m^{PC}(t)Q(t)]) \\ &= \sum_{k=0}^{\infty} \beta_k^2 k! + \lim_{m\to\infty}(\sum_{k=0}^{m} \beta_k^2 k! - 2\sum_{k=0}^{m} \beta_k^2 k!) = \lim_{m\to\infty} \sum_{k\geq m+1}^{\infty} \beta_k^2 k! = 0,\end{aligned} \tag{3.21}$$

provided that $E[\tilde{Q}_m^{PC}(t)Q(t)] = \sum_{k=0}^{m}\sum_{l=0}^{\infty} \beta_k\beta_l E[h_k(G(t))h_l(G(t))] = \sum_{k=0}^{m} \beta_k^2 k!$. This property also implies the convergence in distribution, that is, the marginal distribution of $\tilde{Q}_m^{PC}(t)$ converges to that of $Q(t)$ as m increases.

Property 3: The finite dimensional distribution of $\tilde{Q}_m^{PC}(t)$ converges to the corresponding finite dimensional distribution of $Q(t)$ as $m \to \infty$.

The above statement holds if and only if $\sum_{j=1}^{n} y_j \tilde{Q}_m^{PC}(t_j) \xrightarrow{d} \sum_{j=1}^{n} y_j Q(t_j)$ for each $(y_1, \ldots, y_n) \in \mathcal{R}^n$, where $t_1, \ldots, t_n$ are n arbitrary distinct time points [32] (Theorem 2.14). Hence, it suffices to show that

$$\sum_{j=1}^{n} y_j \tilde{Q}_m^{PC}(t_j) \xrightarrow{L^2} \sum_{j=1}^{n} y_j Q(t_j), \tag{3.22}$$

for every $(y_1, \ldots, y_n) \in \mathcal{R}^n$. From the definition of the L_2 convergence of a random variable, we have

$$\begin{aligned} & E\Big[\Big(\sum_{j=1}^{n} y_j(\tilde{Q}_m^{PC}(t_j) - Q(t_j))\Big)^2\Big] \\ =& \sum_{i=1}^{n}\sum_{j=1}^{n} y_i y_j E[(\tilde{Q}_m^{PC}(t_i) - Q(t_i))(\tilde{Q}_m^{PC}(t_j) - Q(t_j))], \end{aligned}$$

which is bounded above by

$$\begin{aligned} & E\Big[\Big(\sum_{j=1}^{n} y_j(\tilde{Q}_m^{PC}(t_j) - Q(t_j))\Big)^2\Big] \\ \leq& \sum_{i=1}^{n}\sum_{j=1}^{n} y_i y_j E[(\tilde{Q}_m^{PC}(t_i) - Q(t_i))^2]E[(\tilde{Q}_m^{PC}(t_j) - Q(t_j))^2] \to 0, \end{aligned} \tag{3.23}$$

resulted from Cauchy-Schwarz inequality and Eq. 3.21.

Even though we have shown that $\tilde{Q}_m^{PC}(t)$ exhibits convergence in L^2 and in finite dimensional distribution, it has been pointed out in [13] that $\tilde{Q}_m^{PC}(t)$ is not stationary and the higher-order marginal moments (greater than two) of $\tilde{Q}_m^{PC}(t)$ may or may not converge as m grows. It may result in a slow convergence on the tail of the distribution of $\tilde{Q}_m^{PC}(t)$. As a consequence, the estimate of the distribution of extreme based on $\tilde{Q}_m^{PC}(t)$ can have large errors, even when m is large. Moreover, the development of $\tilde{Q}_m^{PC}(t)$ may be computational demanding, or even prohibitive, because of the large number of coefficients that need to be calculated [14].

3.3.3 Translation model

Recall that $Q(t)$ is a stationary stochastic process with mean zero and correlation function $r(\tau) = E[Q(t+\tau)Q(t)]$. Denote by $F(q) = P(Q(t) \leq q)$ the marginal

distribution of $Q(t)$. It is commonly assumed that F is continuous in practical applications. The translation model $\tilde{Q}_T(t)$ has the expression [18]

$$Q(t) \approx \tilde{Q}_T(t) = h(G(t)) = F^{-1} \circ \Phi(G(t)), \tag{3.24}$$

where $h = F^{-1} \circ \Phi$, F^{-1} denotes the inverse of F which exists because of the assumed continuity of F, Φ is the distribution of the standard Gaussian variable $N(0,1)$, and $G(t)$ is a stationary Gaussian process with mean zero, variance one, and correlation function $\rho(\tau) = E[G(t+\tau)G(t)]$. The probability law of $\tilde{Q}_T(t)$ is completely specified by F and $\rho(\tau)$, where the correlation function $\rho(\tau)$ can be obtained through the following equation

$$r(\tau) = \int_{-\infty}^{\infty} \int_{-\infty}^{\infty} h(g_1)h(g_2)\phi(g_1, g_2; \rho(\tau))dg_1 dg_2, \tag{3.25}$$

in which $\phi(g_1, g_2; \rho(\tau))$ is the density of a bivariate standard Gaussian vector with correlation coefficient $\rho(\tau)$, i.e.,

$$\phi(g_1, g_2; \rho(\tau)) = \frac{1}{2\pi\sqrt{1-\rho^2(\tau)}} \exp\Big(- \frac{g_1^2 + g_2^2 - 2\rho(\tau)g_1 g_2}{2(1-\rho^2(\tau))}\Big). \tag{3.26}$$

Properties of the translation model $\tilde{Q}_T(t)$ are provided next. The proofs of properties 1 and 3 are taken from [18].

Property 1: The translation model $\tilde{Q}_T(t)$ is stationary and has marginal distributions F.

The first property holds since

$$\begin{aligned}
&P(\tilde{Q}_T(t_1) \le q_1, \ldots, \tilde{Q}_T(t_n) \le q_n) = P(\cap_{i=1}^n \{\tilde{Q}_T(t_i) \le q_i\}) \\
=&P(\cap_{i=1}^n \{h(G(t_i)) \le q_i\}) = P(\cap_{i=1}^n \{G(t_i) \le h^{-1}(q_i)\}) \\
=&P(\cap_{i=1}^n \{G(t_i+\tau) \le h^{-1}(q_i)\}) = P(\cap_{i=1}^n \{h(G(t_i+\tau)) \le q_i\}) \\
=&P(\cap_{i=1}^n \{\tilde{Q}_T(t_i+\tau) \le q_i\}),
\end{aligned} \tag{3.27}$$

for arbitrary $t_1, \ldots, t_n, \tau$. The above equalities follow from the fact that Gaussian process $G(t)$ is stationary and function h is invertible because it is continuous and strictly increasing. The latter property is true since $P(\tilde{Q}_T(t) \leq q) = P(F^{-1} \circ \Phi(G(t)) \leq q) = P(\Phi(G(t)) \leq F(q)) = F(q)$, provided that $\Phi(G(t))$ is a uniform random variable. It is also worth noting that since the translation model matches exactly the marginal distribution, it can be regarded as the limit of the polynomial chaos approximation at a fixed time as the truncation level approaches infinity.

Property 2: Simultaneously large values of the translation model $\tilde{Q}_T(t)$ at different time points are independent [58].

This statement is equivalent to the following equation

$$\lim_{u_1,\ldots,u_n \to 1} \left| P(\cap_{i=1}^n \{\tilde{Q}_T(t_i) \leq F^{-1}(u_i)\}) - \prod_{i=1}^n u_i \right| = 0, \tag{3.28}$$

where $t_1, \ldots, t_n$ are n distinct time arguments. From the definition of the translation model, Eq. 3.28 yields

$$\begin{aligned} &\lim_{u_1,\ldots,u_n \to 1} \left| P(\cap_{i=1}^n \{\tilde{Q}_T(t_i) \leq F^{-1}(u_i)\}) - \prod_{i=1}^n u_i \right| \\ &= \lim_{u_1,\ldots,u_n \to 1} \left| P(\cap_{i=1}^n \{F^{-1}[\Phi(G(t_i))] \leq F^{-1}(u_i)\}) - \prod_{i=1}^n u_i \right| \\ &= \lim_{u_1,\ldots,u_n \to 1} \left| P(\cap_{i=1}^n \{G(t_i) \leq \Phi^{-1}(u_i)\}) - \prod_{i=1}^n u_i \right| = 0. \end{aligned} \tag{3.29}$$

The proof of Eq. 3.29 follows from (1) the corollary to the Normal Comparison Lemma which states that [41]

$$\left| P(\cap_{i=1}^n \{G(t_i) \leq \Phi^{-1}(u_i)\}) - \prod_{i=1}^n u_i \right| \leq \frac{1}{4} \sum_{1 \leq k < j \leq n} |\rho_{kj}| \exp\left[-\frac{\Phi^{-1}(u_k)^2 + \Phi^{-1}(u_j)^2}{2(1 + |\rho_{kj}|)} \right], \tag{3.30}$$

where ρ_{kj} is the covariance between $G(t_k)$ and $G(t_j)$, and (2) the observation that

the upper bound in Eq. 3.30 approaches zero as $u_1, \ldots, u_n \to 1$. This property is referred to as the tail independence of the translation model.

Property 3: The correlation function $\rho(\tau)$ of $G(t)$ may or may not exist to match the prescribed marginal distribution F and correlation function $r(\tau)$ of $Q(t)$. The translation model has exact or approximate second-moment properties of $Q(t)$, respectively.

The pair $(F, r(\tau))$ is said to be inconsistent if $\rho(\tau)$ does not exist [19, 16]. There are two types of inconsistencies that can occur between a given marginal distributions F and a prescribed correlation function $r(\tau)$. The first type arises when $r(\tau)$ has certain values which lie outside of the admissible range $[r^L, r^U]$, where G is a Gaussian random variable, and

$$r^L = E[h(G)h(-G)], \;\; r^U = E[h(G)h(G)]. \tag{3.31}$$

This admissible range results from (1) the Price Theorem which states that [22]

$$\frac{\partial r(\tau)}{\partial \rho(\tau)} = E\Big[\frac{dh(G(t+\tau))}{dG(t+\tau)} \frac{dh(G(t))}{dG(t)}\Big] > 0, \tag{3.32}$$

since the function h is strictly increasing for continuous F, and (2) the definition of $r(\tau)$ which shows that

$$r(\tau) = \begin{cases} E[h(G)h(-G)] & \text{if } \rho(\tau) = -1, \\ E[h(G)h(G)] & \text{if } \rho(\tau) = 1. \end{cases} \tag{3.33}$$

The second type of inconsistency occurs when the resulting correlation function $\rho(\tau)$ from Eq. 3.25 is not positive semi-definite. Examples of these inconsistencies are given in [18](p. 52).

Simulation algorithms have been developed for constructing translation models such that, for consistent pairs $(F, r(\tau))$, match F and $r(\tau)$, and, for inconsistent pairs $(F, r(\tau))$, match F and approximate $r(\tau)$. These algorithms involve

(1) direct transformation which estimates the correlation function $\rho(\tau)$, provided that it exists, from samples of $G(t)$ obtained from the inverse map h^{-1} of samples of $Q(t)$ [28]; (2) iterative schemes which iteratively upgrade $\rho(\tau)$ so that the error between resulting and target correlation functions of $Q(t)$ is within an acceptable tolerance [56, 11, 3, 50]; or (3) optimization approaches which find the optimal $\rho(\tau)$ by minimizing the error on $r(\tau)$ [19]. A detailed summary of these simulation algorithms can be found in [50].

After providing a review of three types of non-Gaussian models, a comparison of their key features is summarized in Table. 3.1. The accuracies on the estimates of distributions of extremes based on these three models are examined in the first numerical example in section 4. It is shown that the translation model provides the best approximation on the distribution of extreme, especially when the dependence between simultaneously large values of target process at different time points is weak. However, when such tail dependence grows, the accuracy of the approximation from translation model exacerbates. This observation results from the second property of the translation model. In the next section, we present an alternative non-Gaussian model which is based on the higher-order Markov process to overcome this limitation.

	Stationarity	Second-moment properties	Third-moment properties	Marginal distribution	Finite dimensional distribution
Third-order SRM	Weakly	✓	✓	✗	✗
Polynomial chaos	✗	$\approx$ (Approximate)	✗	$\approx$	$\approx$
Translation model	Strictly	✓ or $\approx$	✗	✓	✗

Table 3.1: Comparison of non-Gaussian models for stochastic process

3.4 Copula-based Markov model for stochastic processes

Recall that $Q(t),\ t \in [0, \tau^*]$, is a stationary stochastic process with mean zero, correlation function $r(\tau)$, and marginal distribution $F(q)$. In this section, we develop a new non-Gaussian model for $Q(t)$. The model aims to not only match the marginal distribution $F(q)$ and approximate the correlation function $r(\tau)$ of $Q(t)$ but also capture the information beyond them, e.g., the joint distribution at different times, the distribution of extreme, and the mean crossing rate of $Q(t)$. We refer to these statistical quantities as the quantities of interest. The objective can be achieved by representing $Q(t)$ as a m-th order Markov process $\tilde{Q}_m^M(t)$. Let $0 = t_1 < \cdots < t_n = \tau^*$ be n distinct time arguments which evenly partition the time interval $[0, \tau^*]$. The m-th order Markov process is defined such that the conditional random variables $(\tilde{Q}_m^M(t_i)|\tilde{Q}_m^M(t_{i-1}), \ldots, \tilde{Q}_m^M(t_{i-m}))$ and $(\tilde{Q}_m^M(t_{i-m-1}), \ldots, \tilde{Q}_m^M(t_1)|\tilde{Q}_m^M(t_{i-1}), \ldots, \tilde{Q}_m^M(t_{i-m}))$ are independent for $i = m+1, \ldots, n$ [31]. Under the assumption that the joint density of the random vector $[\tilde{Q}_m^M(t_1), \ldots, \tilde{Q}_m^M(t_n)]^T$ exists, the definition of $\tilde{Q}_m^M(t)$ implies that

$$f_{i|i-1,\ldots,1}(q_i|q_{i-1}, \ldots, q_1) = f_{i|i-1,\ldots,i-m}(q_i|q_{i-1}, \ldots, q_{i-m}), \tag{3.34}$$

where the subscripts of f indicate the reference random variables. For example, the function $f_{i|i-1,\ldots,i-m}$ is the density of $(\tilde{Q}_m^M(t_i)|\tilde{Q}_m^M(t_{i-1}), \ldots, \tilde{Q}_m^M(t_{i-m}))$. The proof of Eq. 3.34 is the straightforward extension of the proof in [24] (p. 121). Eq. 3.34 suggests that conditional random variables $(\tilde{Q}_m^M(t_i)|\tilde{Q}_m^M(t_{i-1}), \ldots, \tilde{Q}_m^M(t_1))$ and $(\tilde{Q}_m^M(t_i)|\tilde{Q}_m^M(t_{i-1}), \ldots, \tilde{Q}_m^M(t_{i-m}))$ have the same density $f_{i|i-1,\ldots,i-m}$, referred to as the transition density. Hence, $\tilde{Q}_m^M(t)$ can

be defined at distinct time arguments $t_i, i = 1, \ldots, n$, and has the form

$$\begin{aligned} \tilde{Q}_m^M(t_1) &= F^{-1}(U_1), \\ \tilde{Q}_m^M(t_i) &= F^{-1}_{i|i-1,\ldots,\max(1,i-m)}(U_i),\ i = 2, \ldots, n, \end{aligned} \tag{3.35}$$

where $U_i, i = 1, \ldots, n$, are independent uniform random variables, and $F_{i|i-1,\ldots,\max(1,i-m)}$ denote the distributions of conditional random variables $(\tilde{Q}_m^M(t_i)|\tilde{Q}_m^M(t_{i-1}), \ldots, \tilde{Q}_m^M(t_{\max(1,i-m)}))$ with corresponding densities $f_{i|i-1,\ldots,\max(1,i-m)}$. From Eq. 3.35, the samples of $\tilde{Q}_m^M(t)$ are generated in a sequential manner, i.e., starting to obtain $\tilde{Q}_m^M(t_1)$, calculating the conditional distribution $F_{2|1}$, then generating $\tilde{Q}_m(t_2)$ from $F^{-1}_{2|1}(U_2)$ and so on.

The construction of the model $\tilde{Q}_m^M(t)$ in Eq. 3.35 requires the knowledge of the transition density, i.e., $f_{i|i-1,\ldots,i-m}(q_i|q_{i-1}, \ldots, q_{i-m})$, or equivalently the joint distribution at m consecutive times $F_{1,\ldots,m}(q_1, \ldots, q_m)$. In this work, we model this joint distribution by m-copula. The parameters of the m-copula are selected such that the resulting model $\tilde{Q}_m^M(t)$ fits best the pre-specified quantities of interest. In the section 3.1, the concepts and examples of the m-copula are presented. The estimation of the parameters of the m-copula is also discussed. Then, we investigate the properties of this copula-based Markov model $\tilde{Q}_m^M(t)$ in section 3.2.

3.4.1 m-copula and estimation of parameters

A m-copula is a multivariate CDF defined in the unit cube $[0, 1]^m$ with uniform marginal distributions. More formally, it is defined as a mapping C: $[0, 1]^m \rightarrow [0, 1]$ with the following properties: [34]

(1) $\forall \boldsymbol{u} = [u_1, \ldots, u_m] \in [0, 1]^m, C(\boldsymbol{u}) = 0$ if at least one coordinate of $\boldsymbol{u}$ equals 0;

(2) $C(\boldsymbol{u}) = u_k$ if all the coordinates of $\boldsymbol{u}$ are equal to 1 except u_k;
(3) $\forall \boldsymbol{a}$ and $\boldsymbol{b} \in [0,1]^m$ such that $a_k \leq b_k$, $k = 1, \ldots, m$, $V_C([\boldsymbol{a}, \boldsymbol{b}]) \geq 0$, where V_C denotes the C-volume defined in [45] (p. 45, def. 2.10.5).

Denote by $\tilde{F}_{1,\ldots,m}(q_1, \ldots, q_m)$ a m-dimensional joint distribution with marginal distribution F. The most important theorem in copula theory, named Sklar's Theorem [27], states that if the marginal distribution F is continuous, then there exists an unique C such that $\forall q_1, \ldots, q_m$,

$$\tilde{F}_{1,\ldots,m}(q_1, \ldots, q_m) = C(F(q_1), \ldots, F(q_m)) = C(u_1, \ldots, u_m), \tag{3.36}$$

where $F(q_k) = u_k$, $k = 1, \ldots, m$. By Sklar's Theorem, the joint distribution $\tilde{F}_{1,\ldots,m}(q_1, \ldots, q_m)$ can be fully captured by m-copula, and so are the marginal distributions. In Table. B.1 and B.2 of Appendix B, we list some commonly-used families of m-copulas, along with the ranges of the parameters, properties, and the corresponding references. It is worth noting that any weighted sum of the m-copulas is also a m-copula. For example, let $C_1(u_1, u_2)$ and $C_2(u_1, u_2)$ be two arbitrary 2-copulas in Table. B.1 and B.2, then $C(u_1, u_2) = \theta C_1(u_1, u_2) + (1 - \theta) C_2(u_1, u_2)$ is another valid 2-copula if $\theta \in [0, 1]$. The copulas shown in the table as well as their weighted sums suffice in practical applications since they can cover a variety of dependence structures.

The parameters of the m-copula are grouped into a vector, denoted by Θ. The optimal group of parameters is selected such that the discrepancies on the quantities of interest are minimized. In other words, Θ is the solution of the optimization problem

$$\min_{\Theta} \{e(\Theta)\}, \tag{3.37}$$

where $e(\Theta) = \sum_j \alpha_j e_j(\Theta)$ measures the errors between quantities of interest of $Q(t)$ and $\tilde{Q}_m(t)$, and $\alpha_j \geq 0$ are weighting factors which are tuned to prioritize

$e_j(\Theta)$ according to their hierarchy of importance. Some examples of $e_j(\Theta)$ are shown in Table. 3.2.

Correlation functions	$e_1(\Theta) = \int_{[0,\tau^*]}(r(\tau) - \tilde{r}(\tau))^2 d\tau$
Third-order cumulant functions	$e_2(\Theta) = \int_{[0,\tau^*]^2}(c(\tau_1,\tau_2) - \tilde{c}(\tau_1,\tau_2))^2 d\tau_1 d\tau_2$
Joint distributions at consecutive times	$e_3(\Theta) = \int_{\mathbb{R}^m}(F_{1,\ldots,m}(q_1,\ldots,q_m) - \tilde{F}_{1,\ldots,m}(q_1,\ldots,q_m))^2 dq_1 \cdots dq_m$
Distributions of extremes	$e_4(\Theta) = \int_{\mathbb{R}}(F_{\max}(q) - \tilde{F}_{\max}(q))^2 dq$
Mean crossing rates	$e_5(\Theta) = \int_{\mathbb{R}}(\nu(q) - \tilde{\nu}(q))^2 dq$

Notes: 1. The quantities with $\sim$ and without $\sim$ are estimated from the model $\tilde{Q}_m^M(t)$ and the target process $Q(t)$.
2. The definition of mean crossing rates can be found in [24] (p. 165).

Table 3.2: Examples of quantities of interest

3.4.2 Properties of the copula-based Markov model $\tilde{Q}_m^M(t)$

We now investigate the properties of $\tilde{Q}_m^M(t)$.

Property 1: The Copula-based Markov model $\tilde{Q}_m^M(t)$ preserves the marginal distribution of $Q(t)$, and the finite dimensional densities of $\tilde{Q}_m^M(t)$ are defined completely by the marginal and transition densities.

We prove the second part of the property. Let $i_1 < i_2 < \cdots < i_l$ be l consecutive integers from set $\{1, \ldots, n\}$. If $l > m$, we have

$$\begin{aligned} f_{i_1,\ldots,i_l}(q_1, \ldots, q_l) &= f_{i_l|i_{l-1},\ldots,i_1}(q_l|q_{l-1}, \ldots, q_1) f_{i_1,\ldots,i_{l-1}}(q_1, \ldots, q_{l-1}) \\ &= f_{i_l|i_{l-1},\ldots,i_{l-m}}(q_l|q_{l-1}, \ldots, q_{l-m}) f_{i_1,\ldots,i_{l-1}}(q_1, \ldots, q_{l-1}). \end{aligned}$$

Repeated use of the above formula gives

$$f_{i_1,\ldots,i_l}(q_1, \ldots, q_l) = f(q_1) \prod_{j=2}^{l} f_{i_j|i_{j-1},\ldots,i_{\max(j-m,1)}}(q_j|q_{j-1}, \ldots, q_{\max(j-m,1)}), \quad (3.38)$$

where f denotes the marginal density of $Q(t)$. If $l \leq m$, then $f_{i_1,\ldots,i_l}(q_1, \ldots, q_l)$ can be matched exactly by the transition density or its marginal densities of order 2 to $m-1$. It is worthy noting that the finite dimensional densities at non-consecutive time arguments can be further obtained via the integrations of those at consecutive time arguments.

Property 2: The Copula-based Markov model $\tilde{Q}_m^M(t)$ is stationary.

It suffices to show the finite dimensional densities in Eq. 3.38 are invariant under arbitrary time shifts. Set $p < n - i_l$ an arbitrary integer. Since the transition

density remains constant under time shift, we have

$$
\begin{aligned}
f_{i_1,\ldots,i_l}(q_1,\ldots,q_l) &= f(q_1)\prod_{j=2}^{l} f_{i_j|i_{j-1},\ldots,i_{\max(j-m,1)}}(q_j|q_{j-1},\ldots,q_{\max(j-m,1)}) \\
&= f(q_1)\prod_{j=2}^{l} f_{i_j+p|i_{j-1}+p,\ldots,i_{\max(j-m,1)}+p}(q_j|q_{j-1},\ldots,q_{\max(j-m,1)}) \\
&= f_{i_1+p,\ldots,i_l+p}(q_1,\ldots,q_l),
\end{aligned}
$$

which completes the proof.

It is also worth noting that Aside from properties 1 and 2, the features of the copula-based Markov model are related to the choices of the quantities of interest in the parameter estimation defined in Eq. 3.37. For example, if the objective function in Eq. 3.37 is selected to be $e(\Theta) = \alpha_1 e_1(\Theta) + \alpha_3 e_3(\Theta)$, where $e_1(\Theta)$ and $e_3(\Theta)$ denote the errors on correlation function and joint distribution which defined in Table. 3.2, then the features of the model are summarized in Table. 3.3. In the next section, the implementation and properties of the copula-based Markov model are illustrated by the numerical examples.

	Stationarity	Second-moment properties	Third-moment properties	Marginal distribution	Finite dimensional distribution
Third-order SRM	Weakly	✓	✓	✗	✗
Polynomial chaos	✗	$\approx$ (Approximate)	✗	$\approx$	$\approx$
Translation model	Strictly	✓ or $\approx$	✗	✓	✗
Copula-based Markov model	Strictly	$\approx$	✗	✓	$\approx$ up to order m

Table 3.3: One example of the features of Markov model

3.5 Numerical examples

Numerical examples are provided to examine the performances of the non-Gaussian models which include third-order SRM, polynomial chaos, translation model, and the copula-based Markov model. In the first example, we calibrate the first three non-Gaussian models introduced in section 2 to the solutions of the stochastic differential equations. The metrics used in the evaluations are correlation function, third-order cumulant function, marginal distribution, and the distribution of extreme. Note that the choices of the test case and metrics provide a fair comparison for the non-Gaussian models. In the second example, we repeat the calibration in Example 1 for copula-based Markov model with two different sets of quantities of interest to illustrate the flexibility and accuracy of the model. In the third example, the copula-based Markov model is applied to a wind pressure process obtained from the wind tunnel experiment to illustrate its practical use. We compare the performances of the copula-based Markov model with the translation model in the second and third examples.

3.5.1 Example 1

Let $Q(t)$ be the solution of a stochastic differential equation driven by the Brownian motion $B(t)$ with linear drift term and diffusion term $b(Q(t))$, i.e., $Q(t)$ satisfies the equation

$$dQ(t) = -\alpha Q(t)dt + b(Q(t))dB(t), \tag{3.39}$$

in which α is a deterministic parameter. The stationary part of $Q(t)$ has mean zero, exponential correlation and third-order cumulant functions irrespective of

the functional form of the diffusion term $b(Q(t))$, that is,

$$\gamma_1 = E[Q(t)] = 0, \tag{3.40}$$

$$\frac{r(\tau)}{\gamma_2} = \frac{E[Q(t+\tau)Q(t)]}{E[Q^2(t)]} = \exp(-\alpha\tau), \text{ and} \tag{3.41}$$

$$\frac{c(\tau_1,\tau_2)}{\gamma_3} = \frac{E[Q(t)Q(t+\tau_1)Q(t+\tau_2)]}{E[Q^3(t)]} = \begin{cases} \exp[-\alpha \max(|\tau_1|,|\tau_2|)], & \text{if } \tau_1\tau_2 \geq 0 \\ \exp[-\alpha(|\tau_1|+|\tau_2|)], & \text{if } \tau_1\tau_2 < 0, \end{cases} \tag{3.42}$$

where γ_1, γ_2, and γ_3 are the mean, variance, and skewness of $Q(t)$, respectively. By applying Itô's formula to the mapping $Q(t) \mapsto Q(t)$ in the time interval $[t, t+\tau]$, we have

$$Q(t+\tau) - Q(t) = \int_t^{t+\tau} dQ(v) = \int_t^{t+\tau} -\alpha Q(v)dv + b(Q(v))dB(v). \tag{3.43}$$

Eq. 3.40 follows from taking expectation on Eq. 3.43 and the property of conditional expectation that $E[b(Q(v))dB(v)]$
$= E\big\{E[b(Q(v))dB(v)|\mathcal{F}_v]\big\} = E\big\{b(Q(v))E[dB(v)|\mathcal{F}_v]\big\} = 0$, where $\mathcal{F}_v$ is the natural filtration of $B(u), 0 \leq u \leq v$. Eq. 3.41 can be obtained by multiplying Eq. 3.43 with $Q(t)$, i.e.,

$$Q(t+\tau)Q(t) - Q(t)Q(t) = \int_t^{t+\tau} -\alpha Q(t)Q(v)dv + Q(t)b(Q(v))dB(v).$$

The average of the above equation gives

$$r(\tau) - r(0) = \int_t^{t+\tau} -\alpha r(v-t)dv, \tag{3.44}$$

since $E[Q(t)b(Q(v))dB(v)] = E\big\{Q(t)E[b(Q(v))dB(v)|\mathcal{F}_t]\big\}$
$= E\big\{Q(t)E\{E[b(Q(v))dB(v)|\mathcal{F}_v]|\mathcal{F}_t\}\big\} = 0$. The differentiation of Eq. 3.44 with respect to τ yields Eq. 3.41 [24](p. 435). Eq. 3.42 can be proved in the same manner.

The diffusion term $b(Q(t))$ relates to the marginal distribution of $Q(t)$ through the stationary Fokker-Planck equation defined in [24](p. 482). We select $b(Q(t))$ to be

$$b(Q(t)) = \frac{\sqrt{b_1(Q(t))b_2(Q(t))}}{\sigma_W}, \tag{3.45}$$

where

$$b_1(Q(t)) = \frac{2\alpha}{f_W(\sigma_W Q(t) + \mu_W)}, \tag{3.46}$$

$$b_2(Q(t)) = \lambda\Gamma\Big(1 + \frac{1}{k}, \Big[\frac{\sigma_W Q(t) + \mu_W}{\lambda}\Big]^k\Big) - \mu_W e^{-((\sigma_W Q(t)+\mu_W)/\lambda)^k}, \tag{3.47}$$

$\Gamma(*,*)$ is the incomplete Gamma function, and f_W is the Weibull density with scale parameter λ, shape parameter k, mean μ_W, and standard deviation σ_W. Then, the marginal density of $Q(t)$, denoted by $f_Q(q)$, is the normalized Weibull density, i.e.,

$$f_Q(q) = \begin{cases} \frac{\sigma_W k}{\lambda}\Big(\frac{\sigma_W x+\mu_W}{\lambda}\Big)^{k-1} \exp\Big[-\Big(\frac{\sigma_W x+\mu_W}{\lambda}\Big)^k\Big], & \text{if } x \geq -\mu_W/\sigma_W \\ 0, & \text{if } x < -\mu_W/\sigma_W. \end{cases} \tag{3.48}$$

We note that $Q(t)$ is bounded below by $-\mu_W/\sigma_W$, referred to as the lower bound.

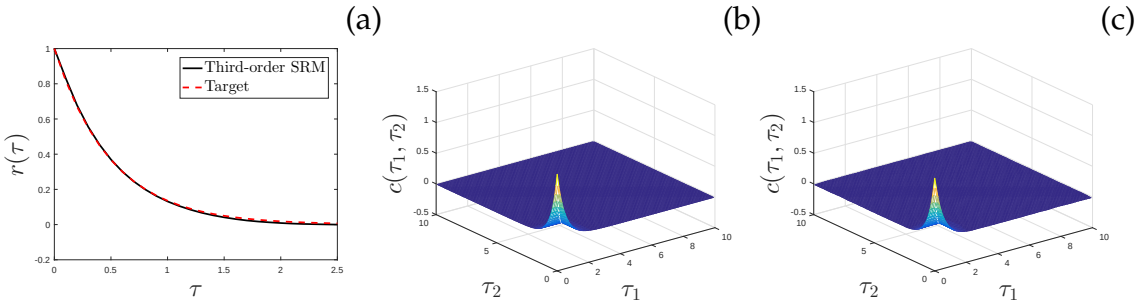

Figure 3.1: (a) Correlation functions, (b) target and (c) estimated third-order cumulant functions of third-order SRM

Set $\alpha = 2$, $k = 1.5$, and $\lambda = 1$. Fig. 3.1 shows the target correlation function and third-order cumulant function of $Q(t)$ and the corresponding estimated

quantities from samples of third-order SRM. Since the third-order SRM $\tilde{Q}_m^{SR}(t)$ converges to $Q(t)$ in the second and the third moment senses, the discrepancies on correlation function and third-order cumulant function are almost indistinguishable. However, because of the incapability of matching the marginal distribution, stochastic processes with different marginal distributions can have the same model from third-order SRM. For example, consider another stochastic differential equation defined in the following equation

$$dQ^*(t) = -\alpha Q^*(t)dt + b^*(Q^*(t))dB(t), \tag{3.49}$$

where

$$\begin{aligned} &b^*(Q^*(t)) \\ &= \frac{1}{\sigma_l}\sqrt{\frac{2\alpha\mu_l(\Phi[(\log(\sigma_l Q^*(t)+\mu_l)-\mu)/\sigma] - \Phi[(\log(\sigma_l Q^*(t)+\mu_l)-\mu)/\sigma - \sigma])}{f_l(\sigma_l Q^*(t)+\mu_l)}}, \end{aligned} \tag{3.50}$$

in which Φ is the distribution of the standard Gaussian variable, μ_l and σ_l are the mean and standard deviation of the log-normal density f_l with parameters μ and σ. We set parameters $\mu = 0$ and $\sigma = 0.3342$ so that the skewness of $Q^*(t)$ is equal to γ_3. Then, processes $Q(t)$ and $Q^*(t)$ have the identical first three moments defined in Eqs. 3.40-3.42. Therefore, the third-order SRM for $Q(t)$ and $Q^*(t)$ remain the same although the marginal distribution of $Q^*(t)$ follows the normalized log-normal distribution, as shown in Fig. 3.2. Note that the distributions in the right panel are plotted in the logarithmic scale so that the discrepancies in the tails of the distributions can be clearly seen. In this example, the third-order SRM may underestimate or overestimate the tail of the distribution. As a result, denote by $Q_{\max} = \max_{t\in[0,\tau^*]} Q(t)$, $Q^*_{\max} = \max_{t\in[0,\tau^*]} Q^*(t)$, and $\tilde{Q}_{\max} = \max_{t\in[0,\tau^*]} \tilde{Q}_m^{SR}(t)$ the maximums of $Q(t)$, $Q^*(t)$, and third-order SRM $\tilde{Q}_m^{SR}(t)$ over the time interval $[0, \tau^*]$, respectively. The distribution of extreme,

i.e., $P(\tilde{Q}_{\max} \leq q)$, based on the third-order SRM exhibits large errors when q is large, as shown in Fig. 3.3.

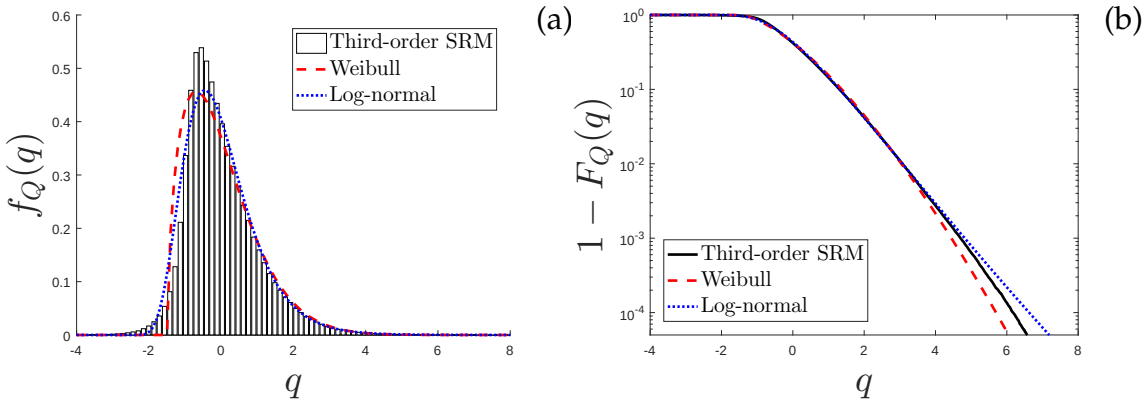

Figure 3.2: (a) Marginal densities and (b) marginal distributions of $Q(t)$, $Q^*(t)$, and third-order SRM $\tilde{Q}_m^{SR}(t)$

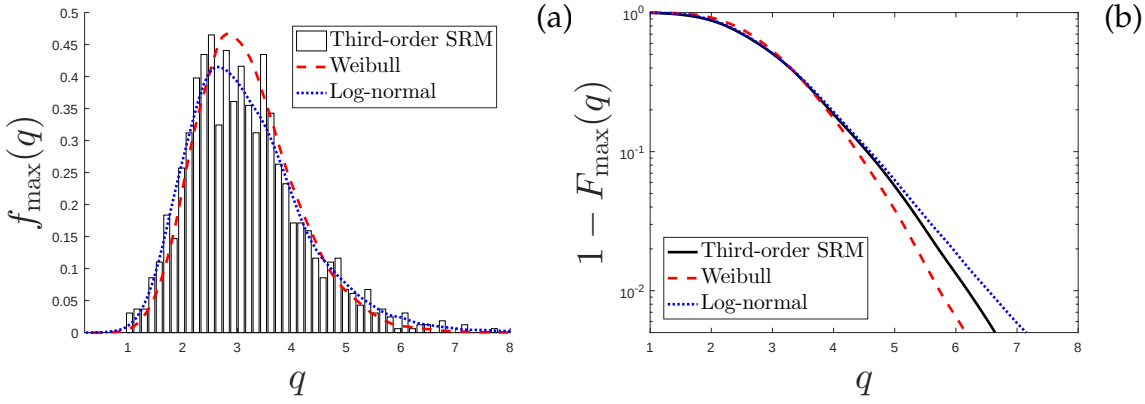

Figure 3.3: (a) Densities and (b) distributions of $Q_{\max}$, $Q^*_{\max}$, and $\tilde{Q}_{\max}$ based on third-order SRM

Figs. 3.4 and 3.5 show the convergences of polynomial chaos $\tilde{Q}_m^{PC}(t)$ to $Q(t)$ in marginal distribution and in correlation function as truncation level m grows. The third-order cumulant functions of $\tilde{Q}_m^{PC}(t)$ at truncation levels $m = 1, 6$, and 10 are shown in Fig. 3.6. It is not surprising that the third-order cumulant function at truncation level $m = 1$ is zero because $\tilde{Q}_1^{PC}(t) = G(t)$ is a Gaussian process. As for this example, the third-order cumulant function is convergent to the target third-order cumulant function. Fig. 3.7 shows the exact maps

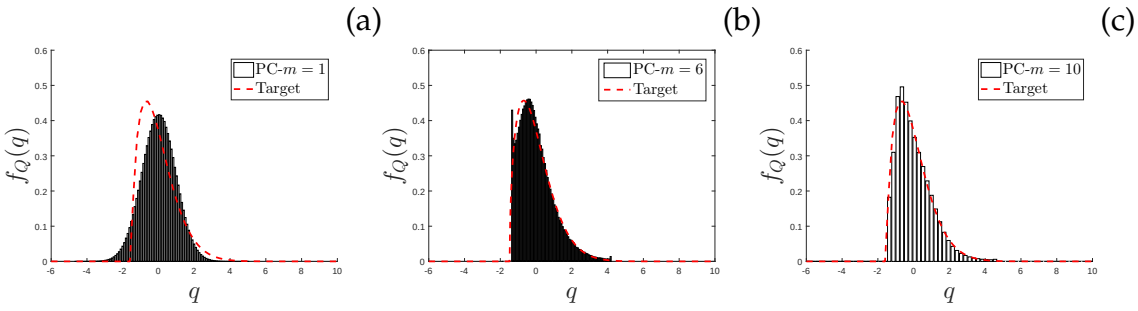

Figure 3.4: Marginal distributions of polynomial chaos at truncation level $m =$ (a) 1, (b) 6, and (c) 10

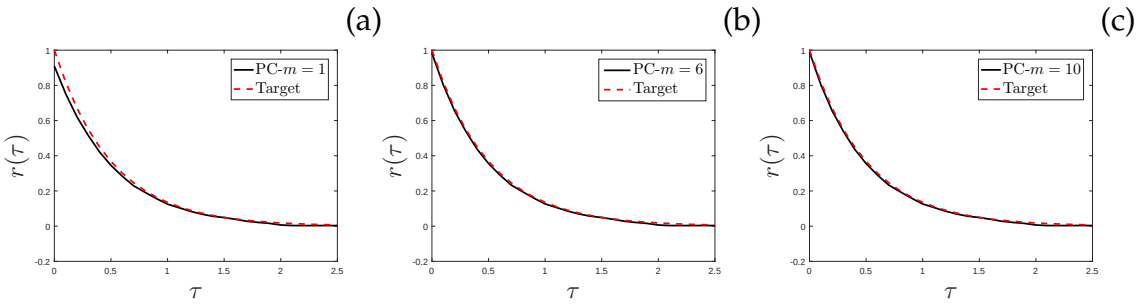

Figure 3.5: Correlation functions of polynomial chaos at truncation level $m =$ (a) 1, (b) 6, and (c) 10

$Q(t) = h(G(t))$ and $Q^*(t) = h^*(G(t))$ at fix time t and the approximate maps $\tilde{Q}_m^{PC}(t) = h_m^{PC}(G(t)) = \sum_{k=0}^{m} \beta_k h_k(G(t))$ from polynomial chaos at truncation levels $m = 1, 6, 10$. The red solid line in the figure indicates the lower bounds. Note that in Fig. 3.7(a), the models $\tilde{Q}_1^{PC}(t)$, $\tilde{Q}_6^{PC}(t)$, and $\tilde{Q}_{10}^{PC}(t)$ have values below the lower bound, although it is not obvious in the middle and right panels of Fig. 3.4.

Fig. 3.8 shows the marginal distributions of $Q(t)$, $Q^*(t)$, and corresponding estimates from polynomial chaos $\tilde{Q}_m^{PC}(t)$ at truncation levels $1, 6, 10$. The tails of the distributions of $\tilde{Q}_m^{PC}(t)$ deviate dramatically because the maps h_6^{PC} and h_{10}^{PC} have notable oscillations in a vicinity of $G(t) = 5$, as shown in Fig. 3.7 (a) and (b). Besides, the convergence rates of the distributions of $\tilde{Q}_m^{PC}(t)$ in the tail region are slow. The distributions of extremes of the target processes $Q(t)$, $Q^*(t)$ and

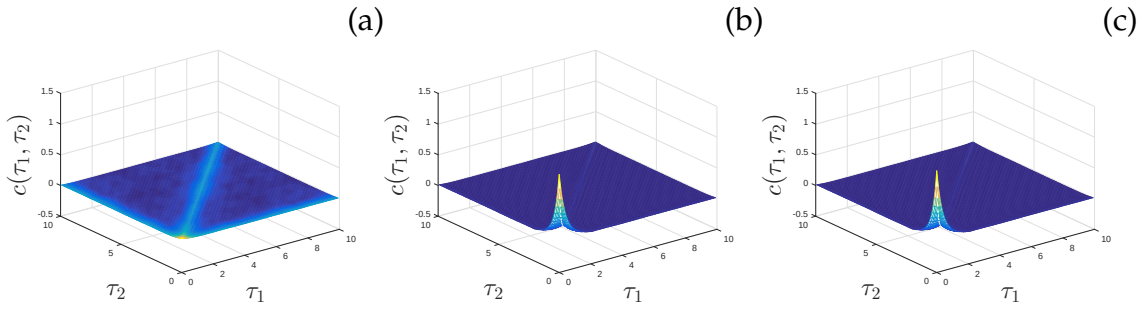

Figure 3.6: Third-order cumulant functions of polynomial chaos at truncation level $m =$ (a) 1, (b) 6, and (c) 10

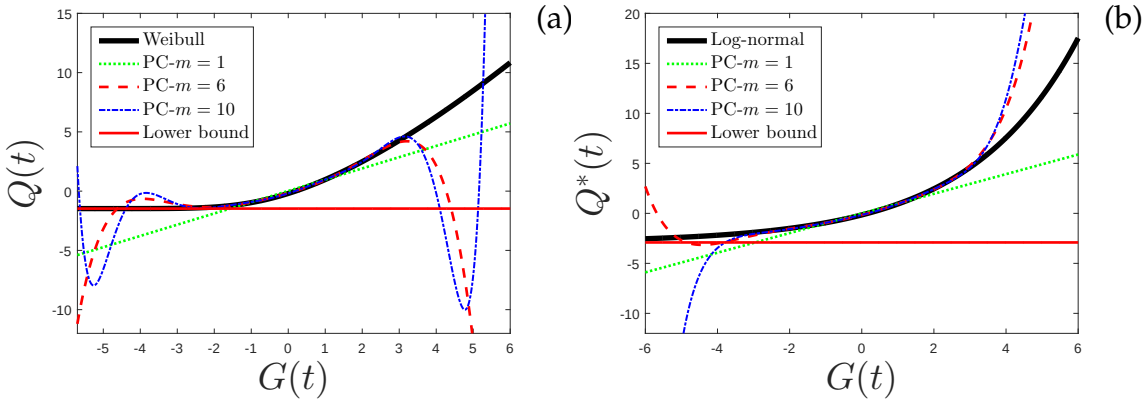

Figure 3.7: Exact maps, (a) $Q(t) = h(G(t))$ and (b) $Q^*(t) = h^*(G(t))$, vs. PC approximate maps, $\tilde{Q}_m^{PC}(t) = h_m^{PC}(G(t))$

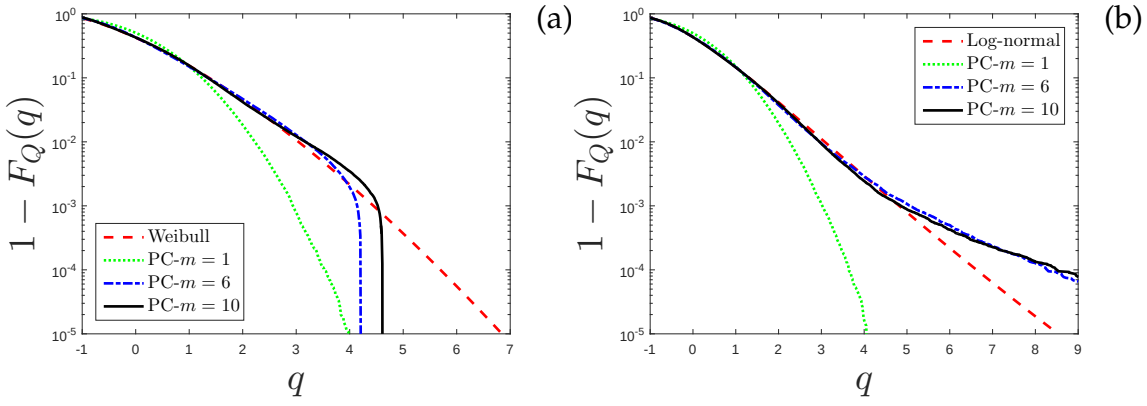

Figure 3.8: Marginal distributions of (a) $Q(t)$, (b) $Q^*(t)$, and polynomial chaos $\tilde{Q}_m^{PC}(t)$ at truncation levels $1, 6, 10$

polynomial chaos $\tilde{Q}_m^{PC}(t)$ are shown in Fig. 3.9. The accuracies of the estimates from polynomial chaos are unsatisfactory and decrease with the argument q.

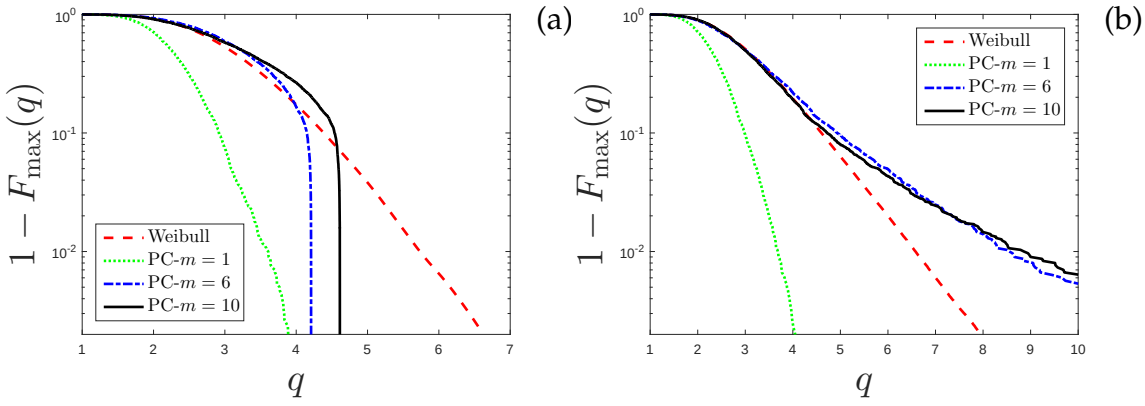

Figure 3.9: Distributions of (a) $Q_{\max}$, (b) $Q^*_{\max}$, and $\tilde{Q}_{\max}$ based on polynomial chaos at truncation levels $1, 6, 10$

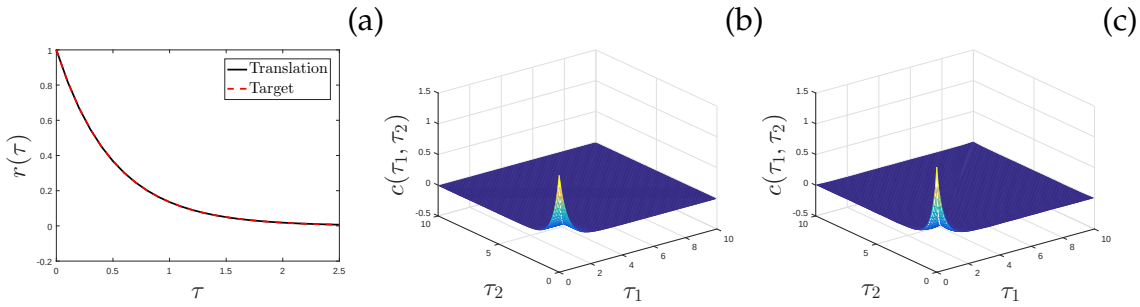

Figure 3.10: (a) Correlation functions, (b) target and (c) estimated third-order cumulant functions of translation model

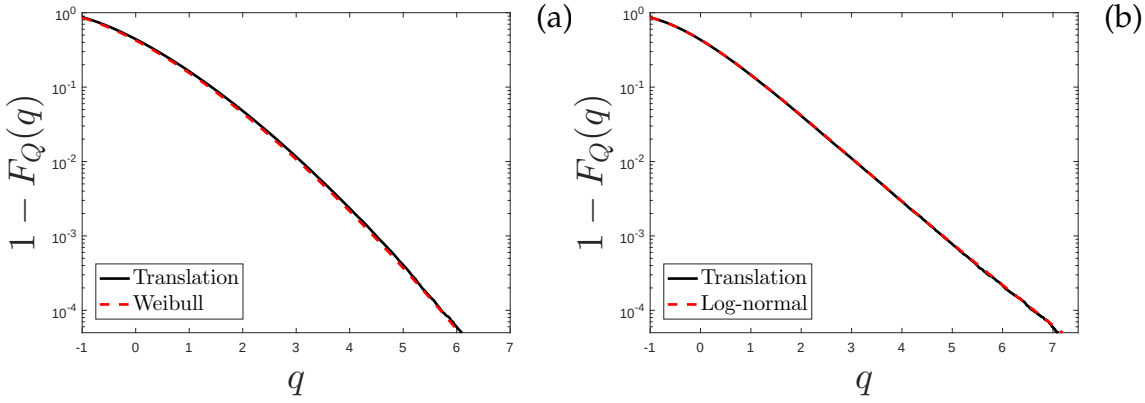

Figure 3.11: Marginal distributions of (a) $Q(t)$, (b) $Q^*(t)$, and translation model $\tilde{Q}_T(t)$

Figs. 3.10 and 3.11 show the target marginal distribution, correlation function, and the third-order cumulant function of $Q(t)$ and the corresponding es-

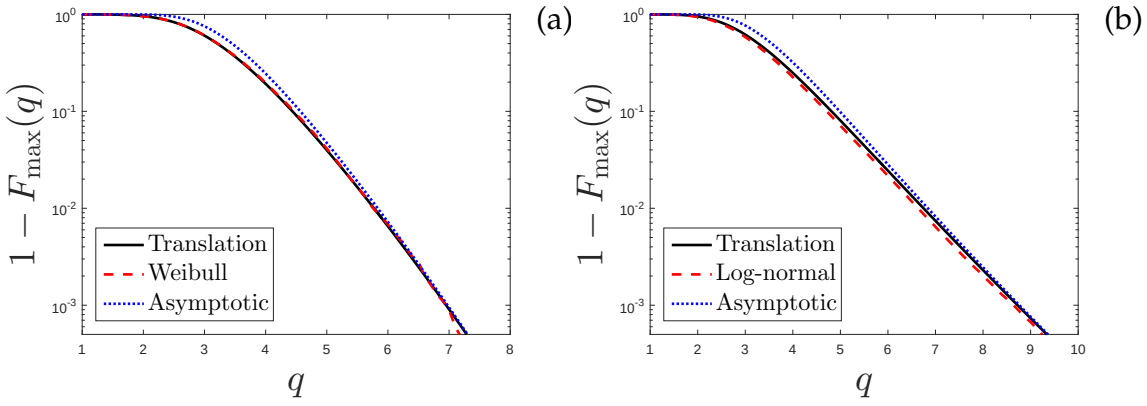

Figure 3.12: Distributions of (a) $Q_{\max}$, (b) $Q^*_{\max}$, and $\tilde{Q}_{\max}$ based on the translation model $\tilde{Q}_T(t)$

timated quantities from samples of translation model. In this example, $\tilde{Q}_T(t)$ can match both marginal distribution and correlation function exactly because (1) $r(\tau)$ is positive for all τ and the admissible bounds $r^L = -0.8623$, $r^U = 1$ so that $r(\tau) \in [r^L, r^U]$, and (2) the resulting $\rho(\tau)$ from Eq. 3.25 is positive semi-definite. The third-order cumulant function of $\tilde{Q}_T(t)$ approximates that of $Q(t)$ satisfactorily.

The plots in Fig. 3.12 are for the distributions of extremes. The red dash lines are the estimates from the target processes $Q(t)$ and $Q^*(t)$, and the black solid lines are the corresponding approximations from the translation model $\tilde{Q}_T(t)$. The blue dotted lines in the figure are the probabilities $1 - F_Q(q)^n$ and $1 - F_{Q^*}(q)^n$, where $F_Q(q)$ and $F_{Q^*}(q)$ are the marginal distributions of $Q(t)$ and $Q^*(t)$, and n is the number of time points which partition the time interval $[0, \tau^*]$ in the numerical calculation. The convergences of the blue dotted lines to the black solid lines as q increases validate the tail independence (second property) of the translation model. The accuracy of the distribution of extreme based on the translation model is remarkable in the left panel, but is slightly worse in the right panel. If we consider another stochastic process $Q^{**}(t)$ defined in the

Eqs. 3.49-3.50 with log-normal marginal distribution and parameters $\mu = 0$ and $\sigma = 1$, the quality of the extreme estimate based on the translation model further deteriorates, as shown in Fig. 3.13(a). This observation results from the fact that the dependences between simultaneously large values of $Q(t)$, $Q^*(t)$, and $Q^{**}(t)$ at different time points are in ascending order. We characterize such dependence by, e.g., the correlation coefficient of $\boldsymbol{Q}|\|\boldsymbol{Q}\| > p$, denoted by ρ_Q, where p is large, t_1, t_2 are two time arguments, $\boldsymbol{Q} = [Q(t_1), Q(t_2)]$, F_Q is the marginal distribution of $Q(t)$, and norm $\|\boldsymbol{Q}\| = \sqrt{F_Q(Q(t_1))^2 + F_Q(Q(t_2))^2}$. Fig. 3.13(b) shows the correlation coefficients ρ_Q, ρ_{Q^*}, and $\rho_{Q^{**}}$. As p approaches $\sqrt{2}$, we have $\rho_{Q^{**}} > \rho_{Q^*} > \rho_Q \approx 0$ which is consistent with the observation and the above statement.

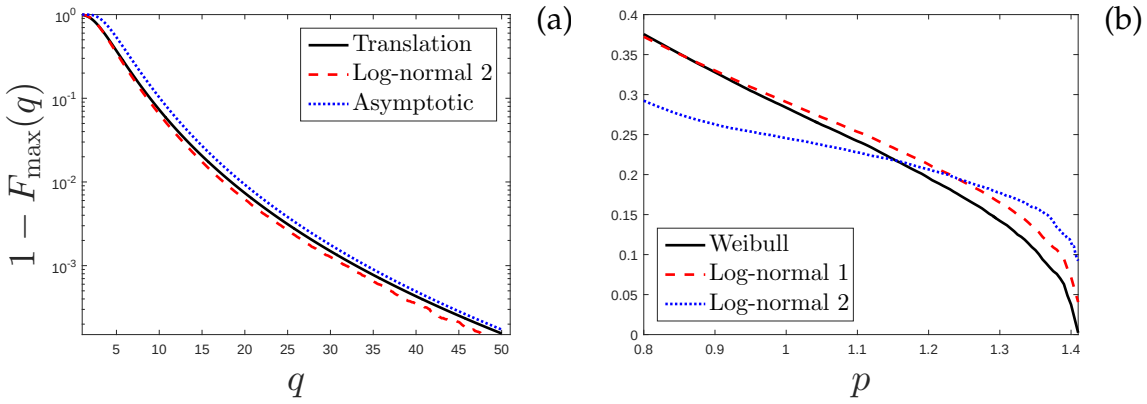

Figure 3.13: (a) Distribution of extremes of $Q^{**}(t)$ and $\tilde{Q}_T(t)$ and (b) correlation coefficients ρ_Q, ρ_{Q^*}, and $\rho_{Q^{**}}$

In summary, the non-Gaussian models, i.e., third-order SRM, polynomial chaos, and translation model, can match exactly or approximate satisfactorily the correlation function and third-order cumulant function of the target processes in this example. However, only translation model captures the marginal distributions. It provides the best approximations on the distributions of extremes, especially when the tail dependence of the target process is weak. It has

also been shown that as the tail dependence grows, the quality of the extreme estimate based on the translation model deteriorates.

3.5.2 Example 2

We now construct a copula-based Markov model $\tilde{Q}_m^M(t)$ with $m = 2$ for target process $Q(t)$ defined in Eq. 3.39. The model $\tilde{Q}_2^M(t)$ has the form

$$\begin{aligned} \tilde{Q}_2^M(t_1) &= F_Q^{-1}(U_1), \quad \text{and} \\ \tilde{Q}_2^M(t_i) &= F_{i|i-1}^{-1}(U_i), \quad i = 2, \ldots, n, \end{aligned} \tag{3.51}$$

where $t_1, \ldots, t_n$ evenly partition the bounded time interval $[0, \tau^*]$, $U_1, \ldots, U_n$ are independent uniform random variables, and $F_{i|i-1}(q_2|q_1)$ is the distribution of the conditional random variable $Q(t_i)|Q(t_{i-1})$. The corresponding joint distributions $F_{i,i-1}(q_1, q_2)$ of $[Q(t_i), Q(t_{i-1})]^T$, $i = 2, \ldots, n$, are approximated by the following 2-copula

$$\begin{aligned} &F_{i,i-1}(q_1, q_2) \approx C(u_1, u_2) \\ =&\theta_3(u_1^{-\theta_1} + u_2^{-\theta_1} - 1)^{-1/\theta_1} + (1 - \theta_3) \exp\big(- [(-\log u_1)^{\theta_2} + (-\log u_2)^{\theta_2}]^{1/\theta_2}\big), \end{aligned} \tag{3.52}$$

where $u_1 = F_Q(q_1)$, $u_2 = F_Q(q_2)$, and $\theta_1 \geq 0$, $\theta_2 \geq 1$, $\theta_3 \in [0, 1]$ are parameters that need to be determined. It is worth noting that from Eq. 3.36, the conditional distributions $F_{i|i-1}(q_2|q_1)$ can be linked with $C(u_1, u_2)$ through the equation

$$F_{i|i-1}(q_2|q_1) = \frac{\partial C(u_1, u_2)}{\partial u_1}. \tag{3.53}$$

The proof of Eq. 3.53 is in [45] (p. 41). The set of parameters $\Theta = [\theta_1, \theta_2, \theta_3]$ are obtained by minimizing the objective function in Eq. 3.37 that is set to be $e(\Theta) = \alpha_1 e_1(\Theta) + \alpha_2 e_2(\Theta) + \alpha_3 e_3(\Theta)$, where $e_1(\Theta)$, $e_2(\Theta)$, and $e_3(\Theta)$ are for correlation

function, third-order cumulant function, and joint distribution at 2 consecutive time points which are defined in Table. 3.2. The plots in Figs. 3.14 and 3.15 show the aforementioned quantities and the corresponding estimates from samples of the model $\tilde{Q}_2^M(t)$. Optimal values of these parameters are selected so that all the quantities of interest can be matched almost perfectly.

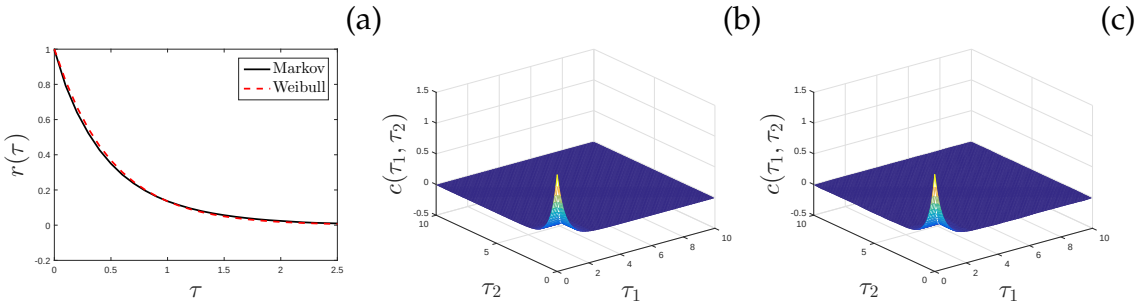

Figure 3.14: (a) Correlation functions, (b) target and (c) estimated third-order cumulant functions of the Copula-based Markov model

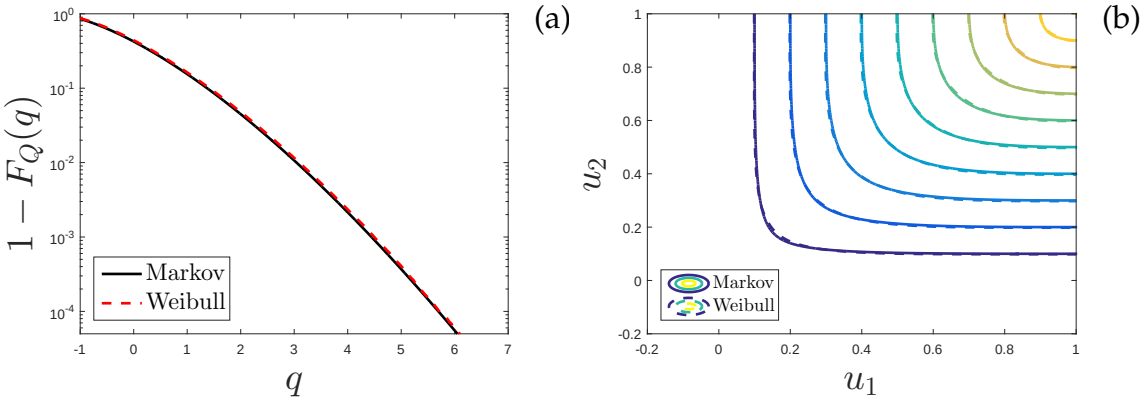

Figure 3.15: (a) Marginal distributions and (b) joint distributions at consecutive times of $Q(t)$ and model $\tilde{Q}_2^M(t)$

We now use the same copula model in Eq. 3.52 and change the quantities of interest to be $e(\Theta) = \alpha_1 e_1(\Theta) + \alpha_3 e_3(\Theta) + \alpha_4 e_4(\Theta) + \alpha_5 e_5(\Theta)$ which are related to correlation function, joint distribution, distribution of extreme and mean crossing rate. The results of $Q(t)$ are also extended to the target processes $Q^*(t)$ and $Q^{**}(t)$ introduced in the previous example. We compare the relative performances of the translation and the copula-based Markov models.

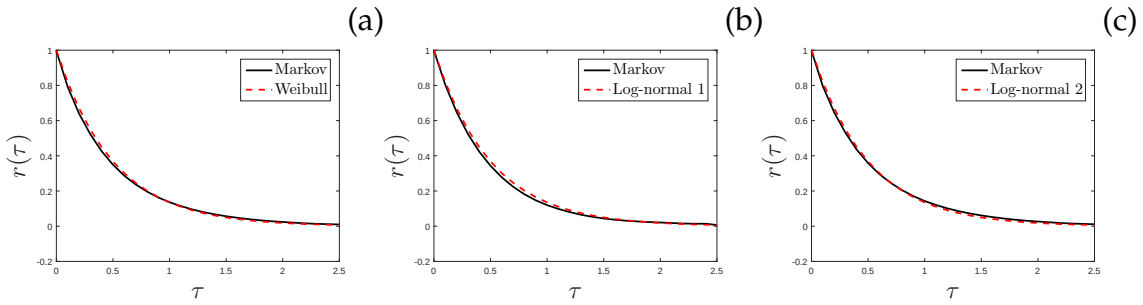

Figure 3.16: Correlation functions of (a) $Q(t)$, (b) $Q^*(t)$, and (c) $Q^{**}(t)$ and corresponding estimates from $\tilde{Q}_2^M(t)$

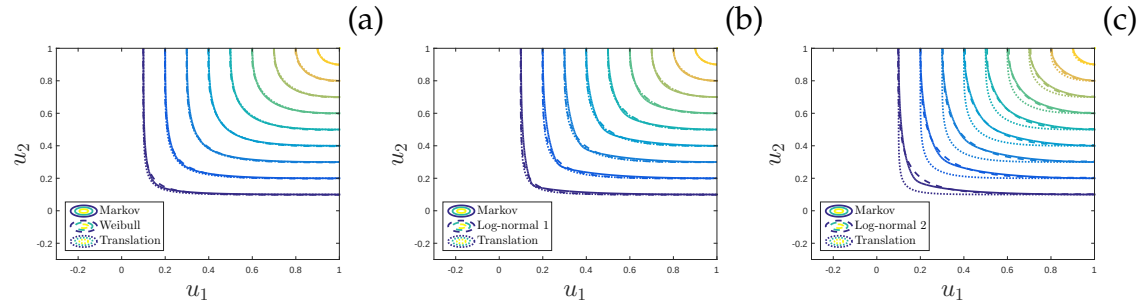

Figure 3.17: Joint distributions of (a) $Q(t)$, (b) $Q^*(t)$, and (c) $Q^{**}(t)$ and corresponding estimates from $\tilde{Q}_2^M(t)$

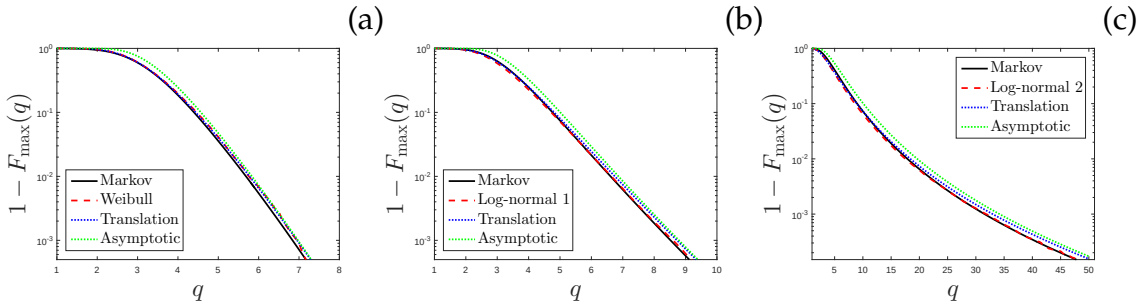

Figure 3.18: Distribution of extremes of (a) $Q(t)$, (b) $Q^*(t)$, and (c) $Q^{**}(t)$ and corresponding estimates from $\tilde{Q}_2^M(t)$

The results are shown in Figs. 3.16-3.19. The solid and dotted contour plots in Fig. 3.17, and the black solid lines and blue dotted lines in Figs. 3.18 and 3.19 correspond to the copula-based Markov and translation models, respectively. As can be seen from Fig. 3.18, the performances of the copula-based Markov model are satisfactory for all test cases, while the quality of the approximation

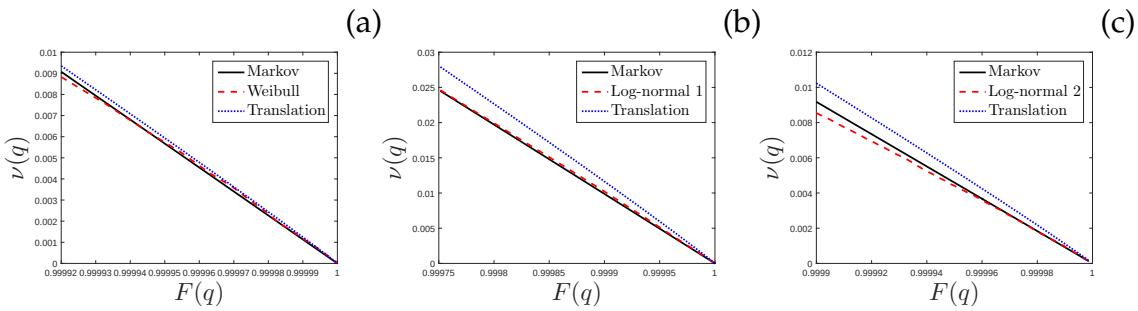

Figure 3.19: Mean crossing rates of (a) $Q(t)$, (b) $Q^*(t)$, and (c) $Q^{**}(t)$ and corresponding estimates from $\tilde{Q}_2^M(t)$

from translation model depends strongly on the tail dependence of the target process. The same observations are in Figs. 3.17 and 3.19, i.e., the dotted lines deviate from the target dash lines as the tail dependence increases, but the solid lines approximate accurately and consistently the dash lines, especially in the tail region. This also suggests the inherent relations among the distribution of extreme, mean crossing rate, and the joint distribution at 2 consecutive time points. It has been shown in [44] that under the Poisson assumption, the distribution of extreme $\tilde{F}_{\max}(q)$ is given in terms of the mean crossing rate $\tilde{\nu}(q)$ by

$$\tilde{F}_{\max}(q) = P(\max_{t\in[0,\tau^*]} \tilde{Q}_m^M(t) \leq q) = \exp(-\tilde{\nu}(q)\tau^*), \tag{3.54}$$

where the mean crossing rate $\tilde{\nu}(q)$ can be estimated by $P(\tilde{Q}_m^M(t_i) \leq q, \tilde{Q}_m^M(t_{i+1}) > q)/\Delta t = (F(q) - C(F(q), F(q)))/\Delta t$, in which Δt is the time step between t_{i+1} and t_i, F is its marginal distribution, and C is the 2-copula defined in Eq. 3.52 which is equivalent to the joint distribution at 2 consecutive time points. Therefore, a good approximation of one quantity may lead to accurate approximations for the other two. The above statement is extremely useful when the accurate estimate is only available for the mean crossing rate (or equivalently the joint distribution) because of the limited data size in the practical applications. We use Eq. 3.54 to infer the distribution of extreme.

3.5.3 Example 3

We calibrate the copula-based Markov model to a wind pressure process obtained from the wind tunnel experiment and compare its performance with the translation model.

The wind tunnel records from Shimizu Corporation Laboratories for zero wind direction are used in this analysis. The mean wind velocity profile corresponds to the urban terrain. The building model is a CAARC standard tall building with square cross section and has 500 wind pressure taps uniformly distributed on its sides. The size of the building model is $0.1\text{m} \times 0.1\text{m} \times 0.5\text{m}$ and the length scale is $1 : 400$. The wind pressure process is from the pressure tap located in the flow separated region where the complex aerodynamic phenomenon occurs. The time history is shown in Fig. 3.20. A total of 32768 measurements of non-dimensional pressure coefficients are recorded continuously with 1000 Hz measurement frequency. Further details can be in [37].

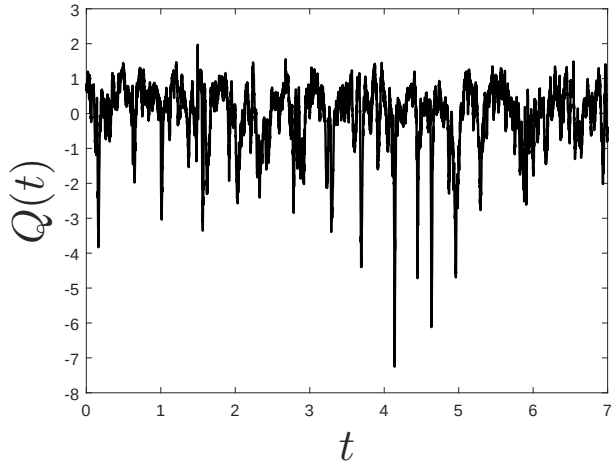

Figure 3.20: Time history of wind pressure process

We estimate the marginal distribution F empirically and the transition den-

sity of the Markov model is approximated by a 3-copula which has the form

$$C(\boldsymbol{u}) = \theta_9 \exp\Big\{ -\Big[\sum_{j=1}^{3} \theta_1 p z_j + \big[(pz_1^{\theta_2})^{\theta_3} + (pz_2^{\theta_2})^{\theta_3}\big]^{\frac{1}{\theta_3}} + \big[(pz_2^{\theta_2})^{\theta_3} + (pz_3^{\theta_2})^{\theta_3}\big]^{\frac{1}{\theta_3}} + \big[(pz_1^{\theta_2})^{\theta_4} + (pz_3^{\theta_2})^{\theta_4}\big]^{\frac{1}{\theta_4}}\Big]^{\frac{1}{\theta_2}} \Big\} + (1-\theta_9)\Big[\sum_{j=1}^{3} u_j^{-\theta_6} - 2 - \big[\hat{u}_1^{-\theta_7} + \hat{u}_2^{-\theta_7}\big]^{-\frac{1}{\theta_7}} + \big[\hat{u}_2^{-\theta_7} + \hat{u}_3^{-\theta_7}\big]^{-\frac{1}{\theta_7}}\big[\hat{u}_1^{-\theta_8} + \hat{u}_3^{-\theta_8}\big]^{-\frac{1}{\theta_8}}\Big]^{-\frac{1}{\theta_6}}, \tag{3.55}$$

where $\boldsymbol{u} = [u_1, u_2, u_3]$, $p = (\theta_1 + 2)^{-1}$, $z_j = -\log u_j$, and $\hat{u}_j = (u_j^{-\theta_2} - 1)/(\theta_5 + 2)$, $j = 1, 2, 3$. The ranges of the parameter $\theta_1, \ldots, \theta_9$ are in Table. B.1 and B.2. As explained in the previous example, the accurate estimate on the distribution of extreme cannot be obtained because of the limited size of the available records. Hence, the objective function in Eq. 3.37 is selected to be $e(\Theta) = \alpha_1 e_1(\Theta) + \alpha_3 e_3(\Theta) + \alpha_5 e_5(\Theta)$ instead, where $e_1(\Theta)$, $e_3(\Theta)$, and $e_5(\Theta)$ correspond to the errors in correlation function, joint distribution at 2 consecutive time points, and mean crossing rate, respectively. Note that since $Q(t)$ is highly negatively-skewed, we focus on the mean downcrossing rate, i.e., the mean rate that $Q(t)$ downcrosses $-q$.

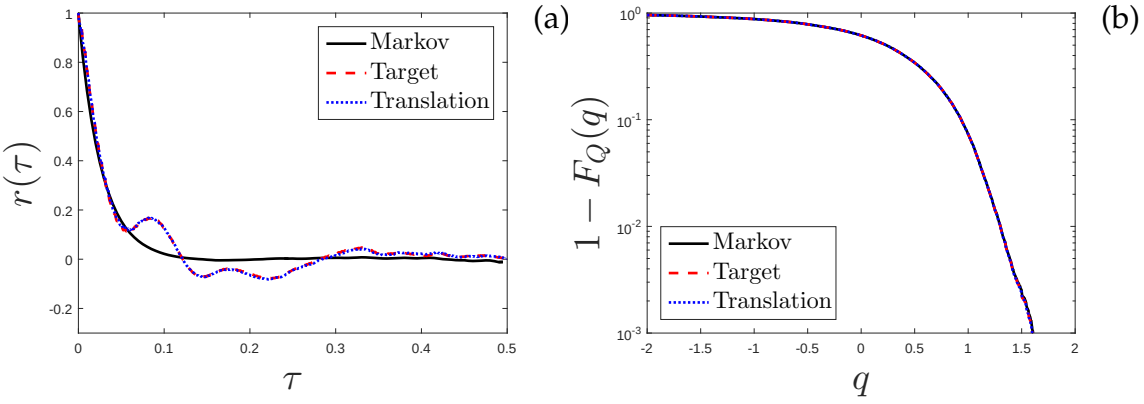

Figure 3.21: (a) Correlation functions and (b) marginal distributions of $Q(t)$, $\tilde{Q}_3^M(t)$ and $\tilde{Q}_T(t)$

The performances of the copula-based Markov model $\tilde{Q}_3^M(t)$ and the trans-

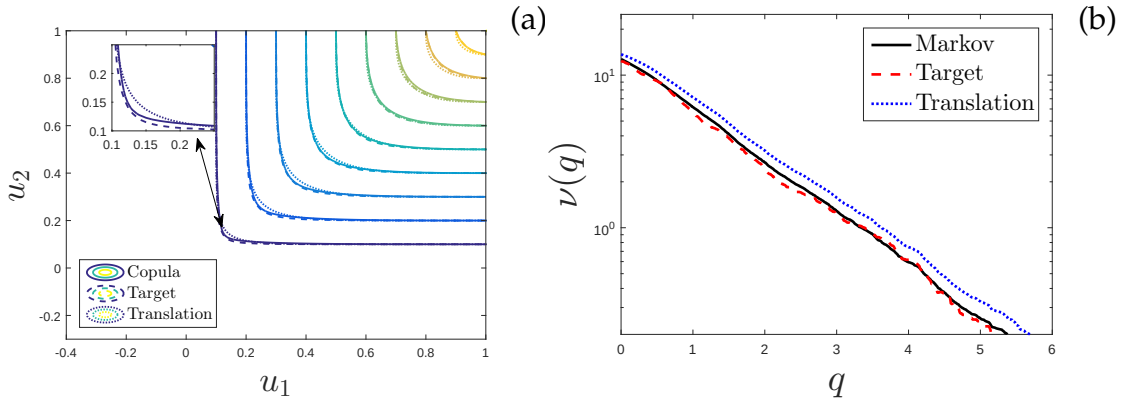

Figure 3.22: (a) Joint distributions and (b) mean crossing rates of $Q(t)$, $\tilde{Q}_3(t)$ and $\tilde{Q}_T(t)$

lation model $\tilde{Q}_T(t)$ are in Figs. 3.21 and 3.22. The copula-based Markov model provides worse approximation on the correlation function comparing to the translation model, but performs almost perfectly for the joint distribution and the mean downcrossing rate, especially in the tail region. The approximation on the correlation function can be improved by increasing the dimension of the copula m. Preliminary study shows that m should be at least greater than 6 in order to capture the wavy shape of this correlation function. It is also worthy noting that the computational cost on constructing the copula-based Markov model depends on the dimension of the copula and it is generally more expensive than the construction of the translation model. It is not our intention here to make a judgment as to which model is preferable. Instead, we outline the strengths and limitations of each model such that the modeler may make the best judgment for the application.

3.6 Chapter summary

The comprehensive review has been presented for three non-Gaussian models, i.e., third-order SRM, polynomials chaos, and translation model. Their accuracies on the estimates of distributions of extremes have been examined by numerical example. It has been shown that the translation model provides the best approximation on the distribution of extreme. Its performance is remarkable when the target process is almost tail independent, yet deteriorates when the tail dependence of the target process increases.

In order to overcome this limitation, a copula-based Markov model has been proposed in this work. The model utilizes the concept of higher-order Markov process whose transition density is characterized by copulas. The optimization algorithm has been developed to estimate the parameters in the copulas such that the errors on the pre-specified quantities of interest are minimized. Theoretical arguments and numerical examples have been provided to illustrate the properties, flexibility, and accuracies of this model on different combinations of quantities of interest. It has been shown that the copula-based Markov model is capable of providing consistent estimation on distribution of extreme, or equivalently the mean crossing rate, regardless of the tail dependence of the target process. The model has also been applied to a wind pressure process from wind tunnel experiment to illustrate its practical use.

CHAPTER 4

TRANSLATION-MODEL-BASED RELIABILITY ANALYSIS FOR WIND LOADS

4.1 Summary

Probabilistic models for wind loads are developed and used to estimate the properties of the responses of linear systems. This analysis involves four steps. First, along-wind, across-wind forces, and torque are represented as polynomials of turbulence fluctuations and wake excitations, which are assumed to be stationary Gaussian processes. Second, two types of models are provided, namely, the empirical model and the mathematical model, for the second-moment properties of the turbulence fluctuations and wake excitations so that the probability law of the wind loads is characterized completely. Proposed models are then calibrated to the experimental observations. Third, the mathematical model provides an efficient method to estimate the response properties relative to Monte Carlo simulation. The responses are modeled by translation processes that match the target second-moment properties and marginal distributions of the responses. Fourth, the response properties that are of interest, e.g., the mean rates at which the responses exit the safe set, are calculated from the resulting translation processes. This procedure is illustrated by one numerical example.

4.2 Introduction to the methodology

Experimental and mathematical approaches are used to characterize structural responses induced by wind loads. Experimental approaches include the full-scale and/or wind-tunnel tests that provide valuable information on both wind loads on structures and structural responses. Cost limits this approach [2]. Mathematical approaches construct deterministic and probabilistic models for wind loads that can be used to estimate the properties of structural responses. This paper proposes probabilistic models to represent wind loads, calibrate these models to the experimental observations, and assess the structural reliability for wind-load effects subjected to these models.

The probabilistic models for wind loads are based on the wind-load model proposed in [52]. Three components of the wind loads, i.e., along-wind, across-wind forces, and torque, are defined by polynomials of the fluctuating part of the wind velocities. Because of the vortex wake formed at the rear region of the structure, additional forces are applied to capture the effects of the wake excitations. Then, the wind loads are fully described by the turbulence fluctuation and wake excitation terms.

Under the assumption that turbulence fluctuations and wake excitations are stationary Gaussian processes, two types of the models for their second-moment properties are considered. The first model is the empirical model that has been used extensively in turbulence and wake excitation modeling. The functional forms of this model result from large amounts of experimental observations and satisfy the physics of the turbulence [53]. The second model represents the turbulence fluctuation and wake excitation terms by filtered Gaussian

processes whose second-moment properties are similar to the empirical model, referred to as the mathematical model [26]. This model is used to develop an efficient method for calculating the response properties of linear structures. The method is based on translation processes that match the target marginal distributions as well as the second-moment properties of the responses. The first two moments of the responses are obtained by methods of the linear random vibration theory [26, 21] and marginal distributions are fitted to the marginal moments calculated exactly by Its formula following an approach in [25]. Then, the structural reliability can be estimated from the resulting translation processes. The mean rate at which the structural responses exit the safe set, referred to as the mean outcrossing rate or mean failure rate, is used to characterize the structural reliability.

The outline of the remaining sections is as follows. Section 4.3 presents the probabilistic models for wind loads including the existing wind-load model and two models for turbulence fluctuations and wake excitations. Section 4.4 describes the experimental records and the algorithm of model calibration. The construction of the translation processes for responses and the use of the method to approximate the mean outcrossing rate are in Section 4.5.

4.3 Probabilistic models for wind loads

The existing wind-load model is summarized first, then this model is used to characterize the second-moment properties of the wind loads and two types of models for turbulence fluctuations and wake excitations are presented.

4.3.1 Wind loads on slender rigid building

Consider a slender rigid building immersed in an ideal bidimensional wind field with wind velocity $V(t) = [\mathrm{u(x,t)}, \mathrm{v(x,t)}]^T$ where $x = (x_1, x_2, x_3)$ is the spatial coordinates shown in Fig. 4.1(a), and $u(x,t)$ and $v(x,t)$ are the wind velocities along with and perpendicular to the mean wind direction (measured by the angle between x_1 and $x_{0,1}$ as shown in Fig. 4.1(b)), referred to as along-wind and across-wind velocities, respectively. Under the assumption that the wind field is stationary, the along-wind and across-wind velocities $u(x,t)$ and $v(x,t)$ admit the representations [53]

$$u(x,t) = \overline{U} + \tilde{u}(x,t), \text{ and } v(x,t) = \tilde{v}(x,t), \tag{4.1}$$

where $\overline{U}(x)$ = mean wind velocity; and $\widetilde{u}(x,t)$ and $\tilde{v}(x,t)$ = along-wind and across-wind turbulence fluctuations. The building is idealized as a linear system with lumped masses at the floor levels. Each lumped mass has three degrees of freedom: along-wind, across-wind displacements, and rotation. Let $F(t)$ be the total force at one floor, and $F_x(t)$, $F_y(t)$ and $M_z(t)$ be the along-wind, across-wind forces, and torque corresponding to the degrees-of-freedom, as shown in Figs. 1(a,b).

The wind-load model proposed in [52] is adopted to represent these forces. The construction of this model involves three steps. First, denote by $F_d(t)$ and $F_l(t)$ the projections of $F(t)$ on the coordinate system aligned with the instantaneous direction of the wind velocity $\gamma(t) = \beta + \delta(t)$ (measured by the angle between x_1' and $x_{0,1}$, where $\delta(t) = \arcsin[\tilde{v}(t)/V(t)]$), in which H_3 is the height of the floor, $\overline{U} = \overline{U}[(0,0,H_3)]$, $\tilde{u}(t) = \tilde{u}[(0,0,H),t]$, $\tilde{v}(t) = \tilde{v}[(0,0,H),t]$, and $V(t) = \sqrt{\overline{U} + \tilde{u}(t)^2 + \tilde{v}^2(t)}$. As shown in Fig. 4.1(b), $F_x(t)$ and $F_y(t)$ relate $F_d(t)$

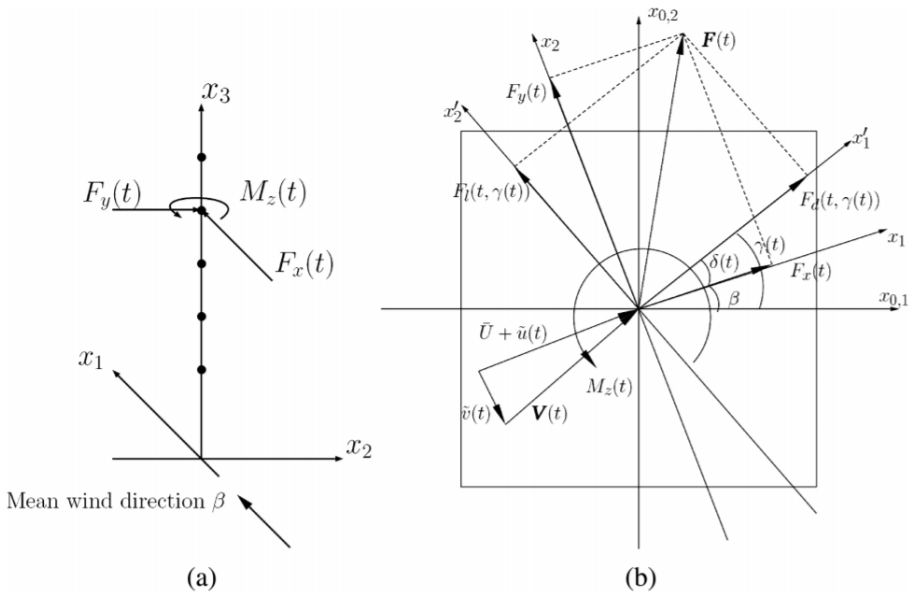

Figure 4.1: (a) Side and (b) top views of the building

and $F_l(t)$ through

$$F_x(t) = F_d(t)\cos\delta(t) - F_1(t)\sin\delta(t), \tag{4.2}$$

$$F_y(t) = F_d(t)\sin\delta(t) - F_1(t)\cos\delta(t), \tag{4.3}$$

Second, set

$$F_d(t) = \rho V^2(t) C_d[\gamma(t)]B/2, \text{ and } F_l(t) = \rho V^2(t) C_l[\gamma(t)]B/2, \tag{4.4}$$

where ρ = air density; B = reference width of the building; and $C_d[\gamma(t)]$ and $C_l[\gamma(t)]$= nondimensional force coefficients corresponding to $F_d(t)$ and $F_l(t)$,respectively [52]. The Taylor expansion of $C_d[\gamma(t)]$ and $C_l[\gamma(t)]$ at β gives

$$\begin{aligned} C_d[\gamma(t)] &= C_d + C_d'\delta(t) + O[\delta^2(t)] \\ C_l[\gamma(t)] &= C_l + C_d'\delta(t) + O[\delta^2(t)], \end{aligned} \tag{4.5}$$

where $C_k = C_k(\beta)$, and $C_k' = \theta C_k[\gamma(t)/\theta\gamma(t)]_{\gamma(t)=\beta}$, $k = d, l$. Eqs. 4.4 and 4.5 are substituted into Eqs. 4.2 and 4.3. Under the assumption of small $\delta(t)$, Eqs. 4.2

and 4.3 become

$$F_x(t) = \frac{1}{2}\rho\overline{U}^2 B^2 C_m + \rho\overline{U}\tilde{u}(t)C_d + \frac{1}{2}\rho\tilde{u}^2(t)BC_d + \frac{1}{2}\rho\overline{U}\tilde{(v)}(t)B(C_d' - C_1), \quad (4.6)$$

$$F_l(t) = \frac{1}{2}\rho\overline{U}^2 BC_l + \rho\overline{U}\tilde{u}(t)BC_l + \frac{1}{2}\rho\overline{U}\tilde{v}(t)B(C_d + C_l'), \quad (4.7)$$

Analogously, torque $M_z(t)$ has the form

$$M_z(t) = \frac{1}{2}\rho\overline{U}^2 B^2 C_m + \rho\overline{U}\tilde{u}(t)B^2 C_m + \frac{1}{2}\rho\overline{U}\tilde{v}(t)B^2 C_m', \quad (4.8)$$

with the notations $C_m = C_m(\beta)$ and $C_m' = \theta C_m[\gamma(t)]/\theta\gamma(t)|_{\gamma(t)=\beta}$. Third, due to the presence of vortex shedding in the rear region of the building, additional forces associated with wake excitations are added linearly to Eqs. 4.6-4.8. Then the non-dimensional forms of Eqs. 4.6-4.8 are

$$C_x(t) = \frac{F_x(t)}{\frac{1}{2}\rho\overline{U}^2 B} = C_d + 2\frac{\tilde{u}(t)}{\overline{U}}C_d + \frac{\tilde{u}^2(t)}{\overline{U}^2}C_d + \frac{\tilde{v}(t)}{\overline{U}}(C_d - C_l') + W_x(t), \quad (4.9)$$

$$C_y(t) = \frac{F_y(t)}{\frac{1}{2}\rho\overline{U}^2 B} = C_l + 2\frac{\tilde{u}(t)}{\overline{U}}C_l + \frac{\tilde{v}(t)}{\overline{U}}C_d + \frac{\tilde{v}(t)}{\overline{U}}(C_d + C_l') + W_y(t), \quad (4.10)$$

$$C_z(t) = \frac{M_Z(t)}{\frac{1}{2}\rho\overline{U}^2 B} = C_m + 2\frac{\tilde{u}(t)}{\overline{U}}C_m + \frac{\tilde{v}(t)}{\overline{U}}C_m' + W_z(t), \quad (4.11)$$

where $C_x(t), C_y(t)$, and $C_z(t)$ = non-dimensional along-wind, across-wind, and torsional force coefficients; and $W_x(t)$, $W_y(t)$ and $W_z(t)$ = zero-mean along-wind, across-wind, and torsional force coefficients associated with wake excitations, respectively.

Turbulence fluctuations $\tilde{u}(t)$ and $\tilde{v}(t)$ can be modeled by Gaussian processes [26]. Assume that $W_k(t)$, $k = x, y, z$, are independent Gaussian processes, then $C_y(t)$ and $C_z(t)$ are Gaussian processes while $C_x(t)$ is a non-Gaussian process, which is consistent with the experimental observations.

Eqs. 4.9-4.11 can be simplified for zero-mean wind direction, $i.e., \beta = 0$. In this special case, turbulence fluctuations $\tilde{u}(t)$ and $\tilde{v}(t)$ are regarded to be independent because of the symmetry of the flow field that indicates $E[\tilde{u}(t)\tilde{v}(t)] = 0$

and experimental observations (Appendix C). Moreover, $C'_d = C_l = C_m = 0$ and $W_x(t)$ contribute insignificantly to $C_x(t)$ [54]. Accordingly, Eqs. 4.9-4.11 yield

$$C_x(t) = C_d + 2\frac{\tilde{u}(t)}{\overline{U}}C_d + \frac{\tilde{u}^2(t)}{\overline{U}^2}C_d, \tag{4.12}$$

$$C_y(t) = \frac{\tilde{v}(t)}{\overline{U}}(C_d + C'_l) + W_y(t), \tag{4.13}$$

$$C_y(t) = \frac{\tilde{v}(t)}{\overline{U}}C'_m + W_z(t), \tag{4.14}$$

In this special case, along-wind force coefficient $C_x(t)$ is independent of $C_y(t)$ and $C_z(t)$.

4.3.2 Second-moment characterization

Let $C(t) = [C_x(t), C_y(t), C_z(t)]^T$ be the non-dimensional wind-load vector process. The second-moment properties of $C(t)$ are shown for the zero-mean wind-direction case. First, the mean of $C(t)$, $E[C(t)]$, is $[C_d\{1 + E[\widetilde{u}^2(t)]/\overline{U}^2\}, 0, 0]^T$. Second, denote by $\Gamma_{kq}(T) = E[C_k(t+\gamma)C_q(t)] - E[C_k(t+\gamma)C_q(t)]$, $k, q = x, y, z$ the covariance functions between two arbitrary components of $C(t)$, where γ denotes the time lag. The spectral densities of wind loads are $S_{kq}(v) = \mathcal{F}[\Gamma_{kq}(\gamma)]$, where v is the circular frequency and $\mathcal{F}$ is the Fourier transform operator. These spectral densities have the expressions

$$S_{xx}(v) = \frac{4C_d^2 S_{\tilde{u}}(v)}{\overline{U}^2} + \frac{C_d^2 S_{\tilde{u}^2}(v)}{\overline{U}^4}, \tag{4.15}$$

$$S_{yy}(v) = \frac{(C_d + C'_l)S_{\overline{v}}(v)}{\overline{U}^2} + Sw_y(v), \tag{4.16}$$

$$S_{zz}(v) = \frac{C'_m S_{\overline{v}}(v)}{\overline{U}^2} + Sw_z(v), \tag{4.17}$$

$$S_{xy}(v) = S_{xz}(v)) = 0, \tag{4.18}$$

$$S_{yz}(v) = \frac{(C_d + C_l')C_m' S_{\overline{v}}(v)}{\overline{U}^2}, \tag{4.19}$$

with the notations $S_{\overline{\eta}}(v) = \mathcal{F}\{E[\overline{\eta}(t+\gamma)\overline{\eta}(t)]\}$, $\eta = u, v, S_{\tilde{u}^2}(v) = \mathcal{F}E[\tilde{u}^2(t+\gamma)\tilde{u}^2(t)]$ and $S_{w_\xi}(v) = \mathcal{F}EW_\xi(t+\gamma)W_\xi(t)$, $\xi = y, z$. Eqs. 4.15-4.19 relate the wind-load spectral densities with the spectral densities if turbulence fluctuations and wake excitations and wake excitations for which models are provided in the following section.

4.3.3 Turbulence and wake excitation modeling

Two models for $S_{\overline{\eta}}(v)$, $\eta = u, v$ and $S_{W_\xi}(v)$, $\xi = y, z$ are discussed. Model 1 is referred to as the empirical model that follows from an extensive series of experiment observations and some information regarding the physics of the turbulence. Model 2 represents the turbulence fluctuation and wake excitation terms by filtered Gaussian processes of which the functional forms are selected such that the resulting spectral densities match the empirical model as closely as possible.

Model 1: Empirical model

The generalized empirical model for $S_{\overline{\eta}}(v)$, denoted by $S_{\overline{\eta}}^{(1)}(v)$, has the expression [53]

$$\frac{vS_{\overline{\eta}}^{(1)}(v)}{U_*^2} = \frac{nS_{\overline{\eta}}^{(1)}(n)}{U_*^2} = \frac{A_\eta f^{a_\eta}}{(C_\eta + B_\eta f^{b_\eta})^{D_\eta}}, \tag{4.20}$$

where n = frequency measured in hertz; U_* = friction velocity; $f = nH_3/\overline{U}$ are the Monin coordinates; and $A_\eta, B_\eta, C_\eta, D_\eta, a_\eta$ and b_η = parameters to be determined. Denote by $f_{m,\eta}$ the f value in correspondence of the peak value of

$nS_{\tilde{\eta}}^{(1)}(n)$. Because the spectral densities in the inertial subrange are governed by the Kolmogorov hypotheses, i.e., $nS_{\tilde{\eta}}^{(1)}(n)/U_*^2 \propto f^{-2/3}$, Eq.4.20 can be simplified to

$$\frac{vS_{\overline{\eta}}^{(1)}(v)}{\sigma_\eta^2} = \frac{nS_{\overline{\eta}}^{(1)}(n)}{\sigma_\eta^2} = \frac{C_\eta f/f_{m\eta}^{\gamma_\eta}}{[1+1.5\gamma_\eta(f/f_{m\eta})^{\beta_\eta}]^{(2/3+\gamma_\eta)/\beta_\eta}}, \tag{4.21}$$

where σ = standard deviation of the turbulence; β_η and γ_η = parameters defining the peakedness of the spectral densities; and $c_\eta = 1/\int_0^\infty [f/f_{m\eta}^{\gamma_\eta}]/[v + 1.5v\gamma_\eta(f/f_{m\eta})^{\beta_\eta}]^{(2/3+\gamma_\eta)/\beta_\eta}dv$ guarantees that $\int_0^\infty S_{\tilde{\eta}}^{(1)}(v)dv = \sigma_\eta^2$.

The spectral density $S_{W_\xi}^{(1)}(v)$ based on the empirical model takes the form

$$S_{W_\xi}^{(1)}(v) = \sigma_{W_\xi}^2 g_{W_\xi}, \tag{4.22}$$

where σ_{W_ξ} = standard deviation of the force coefficients due to wake excitations; and g_{W_σ} is assumed to have the form [55]

$$g_{w_\xi} = \frac{1}{\sqrt{\pi}d_\xi v_{w_\xi}} \exp\left[-\left(\frac{1-\frac{v}{v_{w_\xi}}}{d_\xi}\right)^2\right], \tag{4.23}$$

where d_ξ = bandwidth parameter; and v_{W_σ} denotes the vortex shedding frequency.

Eqs. 4.21 and 4.22 generally provide satisfactory agreements with experimental observations. However, the he empirical model has one limitation. Few methods can be utilized to estimate the properties of the responses. Classical Monte Carlo simulation is one of the candidate methods that infers the statistics of the responses from response samples that are obtained by solving deterministic versions of equation of motion corresponding to samples of $\tilde{u}(t), \tilde{v}(t), W_y(t)$, and $W_z(t)$. The required sample size is large if, e.g., mean outcrossing rate is examined, so the computational time can be significant.

Wind load	Mean	Variance	Skewness	Kurtosis
$C_x(t)$	1.1250	0.0920	0.6305	3.7304
$C_y(t)$	-0.0322	0.2148	-0.0262	3.0330
$C_z(t)$	-0.0083	0.0051	-0.0272	3.5969

Table 4.1: Statistics of Nondimensional Wind Loads

Model 2: Mathematical model

The turbulence fluctuation and wake excitation terms are modeled by filtered Gaussian processes that have similar spectral densities as the empirical model. Turbulence fluctuations $\tilde{u}(t)$ and $\tilde{v}(t)$ can be described by the Ornstein-Uhlenbeck processes [26]

$$d\tilde{\eta}(t) = -\alpha_\eta \tilde{\eta}(t)dt + \sigma_\eta^2\sqrt{2\alpha_\eta}dB_\eta(t), \tag{4.24}$$

and $W_y(t)$ and $W_z(t)$ are modeled by the responses of linear systems driven by Gaussian noise, i.e.

$$dW_\xi(t) = D_\xi W_\xi(t)dt + g_\xi dB_\xi(t), \tag{4.25}$$

where $W_\xi(t) = [W_\xi(t), W_\xi(t)]^T$; $g_\xi = [0, \beta_\xi]^T$; D_ξ = matrix with components $D_\xi(1,1)$ = 0, $D_\xi(1,2) = 1, D_\xi(2,1) = -\theta_\xi^2$, and $D_\xi(2,2) = -2\gamma - \xi\theta_\xi$; and $B_\eta(t), B_\xi(t)$ = independent standard Brownian motions. The spectral densities corresponding to the models in Eqs. 4.24 and 4.25 are

$$S_{\tilde{\eta}}^{(2)}(v) = \mathcal{F}\{E[\tilde{\eta}(t)\tilde{\eta}(t+\gamma)]\} = \frac{2\alpha_\eta\sigma_\eta^2}{[\pi(v^2+\alpha_\eta^2)]}, \tag{4.26}$$

$$S_{\tilde{u}^2}^{(2)}(v) = \mathcal{F}\{E[\tilde{u}^2(t)\tilde{u}^2(t+\gamma)]\} = \frac{8\alpha_u\sigma_u^4}{[\pi(v^2+4\alpha_u^2)]}, \tag{4.27}$$

$$S_{W_\xi}^{(2)}(v) = \mathcal{F}\{E[W_\xi(t)W_\xi(t+\gamma)]\} = \frac{\beta_\xi^2}{[(v^2-\theta_\xi^2)^2+4\gamma_\xi^2 v^2\theta_\xi^2]}, \tag{4.28}$$

where the parameters $\alpha_\eta, \sigma_\eta, \theta_\xi, \gamma_\xi$, and β_ξ are selected by minimizing the norms $\left\|S_{\tilde{\eta}}^{(2)}(v) - S_{\tilde{\eta}}^{(1)}(v)\right\|$ and $\left\|S_{W_\xi}^{(2)}(v) - S_{W_\xi}^{(1)}(v)\right\|$. Unlike the unfavorable feature of

Model 1, Model 2 provides an alternative method to estimate the response properties. This method is more efficient than Monte Carlo simulation.

The structural responses are approximated by translation processes that require knowledge of the marginal distributions as well as the second-moment properties of the marginal distributions an well as the second-moment properties of the responses. The second-moment properties, i.e., the mean and correlation functions of responses, are calculated from those of the wind loads. Marginal distributions are fitted to the marginal moments that can be obtained from moment equations derived from Itô's formula. The resulting translation processes can then be utilized to assess the structural performances.

4.4 Experimental data and model calibration

The experimental records used in this analysis are described, several assumptions are validated, and the algorithm for model calibration is illustrated by one example.

4.4.1 Experimental data

The wind tunnel records from Shimizu Corporation Laboratories for zero wind direction are used in this analysis. The mean wind velocity profile corresponds to the urban terrain. The model is a 25-story building with square cross section and has 500 wind pres-sure taps uniformly distributed on its sides. The length scale used for the model is 1:400. A total of 32,768 measurements of nondimensional pressure coefficients are recorded continuously with 1,000-Hz

measurement frequency. Further details can be found in [37].

Under the assumption that the pressure field is stationary and ergodic, statistics of non-dimensional wind loads $C_x(t), C_y(t)$, and s can be estimated by averaging the time records. Table 1 shows the first four marginal moments of the wind loads at the 12th floor. The mean and standard deviation of $C_k(t)$ are denoted by μ_k and σ_k, and $\tilde{C}_k(t) = [C_k(t) - \mu_k]/\sigma_k$ is set as the normalized wind load. Fig. 4.2(a) shows the marginal densities of $C_k(t)$ and standard normal distribution. $\tilde{C}_x(t)$ presents more non-Gaussian features than $\tilde{C}_y(t)$ and $\tilde{C}_z(t)$. This observation supports the formulation of the wind-load model. Fig. 4.2(b) shows the correlation functions $E[\tilde{C}_x(t+\gamma)\tilde{C}_y(t)], E[\tilde{C}_x(t+\gamma)\tilde{C}_z(t)]$, and $E[\tilde{C}_y(t+\gamma)\tilde{C}_z(t)]$, which can be viewed as the corresponding correlation-coefficient functions between $[C_x(t), C_y(t)], [C_x(t), C_z(t)]$, and $[C - y(t), C_z(t)]$. $C_x(t)$ is almost uncorrelated with $C_y(t)$ and $C_z(t)$, i.e., $E[C_x(t+\gamma)C_y(t)] = E[C_x(t+\gamma)C_z(t)] = 0$. From Eqs. 4.12-4.14, $E[C_x(t+\gamma)C_y(t)]$ and $E[C_x(t+\gamma)C_z(t)]$ are proportional to $E[\tilde{u}(t+\gamma)\tilde{v}(t)]$. This implies the independence between $\tilde{u}(t)$ and $\tilde{v}(t)$ because it is assumed that $\tilde{u}(t)$ and $\tilde{v}(t)$ are Gaussian.

4.4.2 Model calibrations

The parameters of both models defined are fitted to the experimental observations. Let $S_{kk}(\nu;\Theta), k = x, y, z$, be the functional forms of spectral densities with a vector Θ of parameters, e.g., $\Theta = [\alpha_u, \sigma_u]$ for the spectral density of the along-wind force based on Model 2. The algorithm for model calibration has two steps. First, spectral densities of the wind loads are estimated from experimental records. Denote by $S_{kk}(\nu), k = x, y, z$ the corresponding estimates of the

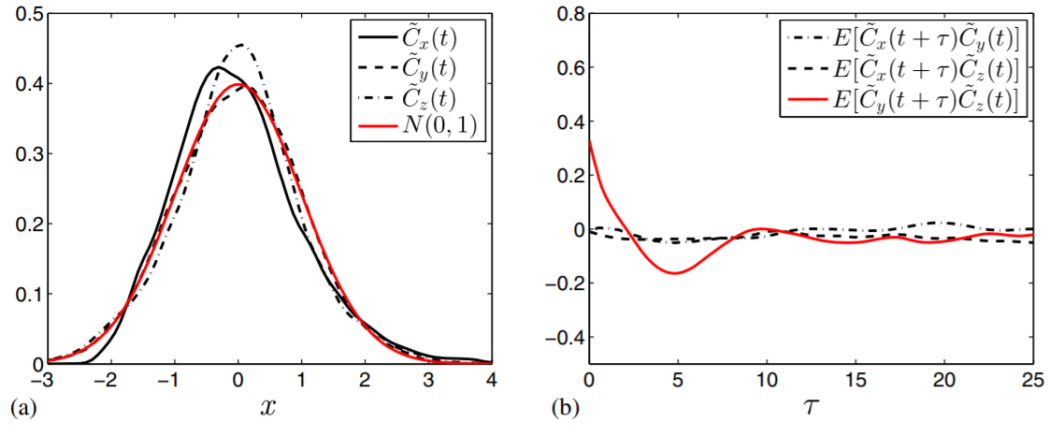

Figure 4.2: Statistics of $\tilde{C}_x(t), \tilde{C}_y(t)$, and $\tilde{C}_z(t)$: (a) marginal densities; (b) correlation functions

,

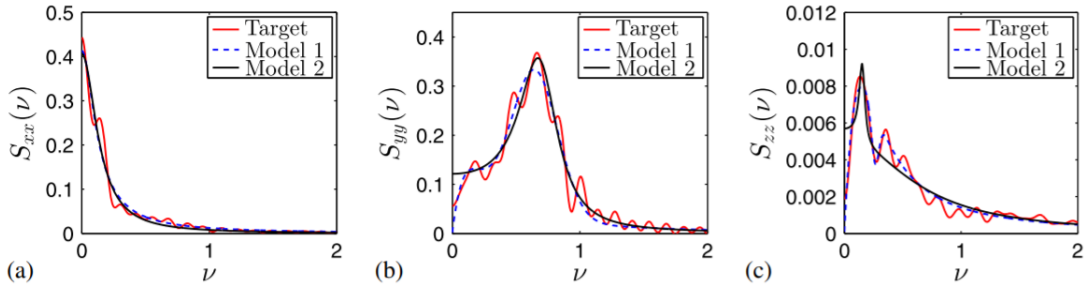

Figure 4.3: Example of model calibration for (a) along-wind force $C_x(t)$; (b) across-wind force $C_y(t)$; (c)torque $C_z(t)$

,

spectral densities. Second, parameters Θ are selected by minimizing the error $\int \left[S_{kk}(\nu;\theta) - \hat{S}_{kk}(\nu)\right]^2 dv$.

Fig. 4.3 shows one example for model calibration. The lighter solid lines are the estimates $\hat{S}_{kk}(\nu)$ obtained from experimental records. The dashed and darker solid lines are the spectral densities $S_{kk}(\nu, \Theta)$ based on Models 1 and 2 fitted to $\hat{S}_{kk}(\nu)$ by the preceding algorithm. Both models match satisfactorily with the experimental observations.

4.5 Response analysis

The detailed procedure to construct translation models for the responses based on Model 2 is shown. Let $X(t) = [X_1(t), X_2(t), X_3(t)]^T$ be the three-dimensional response vector process for the linear system. The components of $X(t), X_1(t), X_2(t)$, and $X_3(t)$ are along-wind and across-wind displacements and rotation, respectively. The vector process $X(t)$ satisfies the equation of motion for a three-degrees-of-freedom system

$$MX(t) + DX(t) + KX(t) = C(t), \tag{4.29}$$

where M, D, and K = mass, damping, and stiffness matrices; and $C(t) = [C_x(t), C_y(t), C_z(t)]^T$ is the wind-load vector process, where $C_x(t), C_y(t)$, and $C_z(t)$ are given by Eqs. 4.12-4.14. Let $\Psi = [\psi_1, \psi_2, \psi_3]$ be a 3×3 matrix whose columns are modal shapes and

$$Y(t) = \Psi^{-1} X, \tag{4.30}$$

be the modal responses. Writing Eq. 4.29 in terms of $Y(t)$ gives

$$\ddot{Y}_k(t) + 2\zeta_k \omega_k \dot{Y}_k(t) + \omega_k^2 Y_k(t) = \frac{\hat{C}_k(t)}{M_k}, \qquad k = 1, 2, 3, \tag{4.31}$$

where $Y_k(t)$ = components of $Y(t)$; and ζ_k, ω_k, and M_k = modal damping ratios, natural frequencies, and masses. The modal forcing functions have the expressions $\hat{C}_k(t) = [\Psi^T C(t)]_k$. Without loss of generality, $M_k = 1$ is set.

4.5.1 Second-moment properties

The mean of $X(t)$ is defined by $E[X(t)] = \sum_{k=1}^{3} \psi_k E[Y_k(t)] = \sum_{k=1}^{3} \psi_k E[\hat{C}_k(t)]/\omega_k^2$. This equation results from Eqs. 4.30 and 4.31.

Similarly, the spectral density of $X(t)$, denoted by $S_X(\nu)$, is

$$S_X(\nu) = F\{E[X(t+\gamma)X^T(t)]\} = \sum_{k=1}^{3}\sum_{q=1}^{3} \psi_k \psi_q^T S_{Y_k Y_q}(\nu), \tag{4.32}$$

where $S_{Y_k Y_q}(\nu)$ = cross-spectral density of arbitrary modal displacement pairs $Y_k(t), Y_q(t), k, q = 1, 2, 3.S_{Y_k Y_q}(\nu)$ can be calculated in two steps. First, $Y_k(t), Y_q(t)$ follows the equation [21](p. 189)

$$\frac{d}{dt}\tilde{Y}(t) = A\tilde{Y}(t) + gC(t) = \begin{pmatrix} A_k & 0 \\ 0 & A_q \end{pmatrix} \tilde{Y}(t) + gC(t), \tag{4.33}$$

where $\tilde{Y}(t) = [Y_k(t), \dot{Y}_k(t), Y_q(t), \dot{Y}_q(t)]^T; \hat{C}(t) = [\hat{C}_k(t), \hat{C}_q(t)]^T$; $g = 4 * 2$ matrix with the first column $[0, 1, 0, 0]^T$ and the second column $[0, 0, 0, 1]^T$; and $A_k = 2 * 2$ matrix with components $A_k(1,1) = 0$, $A_k(1,2) = 1$, $A_k(2,1) = -\omega_k^2$, and $A_k(2,2) = -2\zeta_k\omega_k$. Second, let $S_{\tilde{Y}}(\nu) = \mathcal{F}E[\tilde{Y}(t+\gamma)\tilde{Y}^T(t)]$ and $S_C(\nu) = E[C(t+\gamma)C^T(t)]$ be the spectral densities of $Y(t)$ and $C(t)$, respectively. $S_Y(\nu)$ relates $S_C(\nu)$ through the equation [21](p. 195)

$$S_{\tilde{Y}}(\nu) = H^*(\nu)S_C(\nu)H^T(\nu), \tag{4.34}$$

where $*$ indicates the complex conjugate; and $H(\nu) = (\sqrt{-1}\nu I - A)^- 1g$, in which I is a 4×4 identity matrix. $S_{Y_k Y_q}(\nu)$ is the component (1,3) or (3,1) of $S_Y(\nu)$

Fig. 4.4 shows one example for the spectral densities of modal responses. The solid line is the estimate from experimental records and dashed line is calculated from Eq. 4.34.

4.5.2 Marginal moments and distributions

Moment equations developed from Itô's formula are used to calculate exactly the marginal moments of $X(t)$, then its marginal distributions are inferred.

Let $X_i(t), i = 1, 2, 3$, be the ith component of $X(t)$. The n^{th} marginal moments $E[X_i^n(t)]$ of $X_i(t)$ have the expression

$$\begin{aligned} E[X_i^n(t)] &= E\{[\psi_{i,1}Y_1(t) + \psi_{i,2}Y_2(t) + \psi_{i,3}Y_3(t)]^n\} \\ &= \sum_{\alpha,\beta,\gamma} \frac{n!}{\alpha!\beta!\gamma!}\psi_{i,1}^{\alpha}\psi_{i,2}^{\beta}\psi_{i,3}^{\gamma}E[Y_1^{\alpha}(t)Y_2^{\beta}(t)Y_3^{\gamma}(t)], \end{aligned} \tag{4.35}$$

in which $\alpha+\beta+\gamma = n$; and $\psi_{i,1}, \psi_{i,2}$, and $\psi_{i,3}$ = first, second, and third component of mode ψ_i, respectively. The values of $Y_k(t)$, $k = 1, 2, 3$, are governed by Eq. 4.31 and the $\hat{C}_k(t) = \psi_{k,1}C_x(t) + \psi_{k,2}C_y(t) + \psi_{k,3}C_z(t)$. Substituting the preceding expression in Eq. 4.31 gives.

$$\ddot{Y}_k(t) + 2\zeta_k\omega_k\dot{Y}_k(t) + \omega_k^2 Y_k(t) = \psi_{k,1}C_x(t) + \psi_{k,2}C_y(t) + \psi_{k,3}C_z(t), \tag{4.36}$$

Because Eq. 4.36 is linear, $Y_k(t)$ is decomposed by $Y_k(t) = \psi_{k,1}Y_{k,x}(t) + \psi_{k,2}Y_{k,y}(t) + \psi_{k,3}Y_{k,z}(t)$, where $Y_{k,x}(t), Y_{k,y}(t)$ and $Y_{k,z}(t)$ are the responses corresponding to wind loads $C_x(t), C_y(t)$, and $C_z(t)$, respectively. Then $E[Y_1(t)^{\alpha}Y_2(t)^{\beta}Y_3(t)^{\gamma}]$ are calculated from the moments of $Y_{k,x}(t), Y_{k,y}(t)$ and $Y_{k,z}(t)$ by

$$\begin{aligned} &E[Y_1^{\alpha}(t)Y_2^{\beta}(t)Y_3^{\gamma}(t)] \\ &= \sum_{\alpha_1\alpha_2\alpha_3}\sum_{\beta_1\beta_2\beta_3}\sum_{\gamma_1\gamma_2\gamma_3} \frac{\alpha!}{\alpha_1!\alpha_2!\alpha_3!}\frac{\beta!}{\beta_1!\beta_2!\beta_3!}\frac{\gamma!}{\gamma_1!\gamma_2!\gamma_3!} = \prod_{i=1}^{3}\psi_{1,i}^{\alpha_i}\prod_{j=1}^{3}\psi_{2,j}^{\beta_j}\prod_{k=1}^{3}\psi_{3,k}^{\gamma_k} \\ &E[Y_{1,x}^{\alpha_1}(t)Y_{2,x}^{\beta_1}(t)Y_{3,x}^{\gamma_1}(t)]E[Y_{1,y}^{\alpha_2}(t)Y_{2,y}^{\beta_2}(t)Y_{3,y}^{\gamma_2}(t)Y_{1,z}^{\alpha_3}(t)Y_{2,z}^{\beta_3}(t)Y_{3,z}^{\gamma_3}(t)] \end{aligned} \tag{4.37}$$

where $\alpha_1 + \alpha_2 + \alpha_3 = \alpha; \beta_1 + \beta_2 + \beta_3 = \beta$; and $\gamma_1 + \gamma_2 + \gamma_3 = \gamma$. The preceding equation follows from the fact that $Y_{k,x}(t)$ are independent of $Y_{k,y}(t)$ and $Y_{k,z}(t)$. Because $C_y(t)$ and $C_(t)$ are correlated Gaussian processes, so are the responses $Y_{k,y}(t)$ and $Y_{k,z}(t)$, and higher-order moments of $Y_{k,y}(t)$ and $Y_{k,z}(t)$ in Eq. 4.37 result from their second-moment properties. Let $\mu(\alpha_1, \alpha_1', \alpha_2, \alpha_2', \alpha_3, \alpha_3', r) = E[Y_{1,x}^{\alpha_1}(t)\dot{Y}_{1,x}^{\alpha_1'}(t)Y_{2,x}^{\beta_1}(t)\dot{Y}_{2,x}^{\beta_1'}(t)Y_{3,x}^{\gamma_1}(t)\dot{Y}_{3,x}^{\gamma_1'}(t)\tilde{u}(t)]$

be the moments of vector $[Y_{1,x}(t), \dot{Y}_{1,x}(t), Y_{2,x}(t), \dot{Y}_{2,x}(t), Y_{3,x}(t), \dot{Y}_{3,x}(t), \tilde{u}(t)]$. $\mu(\alpha_1, \alpha_1', \alpha_2, \alpha_2', \alpha_3, \alpha_3', r)$ satisfy the moment equations derived from Itô's formula [25], i.e.

$$
\begin{aligned}
0 &= \alpha_1\mu(\alpha_1 - 1, \alpha_1' + 1, ...) + \alpha_2\mu(..., \alpha_2 - 1, \alpha_2' + 1, ...) + \alpha_3\mu(..., \alpha_3 - 1, \alpha_3' + 1, r) \\
&- \alpha_1'\omega_1^2\mu(\alpha_1 + 1, \alpha_1' - 1, ...) - \beta_1'\omega_2^2\mu(..., \beta_1 + 1, \beta_1' - 1, ...) \\
&- \gamma_1'\omega_3^2\mu(..., \gamma_1 + 1, \gamma_1' - 1, r) - (2\alpha_1'\zeta_1\omega_1 + 2\beta_1'\zeta_2\omega_2 + 2\gamma_1'\zeta_3\omega_3 + r\alpha_u)\mu(...) \\
&+ \alpha_1' C_d \sum_{p=0}^{2} a_l \mu(\alpha_1, \alpha_1' - 1, ..., r + l) + \beta_1' C_d \sum_{p=0}^{2} a_l \mu(..., \beta_1, \beta_1' - 1, ..., r + l) \\
&+ \gamma_1' C_d \sum_{p=0}^{2} a_l \mu(..., \gamma_1, \gamma_1' - 1, ..., r + l) + r(r-1)\alpha_u\sigma_u^2\mu(..., r - 2),
\end{aligned} \tag{4.38}
$$

with the notations $a_0 = 1, a_1 = 2/\overline{U}^2$, and $a_2 = 1/\overline{U}^2$. The set of these moment equations is expressed in closed form so that $\mu(\alpha_1, \alpha_1', \alpha_2, \alpha_2', \alpha_3, \alpha_3', r)$ can be exactly calculated. The moments of $Y_{k,x}(t)$ are obtained by setting $E[Y_{1,x}^{\alpha_1}(t)Y_{2,x}^{\beta_1}(t)Y_{3,x}^{\gamma_1}(t)] = \mu(\alpha_1, 0, \beta_1, 0, \gamma_1, 0, 0)$.

Denote by $\mu_i(n)$ the n^{th} marginal moment $E[X_i^n(T)]$.The marginal distribution if $X_i(t)$ is approximated by $\hat{F}_i(x) = \sum_{\mathrm{j}=1}^{N} p_{ij}\hat{F}_{ij}(x)$, where$\hat{F}_{ij}(x)$ are the preselected distributions with mean $\mu_i(1)$ and variance $\mu_i(2) - \mu_i(1)^2, p_{ij} \geq 0$, are the parameters that minimize the error $\sum_{n=1}^{4}[\mu_i(n) - \hat{\mu}_i(n)]^2$ under the constraint $\sum_{j=1}^{N} p_{ij} = 1$ in which $[\hat{\mu}_i(n), n = 1, ..., 4]$ are the marginal moments of $\hat{F}_i(x)$. Note that $\hat{F}_i(x)$ are non-Gaussian because the along-wind forces are non-Gaussian

Response Translation Models The previous sections have shown that (1) structural responses are non-Gaussian, and (2) the marginal distributions and the second moment properties of the responses can be estimated. In order to model these responses, so-called translation models that constitute one-to-

one mappings between Gaussian processes and non-Gaussian processes that have the target marginal distributions and similar second-moment properties are used. The components $X_{T,i}(t)$ of the translation model $X_T(t)$ are defined by

$$X_{T,i}(t) = \hat{F}_i^{-1}\Phi[Z_i(t)] \tag{4.39}$$

where Φ denotes standard Gaussian distribution; and $[Z_i(t)]$ = components of $Z(t)$, which is a Gaussian vector process with zero mean, unit variance, and spectral density $S_Z(\nu) \geq 0$ that minimizes the difference between the spectral density of $X_T(t), S_{X_T}(\nu)$, and $S_X(\nu)$. The properties of this translation model can be found in, e.g., [17](Section 3.1.1). Based on the observation that the discrepancy between these two spectral densities is generally small irrespective of the choice of $S_Z(\nu)$. The probability law of the translation model $X_T(t)$ is fully characterized.

4.5.3 Mean outcrossing rates

Suppose the system in Eq. 4.29 is safe if its responses approximated by $X_T(x)$ do not leave the rectangular safe set $D_x = \times_{i=1}^{3}[-\zeta x_i, \zeta x_i]$, where $x_i > 0$ is constant and $\zeta > 0$ is the scale factor controlling the size of the safe set. The average number crossings of $X_T(t)$ out of D_x per unit of time, referred to an mean D_x-outcrossing rate, are of interest. Denote the image of the safe set D_x in the Gaussian space by $D_z = \times_{i=1}^{3}[z_i^-, z_i^+]$, where $z_i^+ = \Phi^{-1}[\hat{F}_i(\xi x_i)]$ and $z_i^- = \Phi^{-1}[\hat{F}_i(-\xi x_i)]$. Because $X_T(t)$ crosses safe set D_x if and only if its mapped Gaussian image $Z(t)$ crosses D_z, the mean D_x-outcrossing rate coincides with the mean D_z-outcrossing rate of $Z(t)$, denoted by λ_{D_z}. For arbitrary safe set, λ_{D_z}

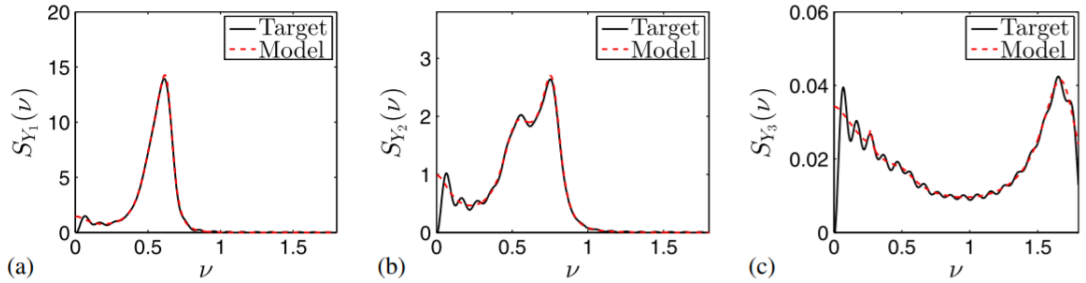

Figure 4.4: Example for the spectral densities of modal responses:(a) $Y_1(t)$; $(b)Y_2(t)$; $(c)Y_3(t)$

,

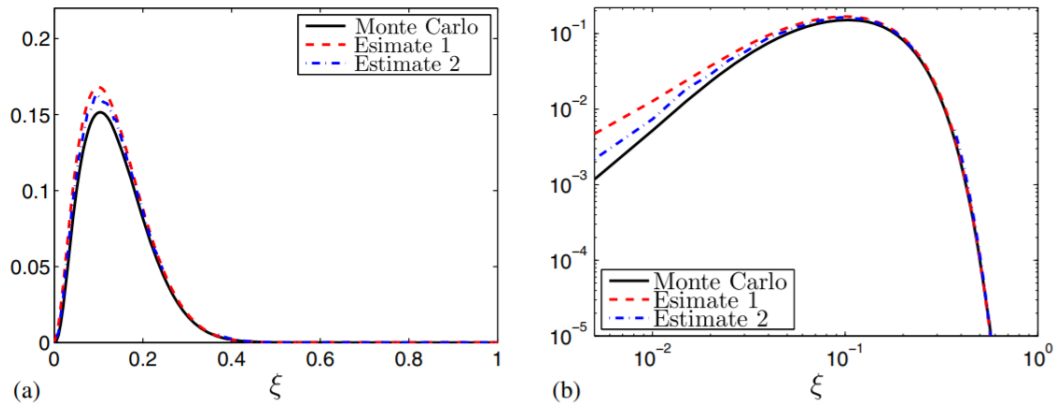

Figure 4.5: Mean D_x-outcrossing rates:(a) linear scales; (b) logarithmic scales

has the form [21](p.300)

$$\lambda_{D_Z} = \int_{\partial D_z} u(z) f(z) d\sigma(z), \tag{4.40}$$

where ∂D_z denotes the boundaries of the safe set $D_z; \in \partial D_z; f(z)$ = probability density function of $Z(t)$; $\sigma(z)$ = surface area measured on ∂D_z; and

$$u(z) = E[\dot{Z}_n(t)+ \mid Z(t) = z] \tag{4.41}$$

where $\dot{Z}_n(t)$ + denotes the positive projection of the velocity $\dot{Z}(t)$ on the outer normal $n(z)$ to ∂D_z.

For a rectangular safe set D_z with six planar boundaries, Eq. 4.40 yields

$$\lambda_{D_z} = \sum_{i=1}^{3} [\lambda_{\partial D_{z_i^+}} + \lambda_{\partial D_{z_i^-}}], \tag{4.42}$$

where $\lambda_{\partial D_{z_i^+}}$ = mean rate at which $Z_i(t)$ crosses boundary $\partial D_{z_i^+}$ at distance Z_i^+ from the origin and with outer normal n_i^+ along with the axis corresponding to $Z_i(t)$; and $\lambda_{\partial D_{z_i^-}}$ is defined similarly. The value of $\lambda_{\partial D_{z_i^+}}$ can be calculated by

$$\lambda_{\partial D_{z_i^+}} = u_i(Z_i^+)P(Z_{\neq i}(t) \in \partial D_{z_i}+ \mid Z_i(t) = z_i^+)f(z_i^+), \tag{4.43}$$

where $Z_{\neq i}(t)$ denotes $Z(t)$ excluding $Z_i(t)$; and $u_i(z_i^+) = E[\dot{Z}_i(t)+ \mid Z(t) = Z_i^+]$ is the corresponding $u(z)$ value on the boundary $\partial D_{z_i^+}$, in which $\dot{Z}_i(t)$ denotes the ith component of $\dot{Z}(t)$ and $Z_i^+ \in \partial D_{z_i^+}$. $\dot{Z}_i(t)$ is independent of $Z(t)$ under some conditions (Appendix D), and it is a Gaussian variable with mean zero and variance $\Gamma_{\dot{Z}i\dot{Z}_i}$,where $\Gamma_{\dot{Z}i\dot{Z}_i} = \int_0^\infty \nu^2 S_{\dot{Z}i\dot{Z}_i}(\nu)dv$ and $S_{\dot{Z}i\dot{Z}_i}(\nu)$ is the spectral density of $Z_i(t)$. Accordingly, $u_i(Z_i^+)$ becomes a constant $u_i^+, i.e., u_i^+ = (\Gamma_{\dot{Z}i\dot{Z}_i}/2\pi)^{12}$. The same procedure can be used to calculate $\lambda_{\partial D_{z_i^-}}$ with threshold value z_i^-.

However, Eq. 4.43 may be computationally demanding because of the probability $P(Z_{\neq i}(t) \in \partial D_{Z_i}+ \mid Z_i(t) = z_i^+)$. This paper proposes to estimate this term from samples of $Z(t)$ for relatively smallz_i^+ and set $P(Z_{\neq i}(t) \in \partial D_{Z_i}+ \mid Z_i(t) = z_i^+) \simeq 1$ for relatively large values of z_i^+. Then, $\lambda_{\partial D_{z_i^+}} \simeq u_i^+ f(z_i^+)$ for relatively large z_i^+.

Fig. 4.5 shows the mean D_x-outcrossing rate of $X(t)$. The solid line is estimated from the response samples that are obtained from the Monte Carlo simulation based on samples of the empirical model, the lighter dashed line is the proposed approximation of Eq. 4.42. They are almost indistinguishable at the figure scale in the tail region.

4.6 Chapter summary

Probabilistic models have been constructed for wind loads based on (1) the existing wind-load model proposed in [52], and (2) the empirical or mathematical models for the second-moment properties of turbulence fluctuations and wake excitations. The empirical model follows from the experimental observations and knowledge of the physics, while the mathematical model represents the turbulence fluctuations and wake excitations by the filtered Gaussian processes with similar second-moment properties as the empirical model. It has been shown that both models agree with the experimental observations.

The mathematical model provides an efficient method to estimate the response properties of linear systems relative to the classical Monte Carlo simulation. The responses are modeled by the translation processes calibrated to the second-moment properties and the marginal distributions of the responses. Linear random vibration theory is applied to find the target second-moment properties, and the marginal distributions match the exact marginal moments that are obtained by the moment equations developed from Itô's formula. Then, response properties are approximated by the corresponding properties of the resulting translation processes. For example, crossing theory for translation processes is used to assess the structural reliability. The accuracy of this approximation is satisfactory as shown in the numerical example.

CHAPTER 5

CONCLUSIONS

5.1 Conclusions

This dissertation is concerned with the assessment of structural performance during catastrophic wind events. The assessment involves two steps: (1) probabilistic characterization of wind loads, and (2) statistical evaluation of structural responses to wind loads.

For step 1, we demonstrated that Gaussian models are not adequate to represent wind loads obtained from experimental tests. The limitations of existing non-Gaussian models, i.e., independent component analysis (ICA), third-order SRM, polynomial chaos, and translation model, have been discussed and are outlined as follows:

- ICA can represent exactly or asymptotically in tails the non-Gaussian random vectors if (1) their characteristic functions satisfy special conditions, or (2) their tails are independent. Nevertheless, the representation based on ICA fails for a broad range of non-Gaussian vectors and is approximately Gaussian for high dimensional vectors.
- Third-order SRM cannot distinguish between processes which have the same third-moment properties.
- Polynomial chaos approximation converges in L_2 and in finite-dimensional distribution to the target process. However, the convergence rate is slow for estimating the distribution of extreme and the construction of the approximation requires high truncation level for accuracy.

- Translation model has been illustrated using a test case that it provides better approximation on the distribution of extreme in comparison to the third-order SRM and polynomial chaos. Its performance is superior if the tail dependence of the target process is weak, but deteriorates as such dependence increases.

In order to overcome the limitations of existing non-Gaussian models, we proposed the use of copula-based Markov model. The model is capable of matching the marginal distribution and approximating satisfactorily the second-moment and third-moment properties. The estimate on the distribution of extreme based on this model is remarkable irrespective of the tail dependence of the target process.

For step 2, an accurate and efficient method has been developed to estimate the statistical properties of structural responses to wind loads. The structural responses have been approximated by the translation model calibrated to the second-moment properties and the marginal distributions of the responses. These two quantities have been obtained by linear random vibration theory and moment equations, respectively. We showed that the reliability estimate based on this method is accurate through numerical examples. In addition, the proposed method is more efficient than the classical Monte Carlo simulation.

5.2 Future work

We identify two future directions of our work:

• The copula-based Markov model shown in chapter 3 is developed for stochastic processes which only represent the wind-load time series at one location on the structure. Extension of this model will be required to incorporate the spatial variation of wind loads in the analysis.

• Surrogate models will be considered as an alternative to the approach presented in chapter 4 to bypass the Monte Carlo simulation. They are more computationally efficient, and have the potential to be more accurate in comparison to the approach in chapter 4.

APPENDIX A

PROOF OF THE THIRD-MOMENT CONVERGENCE OF THIRD-ORDER SRM

First, note that $c(\tau_1, \tau_2) = \iint_{\mathcal{R}^2} B(\omega_1, \omega_2) \exp[i(\omega_1\tau_1 + \omega_2\tau_2)]d\omega_1 d\omega_2 = \iint_{A_1+A_2} B(\omega_1, \omega_2) \exp[i(\omega_1\tau_1 + \omega_2\tau_2)]d\omega_1 d\omega_2 + \iint_{A_3+A_4} B(\omega_1, \omega_2) \exp[i(\omega_1\tau_1 + \omega_2\tau_2)]d\omega_1 d\omega_2 + \iint_{A_5+A_6} B(\omega_1, \omega_2) \exp[i(\omega_1\tau_1 + \omega_2\tau_2)]d\omega_1 d\omega_2$, where $A_1, \ldots, A_6$ are areas labeled in Fig. A.1. By the symmetry properties of $B(\omega_1, \omega_2)$ and integra-

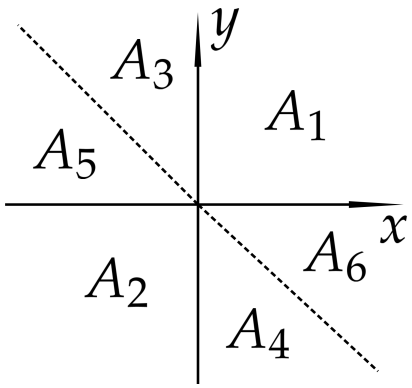

Figure A.1: Partition of $\mathcal{R}^2$

tion by substitution, it can be shown that

$$\begin{aligned}
&\iint_{A_1+A_2} B(\omega_1,\omega_2)\exp[i(\omega_1\tau_1+\omega_2\tau_2)]d\omega_1 d\omega_2 \\
=&2\int_0^\infty\int_0^\infty \Re(B(\omega_1,\omega_2))\cos(\omega_1\tau_1+\omega_2\tau_2) \\
&-\Im(B(\omega_1,\omega_2))\sin(\omega_1\tau_1+\omega_2\tau_2)d\omega_1 d\omega_2; \qquad \text{(A.1)} \\
&\iint_{A_3+A_4} B(\omega_1,\omega_2)\exp[i(\omega_1\tau_1+\omega_2\tau_2)]d\omega_1 d\omega_2 \\
=&2\int_0^\infty\int_0^\infty \Re(B(\omega_1,\omega_2))\cos(\omega_1(\tau_2-\tau_1)+\omega_2\tau_2) \\
&+\Im(B(\omega_1,\omega_2))\sin(\omega_1(\tau_2-\tau_1)+\omega_2\tau_2)d\omega_1 d\omega_2; \qquad \text{(A.2)} \\
&\iint_{A_5+A_6} B(\omega_1,\omega_2)\exp[i(\omega_1\tau_1+\omega_2\tau_2)]d\omega_1 d\omega_2 \\
=&2\int_0^\infty\int_0^\infty \Re(B(\omega_1,\omega_2))\cos(-\omega_1\tau_1+\omega_2(\tau_2-\tau_1)) \\
&-\Im(B(\omega_1,\omega_2))\sin(-\omega_1\tau_1+\omega_2(\tau_2-\tau_1))d\omega_1 d\omega_2. \qquad \text{(A.3)}
\end{aligned}$$

We derive Eq. A.2 for illustration. From the observation in Fig. A.1,

$$\begin{aligned}
&\iint_{A_3} B(\omega_1,\omega_2)\exp[i(\omega_1\tau_1+\omega_2\tau_2)]d\omega_1 d\omega_2 \\
=&\int_{-\infty}^0\int_{-\omega_1}^\infty B(\omega_1,\omega_2)\exp[i(\omega_1\tau_1+\omega_2\tau_2)]d\omega_2 d\omega_1 \qquad \text{(A.4)}
\end{aligned}$$

Set $\omega_1=-\omega_1'$ and $\omega_2=\omega_1'+\omega_2'$. By integration by substitution, Eq. A.4 yields

$$\begin{aligned}
&\iint_{A_3} B(\omega_1,\omega_2)\exp[i(\omega_1\tau_1+\omega_2\tau_2)]d\omega_1 d\omega_2 \\
=&\int_0^\infty\int_0^\infty B(-\omega_1',\omega_1'+\omega_2')\exp[i(-\omega_1'\tau_1+(\omega_1'+\omega_2')\tau_2)]d\omega_2' d\omega_1' \\
=&\int_0^\infty\int_0^\infty B^*(\omega_1',\omega_2')\exp[i(\omega_1'(\tau_2-\tau_1)+\omega_2'\tau_2]d\omega_2' d\omega_1', \qquad \text{(A.5)}
\end{aligned}$$

where $B^*(\omega_1',\omega_2')$ denotes the complex conjugate of $B(\omega_1',\omega_2')$ and the last equality follows from the symmetry properties of $B(\omega_1',\omega_2')$. Similarly, we have

$$\begin{aligned}
&\iint_{A_4} B(\omega_1,\omega_2)\exp[i(\omega_1\tau_1+\omega_2\tau_2)]d\omega_1 d\omega_2 \\
=&\int_0^\infty\int_0^\infty B(\omega_1',\omega_2')\exp[i(\omega_1'(\tau_1-\tau_2)-\omega_2'\tau_2]d\omega_2' d\omega_1'. \qquad \text{(A.6)}
\end{aligned}$$

The summation of Eqs. A.5 and A.6 yields Eq. A.2.

Second, we derive the expression of $E[\tilde{X}_m^{SR}(t)\tilde{X}_m^{SR}(t+\tau_1)\tilde{X}_m^{SR}(t+\tau_2)]$. The three non-zero terms in the expansion of $E[\tilde{X}_m^{SR}(t)\tilde{X}_m^{SR}(t+\tau_1)\tilde{X}_m^{SR}(t+\tau_2)]$ are

$$8\sum_{s=1}^{N}\sum_{\omega_k+\omega_l=\omega_s}\sqrt{S_p(\omega_k)S_p(\omega_l)S(\omega_s)\Delta\omega_k\Delta\omega_l\Delta\omega_s b_p^2(\omega_l,\omega_k)}$$

$$E[\cos(\omega_k t-\phi_k)\cos(\omega_l(t+\tau_1)-\phi_l)\cos((\omega_k+\omega_l)(t+\tau_2)-(\phi_k+\phi_l+\beta(\omega_l,\omega_k)))]; \tag{A.7}$$

$$8\sum_{k=1}^{N}\sum_{\omega_l+\omega_s=\omega_k}\sqrt{S_p(\omega_l)S_p(\omega_s)S(\omega_k)\Delta\omega_k\Delta\omega_l\Delta\omega_s b_p^2(\omega_l,\omega_s)}$$

$$E[\cos((\omega_l+\omega_s)t-(\phi_l+\phi_s+\beta(\omega_l,\omega_s)))\cos(\omega_l(t+\tau_1)-\phi_l)\cos(\omega_s(t+\tau_2)-\phi_s)]; \tag{A.8}$$

$$8\sum_{l=1}^{N}\sum_{\omega_k+\omega_s=\omega_l}\sqrt{S_p(\omega_k)S_p(\omega_s)S(\omega_l)\Delta\omega_k\Delta\omega_l\Delta\omega_s b_p^2(\omega_k,\omega_s)}$$

$$E[\cos(\omega_k t-\phi_k)\cos((\omega_k+\omega_s)(t+\tau_1)-(\phi_k+\phi_s+\beta(\omega_k,\omega_s)))\cos(\omega_s(t+\tau_2)-\phi_s)]. \tag{A.9}$$

The expectations in the above three expressions are

$$E[\cos(\omega_k t-\phi_k)\cos(\omega_l(t+\tau_1)-\phi_l)\cos((\omega_k+\omega_l)(t+\tau_2)-(\phi_k+\phi_l+\beta(\omega_l,\omega_k)))]$$
$$=\frac{1}{4}\cos(\beta(\omega_k,\omega_l)-[\omega_k(\tau_2-\tau_1)+\omega_l\tau_2]); \tag{A.10}$$

$$E[\cos((\omega_l+\omega_s)t-(\phi_l+\phi_s+\beta(\omega_l,\omega_s)))\cos(\omega_l(t+\tau_1)-\phi_l)\cos(\omega_s(t+\tau_2)-\phi_s)]$$
$$=\frac{1}{4}\cos(\beta(\omega_s,\omega_l)+[\omega_l\tau_1+\omega_s\tau_2]); \tag{A.11}$$

$$E[\cos(\omega_k t-\phi_k)\cos((\omega_k+\omega_s)(t+\tau_1)-(\phi_k+\phi_s+\beta(\omega_k,\omega_s)))\cos(\omega_s(t+\tau_2)-\phi_s)]$$
$$=\frac{1}{4}\cos(\beta(\omega_k,\omega_s)+[\omega_k(-\tau_1)+\omega_s(\tau_2-\tau_1)]). \tag{A.12}$$

By substituting Eqs. A.10, A.11, and A.12 into expressions A.7, A.8, and A.9,

expressions A.7, A.8, and A.9 become

$$
\begin{aligned}
&2\sum_{s=1}^{N}\sum_{\omega_k+\omega_l=\omega_s}|B(\omega_k,\omega_l)|\Delta\omega_k\Delta\omega_l\cos(\beta(\omega_k,\omega_l)-[\omega_k(\tau_2-\tau_1)+\omega_l\tau_2]) \\
=&2\sum_{s=1}^{N}\sum_{\omega_k+\omega_l=\omega_s}\{\Re(B(\omega_k,\omega_l))\cos[\omega_k(\tau_2-\tau_1)+\omega_l\tau_2] \\
&+\Im(B(\omega_k,\omega_l))\sin[\omega_k(\tau_2-\tau_1)+\omega_l\tau_2]\}\Delta\omega_k\Delta\omega_l; \qquad \text{(A.13)} \\
&2\sum_{k=1}^{N}\sum_{\omega_l+\omega_s=\omega_k}|B(\omega_l,\omega_s)|\Delta\omega_l\Delta\omega_s\cos(\beta(\omega_s,\omega_l)+[\omega_l\tau_1+\omega_s\tau_2]) \\
=&2\sum_{k=1}^{N}\sum_{\omega_l+\omega_s=\omega_k}\{\Re(B(\omega_l,\omega_s))\cos[\omega_l\tau_1+\omega_s\tau_2] \\
&-\Im(B(\omega_l,\omega_s))\sin[\omega_l\tau_1+\omega_s\tau_2]\}\Delta\omega_l\Delta\omega_s; \qquad \text{(A.14)} \\
&2\sum_{l=1}^{N}\sum_{\omega_k+\omega_s=\omega_l}|B(\omega_k,\omega_s)|\Delta\omega_k\Delta\omega_s\cos(\beta(\omega_k,\omega_s)+[\omega_k(-\tau_1)+\omega_s(\tau_2-\tau_1)]) \\
=&2\sum_{l=1}^{N}\sum_{\omega_k+\omega_s=\omega_l}\{\Re(B(\omega_k,\omega_s))\cos[\omega_k(-\tau_1)+\omega_s(\tau_2-\tau_1)] \\
&-\Im(B(\omega_k,\omega_s))\sin[\omega_k(-\tau_1)+\omega_s(\tau_2-\tau_1)]\}\Delta\omega_k\Delta\omega_s. \qquad \text{(A.15)}
\end{aligned}
$$

Note that Eqs. A.13, A.14, and A.15 are the Riemann sums of Eqs. A.2, A.1, and A.3, respectively. This implies that $E[\tilde{X}_m^{SR}(t)\tilde{X}_m^{SR}(t+\tau_1)\tilde{X}_m^{SR}(t+\tau_2)]$ converges to $c(\tau_1,\tau_2)$ as $m\to\infty$ which completes the proof.

APPENDIX B

EXAMPLES OF M-COPULAS

<table>
<tr><td rowspan="6">$m = 2$</td><td colspan="4">Archimedean Copulas: $C(\boldsymbol{u}) = \varphi^{-1}(\varphi(u_1) + \varphi(u_2))$, where φ = continuous, strictly decreasing functions from $[0,1]$ to $[0,\infty)$ s.t. $\varphi(0) = \infty$, $\varphi(1) = 0$, and its inverse is completely monotonic, i.e., $(-1)^k d^k \varphi^{-1}(x)/dx^k \geq 0$.</td></tr>
<tr><td>Examples</td><td>Parameters</td><td>Properties</td><td>Ref.</td></tr>
<tr><td>$C(\boldsymbol{u}) = (u_1^{-\theta} + u_2^{-\theta} - 1)^{-1/\theta}$
$C(\boldsymbol{u}) = \exp\big(-[(-\log u_1)^\theta + (-\log u_2)^\theta]^{1/\theta}\big)$
$C(\boldsymbol{u}) = u_1 u_2/[1-\theta(1-u_1)(1-u_2)]$</td><td>$\theta \geq 0$
$\theta \geq 1$
$-1 \leq \theta < 1$</td><td>symmetric</td><td>[45]</td></tr>
<tr><td colspan="4">Generalized Archimedean Copulas: $C(\boldsymbol{u}) = \psi\big[\sum_{j=1}^{2} h_{j1}(\psi^{-1}(u_1)) h_{j2}(\psi^{-1}(u_2))/2\big]$, where ψ = continuous functions s.t. $\psi(0) = 0$, $\psi(1) = 1$, $\psi'(x) > 0$, $\psi''(x) \geq 0$, $\forall x \in [0,1]$, and $h_{jk}(x), j,k = 1,2,=$ differentiable and strictly increasing functions with $h_{jk}(0) = 0$, $h_{jk}(1) = 1$, and $\sum_{j=1}^{2} h_{jk}(x)/2 = x$.</td></tr>
<tr><td>Examples</td><td>Parameters</td><td>Properties</td><td>Ref.</td></tr>
<tr><td>$\psi(x) = -\log(1-(1-e^{-\theta})x)/\theta$
$\psi(x) = (e^{\theta x} - 1)/(e^\theta - 1)$
$h_{1k}(x) = (e^{a_{1k}x} - 1)/(e^{a_{1k}} - 1)$, $h_{2k}(x) = 2x - h_{1k}(x)$
$h_{1k}(x) = (a_{1k}+1)x/(1+a_{1k}x)$, $h_{2k}(x) = 2x - h_{1k}(x)$</td><td>$\theta \geq 0$
$\theta \geq 0$
$0 < a_{1k} < 1.594$
$-0.5 < a_{1k} \leq 1$</td><td>asymmetric</td><td>[42]</td></tr>
</table>

Table B.1: Examples of m-copulas

<table>
<tr><td rowspan="4">$m = 3$</td><td colspan="4">Archimedean Copulas with Concordance: $C(\boldsymbol{u}) = \varphi_{\theta_1}(\varphi_{\theta_1}^{-1} \circ \varphi_{\theta_2}(\varphi_{\theta_2}^{-1}(u_1) + \varphi_{\theta_2}^{-1}(u_3)) + \varphi_{\theta_1}^{-1}(u_2))$, where $\varphi_{\theta_1}, \varphi_{\theta_2}$ = functions φ defined in Archimedean Copulas with parameters θ_1 and θ_2.</td></tr>
<tr><td>Examples</td><td>Parameters</td><td>Properties</td><td>Ref.</td></tr>
<tr><td>$C(\boldsymbol{u}) = \left((u_1^{-\theta_2} + u_3^{-\theta_2} - 1)^{\theta_1/\theta_2} + u_2^{-\theta_1} - 1\right)^{-1/\theta_1}$</td><td>$\theta_1 > \theta_2 > 0$</td><td>Partially symm.*,</td><td rowspan="2">[34]</td></tr>
<tr><td>$C(\boldsymbol{u}) = \exp\left\{-\left([z_1^{\theta_2} + z_3^{\theta_2}]^{\theta_1/\theta_2} + z_2^{\theta_1}\right)^{1/\theta_1}\right\}$, $z_k = -\log u_k$</td><td>$\theta_1 > \theta_2 \geq 1$</td><td>concordant**</td></tr>
<tr><td rowspan="4">$m \geq 3$</td><td colspan="4">Other Copulas with General Dependence:</td></tr>
<tr><td>Examples</td><td>Parameters</td><td>Properties</td><td>Ref.</td></tr>
<tr><td>$C(\boldsymbol{u}) = \exp\Big\{-\Big[\sum_{l=1}^{m-1}\sum_{k=1}^{m-l}((p_k z_k^\theta)^{\delta_{k,k+l}} + (p_{k+l} z_{k+l}^\theta)^{\delta_{k,k+l}})^{1/\delta_{k,k+l}} + \sum_{k=1}^{m} \nu_k p_k z_k^\theta\Big]^{1/\theta}\Big\}$, $z_k = -\log u_k$, $p_k = (\nu_k + m - 1)^{-1}$</td><td>$\theta \geq 1$, $\delta_{k,k+l} \geq 1$, $\nu_k \geq 1$</td><td rowspan="2">Partially symm.*</td><td rowspan="2">[34]</td></tr>
<tr><td>$C(\boldsymbol{u}) = \exp\Big\{-\Big[\sum_{k=1}^{m} z_k^\theta - \sum_{l=1}^{m-1}\sum_{k=1}^{m-l}\left(p_{k+l}^{-\delta_{k,k+l}} z_{k+l}^{-\theta\delta_{k,k+l}} + p_k^{-\delta_{k,k+l}} z_k^{-\theta\delta_{k,k+l}}\right)^{-1/\delta_{k,k+l}}\Big]^{1/\theta}\Big\}$, $z_k = -\log u_k$, $p_k = (\nu_k + m - 1)^{-1}$</td><td>$\theta > 0$, $\delta_{k,k+l} > 0$, $\nu_k \geq 0$</td></tr>
</table>

Notes: $*$ If $m \geq 3$, m-copulas is partially symmetric if their marginals of order 2 to $m-1$ with consecutive arguments are equal. For example, a 3-copula is partially symmetric if bivariate marginals $C_{12}(u_1, u_2) = C_{23}(u_1, u_2), \forall u_1, u_2$. We require the partial symmetry for m-copulas because of the stationarity of the Markov model $\tilde{Q}_m(t)$.

$**$ Let C and C' be two 2-copulas. C' is more concordant than C, written $C \prec_c C'$, if $C(u_1, u_2) \leq C'(u_1, u_2), \forall u_1, u_2$. In this example, we have $C_{12} = C_{23} \prec_c C_{13}$, where C_{12}, C_{13}, C_{23} are the bivariate marginals of the 3-copula whose subscripts correspond to the reference subsets of collections of random variables.

Table B.2: Examples of m-copulas (Continue)

APPENDIX C

PROPERTY FROM FLOW SYMMETRY

This section proves that $E[\tilde{u}(t)\tilde{v}(t)] = 0$ if the flow geometry is symmetric about the $x_1 - x_3$ plane. Denote by $f(v_1, v_2; x, t) = \partial^2 \mathcal{F}(v_1, v_2; x, t)/\partial v_1 \partial v_2$ the probability density function of wind-velocity vector$[u(X,t), v(X,t)]^T$, in which $x = [x_1, x_2, x_3]$ and $\mathcal{F}(V_1, V_2; x, t) = P(u(X,t) \leq v_1, v(X,t) \leq v_2)$. Because of the flow symmetry, the statistics is invariant under the reflection of the x_2 coordinate axis so that

$$f(v_1, v_2; [x_1, x_2, x_3], t) = f(v_1, -v_2; [x_1, -x_2, x_3], t), \tag{C.1}$$

Then

$$\begin{aligned} E[v(0,0,H_3),t] &= \int_{-\infty}^{+\infty}\int_{-\infty}^{+\infty} v_2 f(v_1, v_2; [0,0,H_3], t) dv_1 dv_2 \\ &= \int_{-\infty}^{+\infty}\int_{-\infty}^{+\infty} (-v_2) f(v_1, -v_2; [0,0,H_3], t) dv_1 dv_2 \\ &= -E[v([0,0,H_3],t)] = 0 \end{aligned}$$

and

$$\begin{aligned} E[\tilde{u}(t)\tilde{v}(t)] &= E[u([0,0,H_3],t)\tilde{v}([0,0,H_3],t)] \\ &= E[u([0,0,H_3],t)v([0,0,H_3],t)] \\ &= \int_{-\infty}^{+\infty}\int_{-\infty}^{+\infty} v_1 v_2 f(v_1, v_2; [0,0,H_3], t) dv_1 dv_2 \\ &= \int_{-\infty}^{+\infty}\int_{-\infty}^{+\infty} (-v_1 v_2) f(v_1, -v_2; [0,0,H_3], t) dv_1 dv_2 \\ &= -E[u([0,0,H_3],t)v([0,0,H_3],t)] - E[\tilde{u}([0,0,H_3],t)\tilde{v}([0,0,H_3],t)] \end{aligned}$$

Hence, the desired property is obtained.

APPENDIX D

PROOF OF THE INDEPENDENCE BETWEEN $\dot{Z}_I(T)$ AND $Z(T)$

It is proven that $\dot{Z}_i(t)$ is independent of $Z(t)$ under some conditions. Without loss of generality, set $i = 1$.

The proof has two steps. First, let $\varphi(\nu_1, \nu_2, \nu_3)$ $= E(\exp\{[\sum_{j=1}^{3} \nu_j Z_j(t) + \nu Y_n(t)]i\})$ be the characteristic function of vector $[Z_1(t), Z_2(t), Z_3(t), Y_n(t)]$, where $Y_n(t) = [Z_1(t + h_n) - Z_1(t)]/h_n$. It is shown that $\lim_{h_n \to 0} \varphi(\nu_1, \nu_2, \nu_3, \nu) = E(\exp\{[\sum_{j=1}^{3} \nu_j Z_j(t) + \nu \dot{Z}_1(t)]i\})$, which is the characteristic function of vector $[Z_1(t), Z_2(t), Z_3(t), \dot{Z}_1(t)]$. Under the assumption that $Z_1(t)$ is mean square differentiable, $Y_n(t) \to \dot{Z}_1(t)$ in L_2 so that $Y_n(t) \xrightarrow{p} \dot{Z}_1(t)$ by Chebyshev's inequality [23](p.143). Set $\dot{Y}_n(t) = \sum_{j=1}^{3} \nu_j Z_j + \nu Y_n(t)$ and $\dot{Z}(t) = \sum_{j=1}^{3} \nu_j Z_j(t) + \nu \dot{Z}_1(t)$, giving $\tilde{Y}_n(t) \xrightarrow{p} \tilde{Z}_1(t)$, then each subsequence $\tilde{Y}_{n_k}(t)$ of $\tilde{Y}_n(t)$ contain a subsequence $\tilde{Y}_{n_{k_q}}(t)$ such that $\tilde{Y}_{n_{k_q}}(t) \xrightarrow{a.s.} Z(t)$ [23](p.72). Hence, the desired results are obtained by the continuity of characteristic function and bounded convergence theorem.

Second, the expression for $\lim_{h_n \to 0} \varphi(\nu_1, \nu_2, \nu_3, \nu)$ is derived. The value of $\lim_{h_n \to 0} \varphi(\nu_1, \nu_2, \nu_3, \nu)$ can be expressed by

$$\begin{aligned} &\lim_{h_n \to 0} \phi(\nu_1, \nu_2, \nu_3, \nu) \\ =&E\left(\exp\left\{\left[\left(\nu_1 - \frac{\nu}{h_n}\right) Z_1(t) + \frac{\nu}{h_n} Z_1(t + h_n) + \nu_2 Z_2(t) + \nu_3 Z_3(t)\right] i\right\}\right), \end{aligned} \quad \text{(D.1)}$$

Because $Z_1(t), Z_2(t)$, and $Z_3(t)$ are standard Gaussian processes, Eq. D.1

yields

$$\lim_{h_n \to 0} \phi(\nu_1, \nu_2, \nu_3, \nu)$$
$$= \lim_{h_n \to 0} \exp\left(-\frac{1}{2}\left\{ [2 - 2\rho_{11}(h_n)] \frac{\nu^2}{h_n^2} + [2\rho_{11}(h_n) - 2]\frac{\nu\nu_1}{h_n} + [2\rho_{12}(h_n) - 2\rho_{12}(0)]\frac{\nu\nu_2}{h_n} \right.\right.$$
$$\left.\left. + [2\rho_{13}(h_n) - 2\rho_{13}(0)]\frac{\nu\nu_3}{h_n} + \nu^T \Sigma \nu \right\}\right), \tag{D.2}$$

where $\rho_{pq}(h_n) = E[Z_p(t + h_n)Z_q(t)]$, $p, q = 1, 2, 3$; $\nu = [\nu_1, \nu_2, \nu_3]^T$; and $\Sigma = 3 \times 3$ matrix whose first, second, and third columns are $[1, \rho_{12}(0), \rho_{13}(0)]^T$, $[\rho_{12}(0), 1, \rho_{23}(0)]^T$, and $[\rho_{13}(0), \rho_{23}(0), 1]^T$, respectively. Because $Z_1(t)$ is stationary and mean square differentiable, $-\partial^2\rho_{11}(h_n)/\partial h_n^2|_{h_n=0}$ exists and $\partial\rho_{11}(h_n)/\partial h_n|_{h_n=0} = 0$. Under the hypotheses that $\rho_{12}(h_n) = \rho_{12}(-h_n)$ and $\rho_{13}(h_n) = \rho_{13}(-h_n)$, $\partial\rho_{12}(h_n)/\partial h_n|_{h_n=0} = 0$ and $\partial\rho_{13}(h_n)/\partial h_n|_{h_n=0} = 0$. Therefore

$$\lim_{h_n \to \infty} \phi(\nu_1, \nu_2, \nu_3, \nu) = \exp\left\{ -\frac{\nu^2}{2}\left[-\frac{\partial^2\rho_{11}(h_n)}{\partial h_n^2} \right] |_{h_n=0} \right\} \exp\left(-\frac{1}{2}\nu^T \Sigma \nu \right), \tag{D.3}$$

in which the first term on the right-hand side is the characteristic function of $\dot{Z}_1(t)$ and the second one is the characteristic function of $Z(t)$. Hence, $\dot{Z}(t)$ is independent of $Z(t)$.

Bibliography

[1] H. Ahn, E. Choi, and I. Han. "Extracting underlying meaningful fratures and canceling noise using independent component analysis for direct marketing". In: *Expert Systems with Applications* 33.1 (2007), pp. 181–191.

[2] J. B. Barlow, W. H. Rae, and A. Pope. *Low-speed wind tunnel testing*. New York, NY: Wiley, 1999.

[3] P. Bochini and G. Deodatis. "Critical review and latest developments of a class of simulation algorithms for strongly non-Gaussian random fields". In: *Probabilistic Engineering Mechanics* 23 (2008), pp. 393–407.

[4] X. R. Cao and R. W. Liu. "General Approach to Blind Source Separation". In: *Signal Processing* 44.3 (1996), pp. 562–571.

[5] L. Carassale. "Analysis of Aerodynamic Pressure Measurements by Dynamic Coherent Structures". In: *Probabilistic Engineering Mechanics* 28 (2012), pp. 66–74.

[6] X. Chen and Y. Fan. "Estimation of copula-based semiparametric time series models". In: *Journal of Econometrics* 130 (2006), pp. 307–335.

[7] M. Ciampoli, F. Petrini, and G. Augusti. "Performance-based wind engineering: towards a general procedure". In: *Structural Safety* 33.6 (2011), pp. 367–378.

[8] P. Comon. "Independent Component Analysis, A New Concept?" In: *Signal Processing* 36.3 (1994), pp. 287–314.

[9] P. Comon. "Separation of Stochastic Processes". In: *Workshop on Higher-Order Spectral Analysis* (1989), pp. 174 –179.

[10] W. Darsow, B. Nguyen, and E. Olsen. "Copulas and Markov processes". In: *Illinois Journal of Mathematics* 36 (1992), pp. 600–642.

[11] G. Deodatis and R. Micaletti. "Simulation of highly skewed non-Gaussian stochastic processes". In: *Journal of Engineering Mechanics* 127 (2001), pp. 1284–1295.

[12] T. S. Ferguson. "A Representation of the Symmetric Bivariate Cauchy Distribution". In: *The Annals of Mathematical Statistics* 33.4 (1962), pp. 1256–1266.

[13] R. Field and M. Grigoriu. "Convergence properties of polynomial chaos approximations for $\mathcal{L}_2$ random variables". In: *Sandia Report* 2007-1262 (2007).

[14] R. Field and M. Grigoriu. "On the accuracy of the polynomial chaos approximation". In: *Probabilistic Engineering Mechanics* 19 (2004), pp. 65–80.

[15] A. Ghobarah. "Performance-based design in earthquake engineering: state of development". In: *Engineering Structures* 23.8 (2001), pp. 878–884.

[16] M. Gioffre, V. Gusella, and M. Grigoriu. "Simulation of non-Gaussian field applied to wind pressure fluctuations". In: *Probabilistic Engineering Mechanics* 15 (2000), pp. 339–345.

[17] M. Grigoriu. *Applied Non-Gaussian Processes: Examples, Theory, Simulation, Linear Random Vibration, and MATLAB Solutions*. Englewood Cliffs, NJ, USA: PTR Prentice Hall, 1995.

[18] M. Grigoriu. *Applied non-Gaussian processes: Examples, theory, simulation, linear random vibration, and MATLAB solutions*. Englewood Cliffs, NJ: PTR Prentice Hall, 1995.

[19] M. Grigoriu. “Existence and construction of translation models for stationary non-Gaussian processes”. In: *Probabilistic Engineering Mechanics* 24 (2009), pp. 545–551.

[20] M. Grigoriu. “On the spectral representation method in simulation”. In: *Probabilistic Engineering Mechanics* 8 (1993), pp. 75–90.

[21] M. Grigoriu. *Random vibration of mechanical and structural systems*. Englewoods Cliffs, NJ: Prentice Hall, 1993.

[22] M. Grigoriu. “Simulation of stationary non-Gaussian translation processes”. In: *Journal of Engineering Mechanics* 124.2 (1998), pp. 121–126.

[23] M. Grigoriu. *Stochastic calculus: Applications in science and engineering*. Boston: Birkhäuser, 2002.

[24] M. Grigoriu. *Stochastic Calculus: Applications in Science and Engineering*. Boston, MA: Birkhaüser, 2002.

[25] M. Grigoriu and S. T. Ariaratnam. “Response of linear systems to polynomials of Gaussian processes”. In: *Journal of Applied Mechanics* 55.4 (1988), pp. 905–910.

[26] M. Grigoriu and R. V. Field. “A method for analysis of linear dynamic systems driven by stationary non-Gaussian noise with applications to turbulence-induced random vibration”. In: *Applied Mathematical Modelling* 38.1 (2014), pp. 336–354.

[27] S. Grimaldi and F. Serinaldi. “Asymmetric copula in multivariate flood frequency analysis”. In: *Advances in Water Resources* 29.8 (2006), pp. 1155–1167.

[28] K. R. Gurley, M. A. Tognarelli, and A. Kareem. “Analysis and simulation tools for wind engineering”. In: *Probabilistic Engineering Mechanics* 12.1 (1997), pp. 9–31.

[29] J. D. Holmes. *Wind loading of structures*. New York, NY: CRC Press, 2007.

[30] A. Hyvärinen and E. Oja. “Independent Component Analysis: Algorithms and Applications”. In: *Neural Networks* 13.4-5 (2000), pp. 411–430.

[31] R. Ibragimov. “Copula-based characterizations for higher order Markov processes”. In: *Econometric Theory* 25 (2009), pp. 819–846.

[32] J. Jiang. *Large sample techniques for statistics*. New York: Springer, 2010.

[33] H. Joe. *Multivariate Models and Dependence Concepts*. Chapman and Hall, 1997.

[34] H. Joe. *Multivariate models and dependence concepts*. London, UK: Chapman & Hall, 1997.

[35] A. Kareem and T. Wu. “Wind-induced effects on bluff bodies in turbulent flows: nonstationary, non-Gaussian and nonlinear features”. In: *Journal of Wind Engineering and Industrial Aerodynamics* 122 (2013), pp. 21–37.

[36] H. Kawai. “Pressure fluctuations on square prisms - applicability of strip and quasi-steady theories”. In: *Journal of Wind Engineering and Industrial Aerodynamics* 13 (1983), pp. 197–208.

[37] H. Kikuchi et al. “Dynamic wind pressures acting on a tall building model-Proper orthogonal decomposition”. In: *Jounal of Wind Engineering and Industrial Aerodynamics* 69-71 (1997), pp. 631–646.

[38] S. Kotz, N. Balakrishnan, and N. L. Johnson. *Continuous Multivariate Distributions*. Volume 1: Models and Applications. New York: John Wiley & Sons, Inc, 2000.

[39] L. Li, K. Phoon, and S. Quek. “Comparison between Karhunen-Loéve expansion and translation-based simulation of non-Gaussian processes”. In: *Computers and Structures* 85 (2007), pp. 264–276.

[40] W. V. Li and Q. M. Shao. “A Normal Comparison Inequality and Its Applications”. In: *Probability Theory and Related Fields* 122.4 (2002), pp. 494–508.

[41] W. V. Li and Q. M. Shao. “A normal comparison inequality and its applications”. In: *Probability Theory and Related Fields* 122.4 (2002), pp. 494–508.

[42] E. Liebscher. “Construction of asymmetric multivariate copulas”. In: *Journal of Multivariate Analysis* 99.10 (2008), pp. 2234–2250.

[43] E. Moreau. “A Generalization of Joint-diagonalization Criteria for Source Separation”. In: *Signal Processing* 49.3 (2001), pp. 530–541.

[44] A. Naess and O. Gaidai. “Monte carlo methods for estimating the extreme response of dynamical systems”. In: *Jounal of Engineering Mechanics* 134.8 (2008), pp. 628–636.

[45] R. Nelson. *An introduction to copulas*. 2nd. Springer Series in Statistics. New York, NY: Springer, 2007.

[46] K. Phoon, H. Huang, and S. Quek. “Simulation of strongly non-Gaussian processes using Karhunen-Loéve expansion”. In: *Probabilistic Engineering Mechanics* 20.2 (2005), pp. 188–198.

[47] S. I. Resnick. *A probability path*. Boston: Birkhäuser, 1998.

[48] R. Rubinstein. *Simulation and the Monte Carlo Method*. New York, NY: John Wiley & Sons, 1981.

[49] S. Sakamoto and R. Ghanem. “Simulation of multi-dimensional non-Gaussian, non-stationary random fields”. In: *Probabilistic Engineering Mechanics* 17 (2002), pp. 167–176.

[50] M. D. Shields, G. Deodatis, and P. Bocchini. “A simple and efficient methodology to approximate a general non-Gaussian stationary stochastic process by a translation process”. In: *Probabilistic Engineering Mechanics* 26 (2011), pp. 511–519.

[51] M. D. Shields and H. Kim. “Simulation of higher-order stochastic processes by spectral representation”. In: *Probabilistic Engineering Mechanics* 47 (2017), pp. 1–15.

[52] G. Solari. “Gust-excited vibrations”. In: *Wind-excited vibrations of structures* (1994), pp. 195–291.

[53] G. Solari and G. Piccardo. “Probabilistic 3-D turbulence modeling for gust buffeting of structures”. In: *Probabilistic Engineering Mechanics* 16.1 (2001), pp. 73–86.

[54] G. Solari and F. Tubino. “Dynamic approach to the wind loading of structures: Alongwind, crosswind, and torsional responses”. In: *Wind effects on buildings and design of wind-sensitive structures* (2007), pp. 137–166.

[55] B. J. Vickery and A. W. Clark. “Lift or across-wind response to tapered stacks”. In: *Journal of the Structural Division* 98.1 (1972), pp. 1–20.

[56] F. Yamazaki and M. Shinozuka. “Digital generation of non-Gaussian stochastic fields”. In: *Journal of Engineering Mechanics* 114 (1988), pp. 1183–1197.

[57] A. Yeredor. “Blind Source Separation via The Second Characteristic Function”. In: *Signal Processing* 80.5 (2000), pp. 897–902.

[58] H. Zhao and M. Grigoriu. “A new perspective on independent component analysis”. In: *Probabilistic Engineering Mechanics* 42 (2015), pp. 64–70.